EXPERIMENTAL INVESTIGATION OF NEAR AND FAR FIELD FLOW CHARACTERISTICS OF CIRCULAR AND NON-CIRCULAR TURBULENT JETS

A THESIS SUBMITTED TO
THE GRADUATE SCHOOL OF NATURAL AND APPLIED SCIENCES
OF
MIDDLE EAST TECHNICAL UNIVERSITY

BY

GÜRSU TAŞAR

IN PARTIAL FULFILLMENT OF THE REQUIREMENTS
FOR
THE DEGREE OF MASTER OF SCIENCE
IN
AEROSPACE ENGINEERING

DECEMBER 2008

Approval of the thesis:

EXPERIMENTAL INVESTIGATION OF NEAR AND FAR FIELD FLOW CHARACTERISTICS OF CIRCULAR AND NON-CIRCULAR TURBULENT JETS

submitted by **GÜRSU TAŞAR** in partial fulfillment of the requirements for the degree of **Master of Science in Aerospace Engineering Department, Middle East Technical University** by,

Prof. Dr. Canan Özgen
Dean, Graduate School of **Natural and Applied Sciences** ________________

Prof. Dr. İsmail H. Tuncer
Head of Department, **Aerospace Engineering** ________________

Assoc. Prof. Dr. Serkan Özgen
Supervisor, **Aerospace Engineering Dept., METU** ________________

Assist. Prof. Dr. Oğuz Uzol
Co-supervisor, **Aerospace Engineering Dept., METU** ________________

Examining Committee Members:

Prof. Dr. Cevdet Çelenligil
Aerospace Engineering Dept., METU ________________

Assoc. Prof. Dr. Serkan Özgen
Aerospace Engineering Dept., METU ________________

Prof. Dr. İsmail Hakkı Tuncer
Aerospace Engineering Dept., METU ________________

Assoc. Prof. Dr. Yusuf Uludağ
Chemical Engineering Dept., METU ________________

Assist. Prof. Dr. Oğuz Uzol
Aerospace Engineering Dept., METU ________________

Date: ________________

I hereby declare that all information in this document has been obtained and presented in accordance with academic rules and ethical conduct. I also declare that, as required by these rules and conduct, I have fully cited and referenced all material and results that are not original to this work.

Name, Last Name: GÜRSU TAŞAR

Signature :

ABSTRACT

EXPERIMENTAL INVESTIGATION OF NEAR AND FAR FIELD FLOW CHARACTERISTICS OF CIRCULAR AND NON-CIRCULAR TURBULENT JETS

Taşar, Gürsu

M.S., Department of Aerospace Engineering

Supervisor : Assoc. Prof. Dr. Serkan Özgen

Co-Supervisor : Assist. Prof. Dr. Oğuz Uzol

December 2008, 82 pages

The atomization problem of high speed viscous jets has many applications in industrial processes and machines. In all these applications, it is required that the droplets have high surface area/volume ratio meaning that the droplets should be as small as possible. This can be achieved with high rates of turbulence and mixing of the flow. In order to constitute a foresight of geometry effects on droplet size, experimental investigation and the determination of flow characteristics in near and far fields of a low-speed air jet have been performed. In order to fulfill this task, three components of instantaneous velocity are measured, using a triple sensor Constant Temperature Anemometer (CTA) system. Through these measurements, mean velocity, Reynolds stress, velocity decay, spreading rate, turbulent kinetic energy, vorticity, and mass entrainment rate values are obtained. Stress-Strain relationship is also observed. Measurements are obtained for a baseline circular nozzle (round jet) as well as for an equilateral triangular and a square nozzle. On the basis of these measurements, the equilateral triangular jet is found to be the best option in order to get highest turbulence and mixing level with smallest core length.

Keywords: Experimental aerodynamics, turbulence, viscous jet, vorticity, mixing, Reynolds stress, non circular jet

ÖZ

DAİRESEL VE DAİRESEL OLMAYAN TÜRBÜLANS JETLERİN YAKIN VE UZAK BÖLGELERİNDEKİ AKIŞ YAPISININ DENEYSEL YÖNTEMLER KULLANARAK İNCELENMESİ

Taşar, Gürsu

Yüksek Lisans, Havacılık ve Uzay Mühendisliği Bölümü

Tez Yöneticisi : Doç. Dr. Serkan Özgen

Ortak Tez Yöneticisi : Yrd. Doç. Dr. Oğuz Uzol

Aralık 2008, 82 sayfa

Yüksek hızlı viskoz jetlerin atomizasyon problemi bir çok endüstriyel süreç ve makinede uygulama alanı bulmaktadır. Tüm bu uygulamalarda, damlacıkların yüksek yüzey alanı/hacim oranına sahip olmaları tercih edilmektedir. Bu da damlacıkların mümkün olduğunca küçük olmaları gerektiği anlamına gelmektedir. Damlacık boyutundaki küçülme akışın türbülanslı olması ve karışım oranlarıyla artmaktadır. Değişik geometrilerin parçacık boyutuna etkisini anlayabilmek için düşük hızlı hava jetinin deneysel olarak incelenmesi, yakın ve uzak akış bölgelerinde akış ve türbülans karakteristiklerinin hesaplanması ve yakın akış bölgesinde gerinim ve gerilim ilişkilerinin belirlenmesi bu tezin konusunu oluşturmaktadır. Değişik geometrilerdeki akışın karışım oranları da hesaplanmıştır. Ölçümler daire, eşkenar üçgen ve kare şeklinde kesit alanlara sahip lülelerde yapılmıştır. Elde edilen sunuçlara göre eşkenar üçgen en yüksek türbülans ve karışım oranlarını verirken, en düşük göbek uzunluğuna sahiptir.

Anahtar Kelimeler: Deneysel aerodinamik, türbülans, viskoz jet, vortisite, karışma, Reynolds gerilimi, dairesel olmayan jet

To my family

ACKNOWLEDGMENTS

I would like to express my sincere gratitude to my supervisor Assoc. Prof. Dr. Serkan Özgen and co-supervisor Assist. Prof. Dr. Oğuz Uzol who supervised all steps of this work and provided the necessary resources of their knowledge and experience. Their enthusiasm, support and guidance helped me to complete this work, and constitute a solid example for being good researcher.

I wish to state may endless thanks to Nuri Erkin Öçer. I probably would not be able to finish my thesis without his help about designing and conducting the experiments. Designing the experiments would also be impossible without help and experience of Ahmet Uyar and Murat Ceylan.

I appreciate Deniz Yılmaz and Özlem Ceyhan who helped me a lot especially throughout the writing progress of this thesis. I would like to thank to Onur Tarımcı, Volkan Kargın and Mustafa Kaya sharing their software knowledge with me. I would also like to thank to all my friends within the Aerospace Engineering Department; Gökhan Ahmet, Sinan Körpe, Tahir Turgut, Alper Ezertaş, Mehmet Karaca, Eser Kubalı, Tuba Elmas, Sinem Işık and Zeynep Çakır for their supports and always being on my side during the thesis. Special thanks to all Aerospace Engineering Department staff for their kind responses.

Finally, I would like to express my deepest thanks to my parents and sister for their endless support throughout my life and Türkan Kobak supporting me in all aspect of my life. Without their love, patience and limitless support, what I achieved so far would be far from success.

The support given through the grant 106M067 by The Scientific and Technological Research Council of Turkey (TUBITAK) to this thesis is greatly acknowledged.

TABLE OF CONTENTS

LIST OF TABLES

TABLES

LIST OF FIGURES

FIGURES

LIST OF ABBREVIATIONS

x	Axial coordinate
y	Vertical coordinate
z	Horizontal coordinate
e_1, e_2, e_3	Hot wire voltages
$U_{cal1}, U_{cal2}, U_{cal3}$	Calibration velocities
U_1, U_2, U_3	Velocities in the wire-coordinate system
U	Axial velocity
V	Vertical velocity
W	Horizontal velocity
$\overline{U}$	Mean axial velocity
$\overline{V}$	Mean vertical velocity
$\overline{W}$	Mean horizontal velocity
u	Fluctuating axial velocity
v	Fluctuating vertical velocity
w	Fluctuating horizontal velocity
P	Pressure
$\overline{P}$	Mean pressure
p	Fluctuating pressure
$\overline{U_i}$	Tensorial notation of mean velocity
u_i	Tensorial notation of fluctuating velocity
t	Time
$\frac{\partial}{\partial t}$	Partial time derivative
$\frac{\partial}{\partial x_j}$	Partial spatial derivative
ν	Kinematic viscosity
μ	Dynamic viscosity
ρ_0	Density of the jet fluid
δ_{ij}	Kronecker's delta
$\overline{u_i u_j}$	Reynolds stress tensor
a_{ij}	Anisotropy tensor
$\overline{S_{ij}}$	Mean strain rate tensor
k	Turbulent kinetic energy
E	Kinetic energy of the flow
$\overline{E}$	Kinetic energy of the mean flow
$\overline{uu}$	Streamwise component of Reynolds normal stress
$\overline{vv}$	Vertical component of Reynolds normal stress
$\overline{ww}$	Horizontal component of Reynolds normal stress
$\overline{uv}$	Vertical component of Reynolds primary shear stress
$\overline{uw}$	Horizontal component of Reynolds primary shear stress
$\overline{vw}$	Reynolds secondary shear stress
ω_x	Axial vorticity
N	Number of samples
d	Equivalent exit diameter
r	Radial direction
$r_{1/2}$	Half velocity width
U_0	Local maximum of the axial velocity
U_e	Jet exit velocity
Re	Reynolds number
B	Velocity decay rate
S_r	Spreading rate
Q	Mass flow rate at a streamwise location
Q_0	Mass flow rate at the jet exit
$f_{cut-off}$	Cut-off frequency
f_{max}	Max frequency
t_{record}	Sampling time

CHAPTER 1

INTRODUCTION

Mixing helps to convert heterogeneous physical systems into more homogeneous ones. For example in processes such as combustion, in which chemical reactions between the fuel and the oxidizer are accompanied by the production of heat, mixing becomes a complex problem that is usually difficult to define and analyze. The mixing of air and fuel ejecting from nozzles needs special attention. Improved combustion performance may be obtained by using non-circular nozzle geometry as a passive mixing control technique, which is also easy to apply in industrial systems. The ejection of accelerated air through a nozzle into stagnant ambient air constitutes a general configuration for the numerical and experimental mixing studies. The vorticity distribution which dominates the evolution of turbulent structures of the flow is an important deterministic parameter that can be used to measure the mixing levels of flows. The entrainment of the ambient flow is generally driven by large and small scale turbulent structures within the jet flow field [1].

Various studies have investigated circular and non-circular sharp-edged orifices and jets. The experimental study of Wygnanski and Fielder [2] is a premise for following studies in terms of mean velocity profiles, Reynolds stresses and triple correlation. Baker [3] and Seif [4] discovered that data supplied by Wygnanski and Fielder for far field fail to satisfy the constraint of the integrated axial momentum equation. Another experimental study performed by Hussein et al [5] provides reliable data set and results also for far field of the jet flow. The reliability of the study of Hussein et al is based on various data acquisition techniques that are used in the experiments such as flying and stationary hot wire anemometry and burst mode laser Doppler anemometry.

In the numerical study of Miller et al [6], three-dimensional jets emanating from non-circular nozzles were observed and compared with circular ones at low Reynolds numbers using Direct Numerical Simulation (DNS). The axis rotation phenomenon, an indicator of better mixing characteristics, was observed for all non-circular jets. The work by Gutmark and Grinstein [7] has also indicated the significance of axis rotation of non-circular jets, which make them more efficient mixers than the circular jets. The jet core length was also stressed as a result of mixing [7], and the results showed that the isosceles triangular jet is the most efficient mixer over other jets investigated. On the experimental side, Quinn has investigated the near-field of a flow emanating from a sharp-edged equilateral triangular orifice [8] as well as from a sharp-edged isosceles one [9] by taking velocity measurements with a hot-wire anemometer. As a result, some quantitative outcomes on the mixing rate were obtained and the isosceles triangular jet was found to be a better mixer compared to the circular and equilateral triangle. One point that is not fully investigated in previous studies is the effect of corner radii in non-circular jets and this point is indicated to be a further research topic by Quinn [8]. The existence of sharp corners in the nozzle can increase the fine-scale turbulence at the corners relative to the flat segments of the nozzle as indicated in Schadow et al [10], and Toyoda et al and enhance mass entrainment significantly [11].

In the study of Hussein et al [5] the self preserving behaviour (self similarity) of the round jet is examined and compared with Wygnanski [2] as well as the velocity decay rate and spread rate. Gaskin [12], Bradbury [13], Chu[14] and Maczynski [15] also study the self preserving behaviour for co-flowing round jets.

The stress-strain relation based on the velocity gradient of the turbulent shear flows are observed in the studies of Tao et al [16], and Kang and Meneveau [17]. The relation between mean strain rates and anisotropic stress is investigated at the principal axes.

In this study, turbulence structures and mixing levels of the jets emanating from circular and non-circular nozzles with round corners are investigated experimentally using hotwire anemometry. The experiments are performed in a low-speed free-jet facility at near and far fields with a maximum mean streamwise velocity of 22 m/s. The near field data is obtained at streamwise stations of x/d = 0, 1, 2, 4, 6 and 10, by scanning cross stream (lateral) planes, and horizontal (longitudinal) center-plane, whereas the far field data acquisition stations are located at x/d = 15, 20, 25, 30, 35, 40, 45, and 50. Additional data are acquired on closely spaced planes at near field stations of x/d = 2 to obtain streamwise gradients that are necessary to investigate stress-strain relationship. The corresponding Reynolds number is 5.5×10^4 based on the mean streamwise velocity and the nozzle equivalent diameter ($d = 40mm$). The velocity decay (B), and spreading rate (S_r) are determined and compared. Normalized values of mean axial velocities, Reynolds stresses and turbulent kinetic energies at the far field region of jet flow with a traversing process are carried out only in a horizontal direction, along a single axis z. Comparison of the round jet results with the previous studies of Hussein et al [5] and Wygnanski and Fielder [2] at the far field is also made. Distributions of all three components of the mean velocity vector are obtained at the near field region of the flow field for a baseline circular nozzle (round jet) and for equilateral triangular and square nozzles in a square plane parallel to the nozzle exit plane. The data are used to determine and compare the six components of the Reynolds stress tensor, streamwise vorticity, turbulent kinetic energy and mass entrainment rates for all three types of jets. The stress-strain behaviour of the jets at $x/d = 2$ are also observed for the principal axes.

CHAPTER 2

EXPERIMENTAL PROCEDURE

2.1 Experimental Setup

In this study the experiments are conducted in a free jet facility shown in Figure 2.1. It consists of an axial fan, a duct, a contraction, a settling chamber and a diffuser that enables attaching of different nozzles at its exit. Honeycombs are used at the entrance of the settling chamber to obtain a homogeneous flow across the facility and pads are used at necessary points to prevent vibration. The diffuser, settling chamber and contraction are constructed from Plexiglas whereas the fan transition duct and nozzles are made of metal. The diffuser has an inlet area of $0.5 \times 0.66m^2$ and an exit area of $0.66 \times 0.66m^2$ and $0.34m$ length. The settling chamber has a square cube having a length of $0.565m$. The contraction has a length of $0.29m$ and has inlet and exit areas of $0.66 \times 0.66m^2$ and $0.237 \times 0.237m^2$, respectively, resulting a contraction ratio of 7.75. The three nozzles have cross sectional shapes of circle, square and equilateral triangle. All nozzles have a contraction part with a length of 0.5m and a straight part again with a length of 0.5m. The straight pipe section of nozzles have equivalent exit diameter of $d = 40mm$. Calculation of d is based on equally designed cross sectional areas of nozzles.

By using a computer controlled traversing mechanism that allows a $0.00254m$ resolution in x, y, z direction, the three components of velocity were measured on cross sectional planes at six and eight streamwise stations in near and far fields respectively. The region between the jet exit and $x/d < 10$ is defined as the near field region of the jet flow whereas far field region comprises of $x/d > 15$. Coordinate system is depicted in Figure 2.1.

The near field data acquisition is organized in order to obtain velocity fields in each stream-

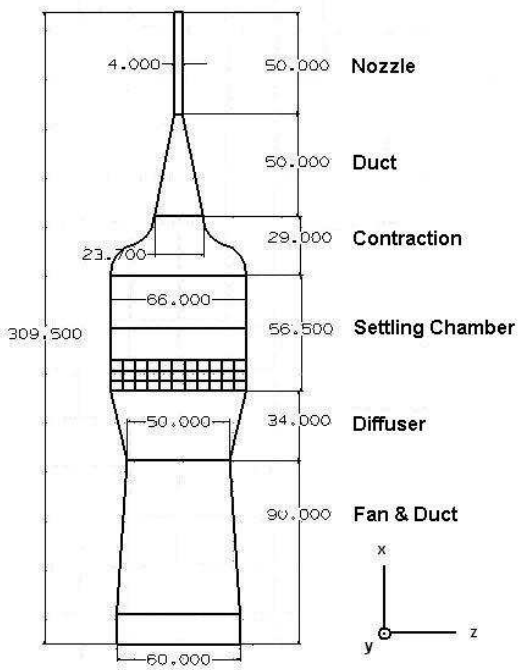

(a) Top view drawing of jet facility

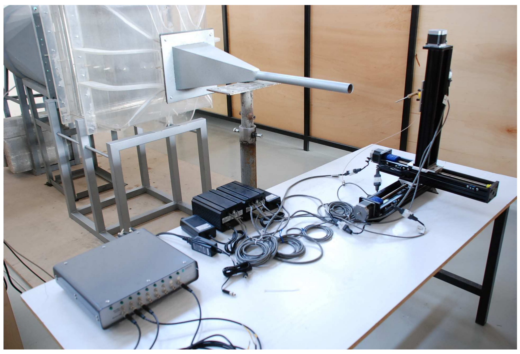

(b) Jet facility, data acquisition and traversing system

Figure 2.1: Experimental facility (dimensions are in cm).

wise station which are located at $x/d = 0, 1, 2, 4, 6$ and 10. The probe is traversed through a total length of 152.4mm with a grid spacing of 3.81mm in y and z directions for all streamwise stations at near field. At station $x/d = 2$, two additional velocity fields are obtained which are located 3.81mm downstream and 3.81mm upstream of the nominal location in order to determine the streamwise velocity gradient at the specified location. The horizontal center-plane measurements are designed to comprise all near field region in x-z plane. The probe is traversed through a total length of 394.34mm and total width of 148.59mm with a grid spacing of 5.715mm in x and z directions respectively, for all nozzle types.

On the other hand the farfield data acquisition is organized to obtain the half of the centerline velocity profile. The farfield streamwise stations are located at x/d = 15, 20, 25, 30, 35, 40, 45, and 50. Traversing process is carried out only in the horizontal direction (z axis), and through a total length of 681.99 mm with a grid spacing of again 3.81mm.

The measurement unit used in the experiments was a DANTEC P91 triaxial hotwire anemometer designed for high-turbulence flows. It has gold-plated probes having 5µm diameter and

3mm overall length which provides the necessary information for calculation of the full Reynolds stress tensor. The data are acquired using NI 9205 analog input module with 250 kS/s aggregate sampling rate.

A Labview code is used to coordinate traverse mechanism and the Constant Temperature Anemometry (CTA). The values of sampling rate, samples to read, sampling time and grid resolution are also set by using that code.

2.2 Methodology

The experiments are performed at a maximum mean streamwise velocity of 22m/s and the data is obtained by traversing a triple-sensor hot-wire probe at varying streamwise locations downstream of the jet exit plane. The corresponding Reynolds number is 5.76×10^4 based on the mean streamwise velocity and the nozzle equivalent diameter ($d = 40mm$).

Before beginning the data acquisition process the sampling rates of 1 kHz, 5 kHz, 10 kHz, 15 kHz, and 20 kHz are checked in order to decide most suitable one. Considering also the study of Quinn [8] in which sampling rate is set to 4 kHz, the sampling rate is decided to be 5 kHz which is the optimum value among variety of tested sampling rates. Together with 2 seconds of sampling time in the near field region, 10000 samples at each grid point maintain good observation of turbulence. On the other hand 50000 samples are acquired at each grid point in the far field region with same sampling rate.

2.2.1 Calibration and Data Conversion

The manufacturer's given constants were used for directional calibration, and velocity calibration was conducted at the center point of the exit of the wind tunnel. Three conversions are made in order to derive the actual velocities. In the first step, hot wire voltages e_1, e_2, and e_3 are converted to calibration velocities namely U_{cal1}, U_{cal2}, U_{cal3}. In the second step the calibration velocities are converted to the U_1, U_2, U_3 velocities which are defined for the for the wire coordinate system. The final conversion is performed to obtain U, V, W which are the main x, y and z components of velocity respectively. Several calibrations are performed at 20, 22, 25, and 28 °C, due to temperature changes. The e to U_{cal} curve fit obtained for 20

°C is shown in Figure 2.2.

MMF model is used to convert the CTA output voltage e_1, e_2, and e_3 into velocity values U_{cal1}, U_{cal2}, U_{cal3} specified in Figure 2.2 and the curves are found to be

$$U_{cal1} = \frac{(-0.4439668 * 400.47362 + 107.14277 * e_1^7.9047463)}{(400.47362 + e_1^7.9047463)}, \tag{2.1a}$$

$$U_{cal2} = \frac{(-0.53443656 * 232.62451 + 155.85194 * e_2^7.2805617)}{(232.62451 + e_2^7.2805617)}, \tag{2.1b}$$

$$U_{cal3} = \frac{(-0.49409868 * 903.65463 + 164.77246 * e_3^7.4223736)}{(903.65463 + e_3^7.4223736)}. \tag{2.1c}$$

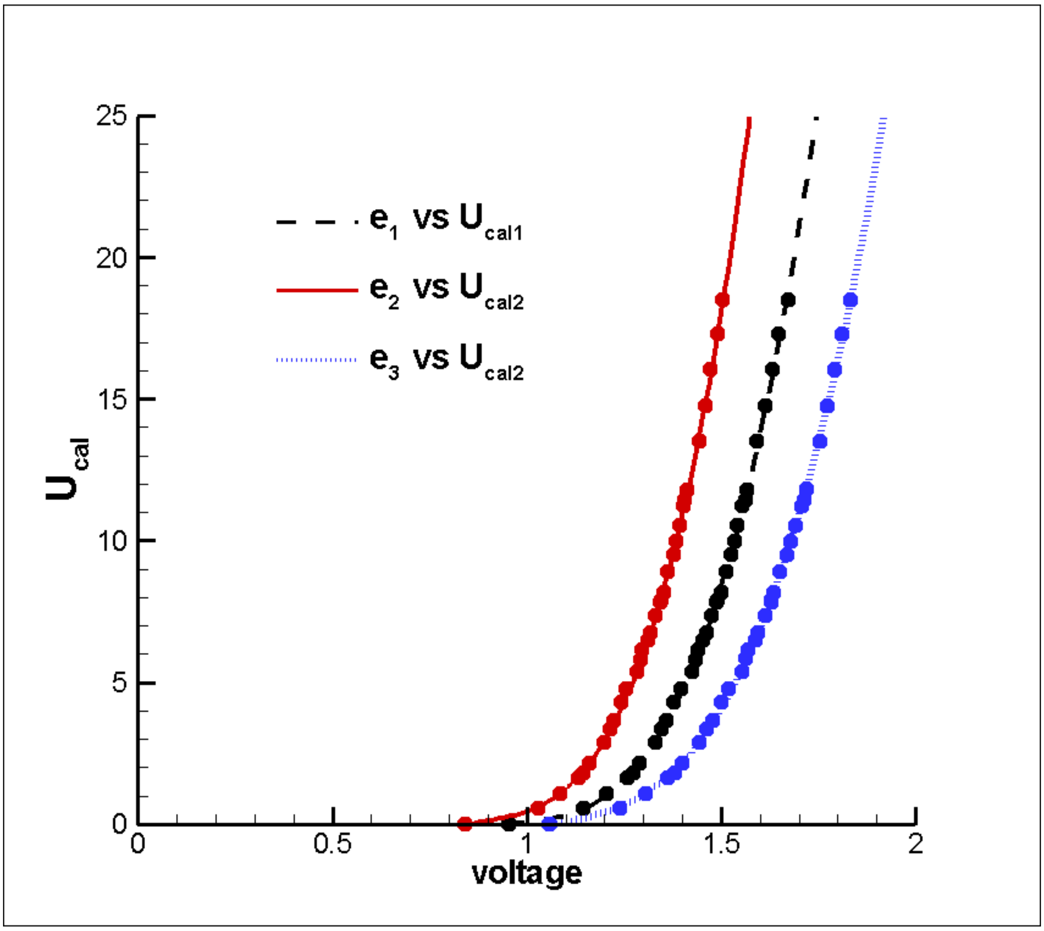

Figure 2.2: e vs. U_{cal} for 20 °C.

The remaining conversions are made by using the equations shown below:

$$U_1 = \sqrt{-0.3676U_{cal1}^2 + 0.3747U_{cal2}^2 + 0.3453U_{cal3}}, \tag{2.2a}$$

$$U_2 = \sqrt{0.3453U_{cal1}^2 - 0.3676U_{cal2}^2 + 0.3747U_{cal3}}, \tag{2.2b}$$

$$U_3 = \sqrt{0.3747U_{cal1}^2 + 0.3453U_{cal2}^2 - 0.3676U_{cal3}}, \tag{2.2c}$$

and

$$U = U_1 \cos 54.74 + U_2 \cos 54.74 + U_3 \cos 54.74, \tag{2.3a}$$

$$V = -U_1 \cos 45 - U_2 \cos 135 + U_3 \cos 90, \tag{2.3b}$$

$$W = -U_1 \cos 114.09 - U_2 \cos 114.09 - U_3 \cos 35.26, \tag{2.3c}$$

which in fact, include the directional calibration and supplied by the manufacturer.

2.2.2 Data Reduction

The collected data is used to obtain the basic turbulence characteristics of jet flow. Those characteristics are derived by substituting Reynolds decomposition of the velocity field and pressure into continuity and momentum equations based on the incompressible flow and constant viscosity assumption. Body forces are neglected. Emerging equations represent the effects of turbulent fluctuations on the mean flow [18].

2.2.2.1 Equations of Motion

In the very beginning of derivation it is wise to introduce the Reynolds decomposition

$$U(x, y, z, t) = \overline{U}(x, y, z, t) + u(x, y, z, t), \tag{2.4a}$$

$$P(x, y, z, t) = \overline{P}(x, y, z, t) + p(x, y, z, t), \tag{2.4b}$$

continuity equation

$$\frac{\partial U_i}{\partial x_i} = 0, \tag{2.5}$$

the momentum equation

$$\frac{\partial U_i}{\partial t} + U_j \frac{\partial U_i}{\partial j} = -\frac{1}{\rho_0}\frac{\partial P}{\partial x_i} + \nu \frac{\partial^2 U_i}{\partial x_j^2}, \tag{2.6}$$

and the axial vorticity,

$$\omega_x = \frac{\partial \overline{W}}{\partial y} - \frac{\partial \overline{V}}{\partial z}, \tag{2.7}$$

where quantities with a bar and lowercase letters in the Reynolds decomposition indicates the mean and fluctuating quantities, respectively.

Averaging the continuity equation yields

$$\overline{\frac{\partial(\overline{U}_i + u_i)}{\partial x_i}} = \overline{\frac{\partial \overline{U}_i}{\partial x_i}} + \overline{\frac{\partial u_i}{\partial x_i}}. \tag{2.8}$$

As the operation of differentiation commutes with the operation of ensemble averaging [18], the orders can be interchanged and the equation 2.8 becomes

$$\overline{\frac{\partial(\overline{U}_i + u_i)}{\partial x_i}} = \frac{\partial \overline{U}_i}{\partial x_i} + \frac{\partial \overline{u}_i}{\partial x_i}. \tag{2.9}$$

Using $\overline{u}_i = 0$ which shows the fluctuating velocities have zero mean;

$$\frac{\partial \overline{U}_i}{\partial x_i} = 0, \tag{2.10}$$

and

$$\frac{\partial u_i}{\partial x_i} = 0, \tag{2.11}$$

which results in the continuity equation for turbulent fluctuating field.

Applying the same procedure for the momentum equation gives

$$\frac{\partial(\overline{U}_i + u_i)}{\partial t} + (\overline{U}_j + u_j)\frac{\partial(\overline{U}_i + u_i)}{\partial x_j} = -\frac{1}{\rho_0}\frac{\partial(\overline{P} + p)}{\partial x_i} + \nu\frac{\partial^2(\overline{U}_i + u_i)}{\partial x_j^2}. \tag{2.12}$$

Averaging the time derivative, advective, pressure gradient and viscous terms yields

$$\overline{\frac{\partial(\overline{U}_i + u_i)}{\partial t}} = \frac{\partial\overline{U}_i}{\partial t} + \overline{\frac{\partial u_i}{\partial t}} = \frac{\partial\overline{U}_i}{\partial t} + \frac{\partial\overline{u}_i}{\partial t} = \frac{\partial\overline{U}_i}{\partial t}, \tag{2.13}$$

$$\overline{(\overline{U}_j + u_j)\frac{\partial(\overline{U}_i + u_i)}{\partial x_j}} = \overline{U}_j\frac{\partial\overline{U}_i}{\partial x_j} + \frac{\partial(\overline{u_i u_j})}{\partial x_j}, \tag{2.14}$$

$$\overline{\frac{\partial(\overline{P} + p)}{\partial x_i}} = \frac{\partial\overline{P}}{\partial x_i} + \frac{\partial\overline{p}}{\partial x_i} = \frac{\partial\overline{P}}{\partial x_i}, \tag{2.15}$$

and

$$\nu\overline{\frac{\partial^2(\overline{U}_i + u_i)}{\partial x_j \partial x_j}} = \nu\frac{\partial^2(\overline{U}_i)}{\partial x_j^2}. \tag{2.16}$$

Combining those 2.13, 2.14, 2.15 and 2.16 results in

$$\frac{\partial\overline{U}_i}{\partial t} + \overline{U}_j\frac{\partial\overline{U}_i}{\partial x_j} + \frac{\partial(\overline{u_i u_j})}{\partial x_j} = -\frac{1}{\rho_0}\frac{\partial\overline{P}}{\partial x_i} + \nu\frac{\partial^2\overline{U}_i}{\partial x_j^2}, \tag{2.17}$$

and after rearrangement

$$\rho_0\frac{D\overline{U}_i}{Dt} = \frac{-\partial\overline{P}}{\partial x_i}\delta_{ij} + \frac{\partial}{\partial x_j}\left(\mu\frac{\partial\overline{U}_i}{\partial x_j} - \rho_0\overline{u_i u_j}\right) \tag{2.18}$$

The implicit form of equation 2.18 is

$$\rho_0\frac{D\overline{U}_i}{Dt} = \frac{\partial\,\overline{\tau}_{ij}}{\partial x_j}, \tag{2.19}$$

where

$$\overline{\tau}_{ij} = -\overline{P}\delta_{ij} + \mu\left(\frac{\partial\overline{U_i}}{\partial x_j} + \frac{\partial\overline{U_j}}{\partial x_i}\right) - \rho_0\overline{u_i u_j}. \tag{2.20}$$

When considering the instantaneous form of equation 2.20

$$\tau_{ij} = -P\delta_{ij} + \mu\left(\frac{\partial U_i}{\partial x_j} + \frac{\partial U_j}{\partial x_i}\right), \tag{2.21}$$

it can be seen that an additional stress term of $\rho_0\overline{u_i u_j}$ comes into picture which is called Reynolds stress tensor. The components of this tensor in the Cartesian form are

$$\left[\overline{u_i u_j}\right] = \begin{bmatrix} \overline{u}^2 & \overline{uv} & \overline{uw} \\ \overline{uv} & \overline{v}^2 & \overline{vw} \\ \overline{uw} & \overline{vw} & \overline{w}^2 \end{bmatrix}. \tag{2.22}$$

The diagonal components of this tensor are called Reynolds normal stress while the off diagonal ones represent the Reynolds shear stresses.

2.2.2.2 Turbulent Kinetic Energy

Comprehension of the causes of generation and dissipation of the kinetic energy in the mean flow requires additional manipulation of the equation of motion of mean flow [18]. Before multiplying both sides of it by $\overline{U}_i$ lets recall equations 2.19 and 2.20

$$\frac{\partial\overline{U}_i}{\partial t} + \overline{U}_j\frac{\partial\overline{U}_i}{\partial x_j} = \frac{1}{\rho_0}\frac{\partial\overline{\tau}_{ij}}{\partial x_j}, \tag{2.23}$$

After multiplication by $\overline{U}_i$ the obtained equation is

$$\frac{\partial\left(\frac{1}{2}\overline{U}_i^2\right)}{\partial t} + \overline{U}_j\frac{\partial\left(\frac{1}{2}\overline{U}_i^2\right)}{\partial x_j} = \frac{1}{\rho_0}\frac{\partial(\overline{U}_i\overline{\tau}_{ij})}{\partial x_j} - \frac{1}{\rho_0}\overline{\tau}_{ij}\frac{\partial\overline{U}_i}{\partial x_j}. \tag{2.24}$$

In order to simplify the newly existing equation it is needed to introduce the mean strain rate as

$$\overline{S}_{ij} = \frac{1}{2}\left(\frac{\partial \overline{U_i}}{\partial x_j} + \frac{\partial \overline{U_j}}{\partial x_i}\right) \tag{2.25}$$

After rearrangement, simplification and recalling equation 2.5, the resulting equation of kinetic energy balance has the form of

$$\frac{D}{Dt}\left(\frac{1}{2}\overline{U_i}^2\right) = \frac{\partial\left[-\frac{\overline{U_i}\overline{P}}{\rho_0} + 2\nu\overline{U_i}\overline{S}_{ij} - \overline{u_i u_j}\overline{U_i}\right]}{\partial x_j} - 2\nu\overline{S}_{ij}\overline{S}_{ij} + \overline{u_i u_j}\frac{\partial\overline{U_i}}{\partial x_j}. \tag{2.26}$$

The left hand side of the equation indicates the variation of the mean kinetic energy, which is a result of various mechanisms represented in the right hand side of the equation [18]. The first three terms are called the transport term altogether, is responsible for the re-distribution of the kinetic energy. The fourth term represents the viscous dissipation and the fifth term indicates the loss of mean kinetic energy, in other words, gain of turbulent kinetic energy where the turbulent kinetic energy is defined as the half of the trace of Reynolds stress tensor [19].

The kinetic energy of the fluid flow is

$$E \equiv \frac{1}{2}U_i U_i. \tag{2.27}$$

It can be written in the form of

$$E = \overline{E} + k, \tag{2.28}$$

where $\overline{E}$ represents the kinetic energy of the mean flow and

$$k = \frac{1}{2}\overline{u_i u_i} = \frac{1}{2}(\overline{uu} + \overline{vv} + \overline{ww}). \tag{2.29}$$

represents the turbulent kinetic energy,

which is an important parameter for turbulence generation. The $\overline{V}$ and $\overline{W}$ are mean vertical and horizontal velocities respectively.

In order to determine the Reynolds' stresses, mean strain-rate (eqn. 2.25) and the turbulent kinetic energy (eqn. 2.29), first of all the mean velocities $\overline{U}$, $\overline{V}$, and $\overline{W}$ are calculated from the instantaneous data by using

$$\overline{U_i} = \frac{1}{N}\sum_{k=1}^{N}(U_i)_k. \tag{2.30}$$

Hence the Reynolds' stress $\overline{u_i u_j}$ is

$$\overline{u_i u_j} = \frac{1}{N}\sum_{k=1}^{N}[(U_i)_k - \overline{U_i}][(U_j)_k - \overline{U_j}] \tag{2.31}$$

where N=10000 represents the number of samples obtained at each grid point.

CHAPTER 3

FAR FIELD ANALYSIS OF JET FLOW

A reliability study for the current data set is performed by comparing farfield data to the data presented in Hussein et al. [5], Wygnanski et al. [2] and Pope [19]. In order to fulfil this task, one half of the jet data is acquired for the streamwise locations from x/d = 15 to 50.

Data obtained at far field region are suffered from high level of scatter, which is most likely due to the experimental error and relatively low speed of jet flow at far field region. This is tried to be reduced by changing the data acquisition intervals, modes and applying digital filter.

After the comparison of the results for the round jet with stated references, a comparison is also made for the round, square and triangular jets as well.

3.1 Reduction of Scatter

It is observed that, in the results obtained from the preliminary experiments conducted at the far field region of the jet flow have high levels of scatter after the x/d = 35. Curve fitting process and calculation of flow characteristics might be misleading due to the scatter.

In order to reduce scatter appearing after the x/d = 35, preliminary experiments are conducted at x/d = 40 of the round jet based on three modes:

- Using band and low pass digital filters,
- decreasing the number of data acquisition points,
- increasing the data acquisition interval (sampling time).

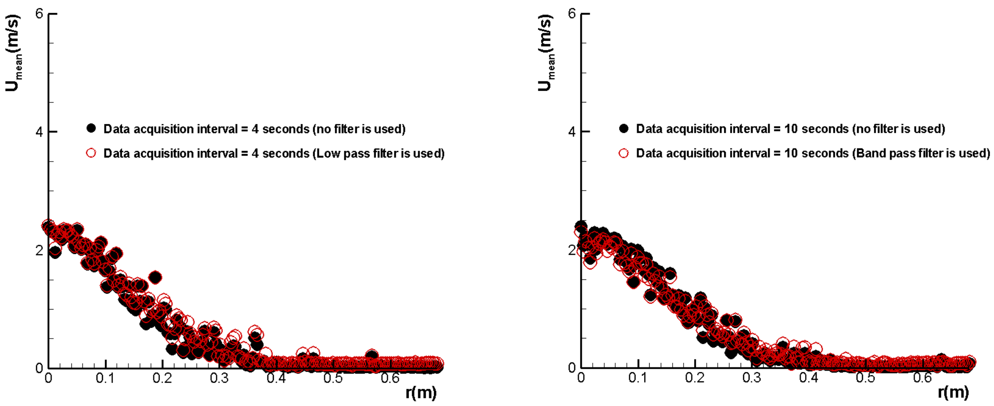

(a) Data acquisition interval = $4 seconds$ (b) Data acquisition interval = $10 seconds$

Figure 3.1: Comparison of data with and without filters.

The effects of low or band pass digital filtering is observed to be minimal. Digital filtering seems to shift all data to a higher or lower value, in general. Low pass filters use a cut-off frequency defined in equation 3.1, while band pass filters use cut-off frequencies defined both in equations 3.1 and 3.2.

$$f_{cut-off} = f_{max} \tag{3.1}$$

$$f_{cut-off} = \frac{5}{2t_{record}} \tag{3.2}$$

The results obtained using 4 seconds of data acquisition with and without low-pass filtering is shown in Figure 3.1 (a) whereas the result with 10 seconds of data acquisition with and without band-pass filtering is shown in Figure 3.1 (b). It can be clearly seen that either band-pass or low-pass filters have minimal effect in terms of reducing the scatter. Digitally filtered data are acquired simultaneously with the corresponding non-filtered data.

In the Table 3.1 standard deviation and correlation coefficient values are shown. They are calculated due to the best curve fit. As presented in the table, digital filtering has no significant effect on scattering as well as reducing data acquisition points. On the other hand increasing data acquisition duration causes reduction of scatter and thus implementing a suitable curve-fit. Reduction of scatter with increasing data acquisition time is shown in Figure 3.2.

Table 3.1: Data acquisition modes with statistical comparison.

Data Acquisition Points	Data Acquisition Interval	Data Acquisition Type	Standard Error	Correlation Coefficient
90	2 seconds	without filter	0.149	0.981
90	2 seconds	band pass	0.139	0.981
90	2 seconds	without filter	0.156	0.981
90	2 seconds	low pass	0.161	0.979
180	2 seconds	without filter	0.151	0.982
180	2 seconds	band pass	0.143	0.981
180	2 seconds	without filter	0.147	0.982
180	2 seconds	low pass	0.152	0.980
180	4 seconds	without filter	0.115	0.989
180	4 seconds	band pass	0.103	0.990
180	4 seconds	without filter	0.111	0.990
180	4 seconds	low pass	0.108	0.991
180	10 seconds	without filter	0.104	0.991
180	10 seconds	band pass	0.091	0.992
180	10 seconds	without filter	0.093	0.993
180	10 seconds	low pass	0.098	0.992

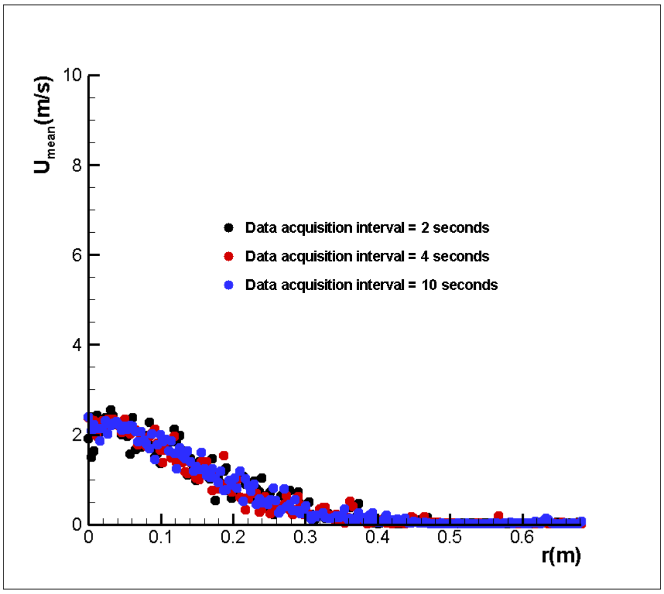

Figure 3.2: Comparison of $\overline{U}$ with 2, 4, and 10 seconds of data acquisition duration.

According to results obtained from those preliminary experiments, the far field experiments are conducted with a sampling rate of 5 khz and 10 seconds of data acquisition interval in order to reduce scattering.

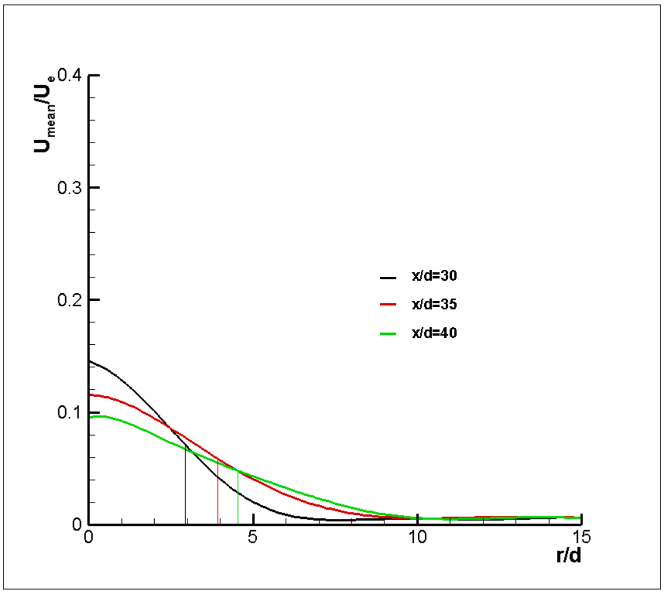

Figure 3.3: Indication of $r_{1/2}(x)$ for mean axial velocity in round jet at $x/d = 30$, $x/d = 35$, $x/d = 40$.

3.2 Verification Of Data

3.2.1 The Mean Velocity Profile

Considering the mean axial velocity field $\overline{U}(x, y, z)$ for the cylindrical coordinates $\overline{U}(x, r, \theta)$ [19], the centerline velocity is

$$U_0(x) \equiv \overline{U}(x, 0, 0), \tag{3.3}$$

where U_0 can also be adopted as the local maximum of the axial velocity. Accordingly the half velocity width $r_{1/2}$ is defined as

$$\overline{U}(x, r_{1/2}(x), 0) = \frac{1}{2} U_0(x). \tag{3.4}$$

The normalizing value in Figure 3.3 represents the jet exit velocity, U_e .

In Figure 3.3 it can be seen that along the streamwise direction, the mean velocity profile changes as the jet spreads, but the shape of it should remain the same beyond $x/d > 30$ for round jets [19]. This behaviour of the velocity profile is defined as self-similarity.

In order to obtain the self-similar profile of the jet flow, the mean axial velocity is normalised by U_0, and Reynolds stresses and turbulence kinetic energy (k) by ${U_0}^2$. The radial coordinate, on the other hand, is non-dimensionalized by $r_{1/2}$.

The self similarity concept is very important as it provides a strong relation between the mean velocity profiles, Reynolds shear and normal stresses of a jet between different streamwise locations. Moreover it can also be said that the self similar mean velocity profile is Re independent after comparison with the ones presented by Hussein [5] and Wygnanski et al [2] which are obtained at higher Re.

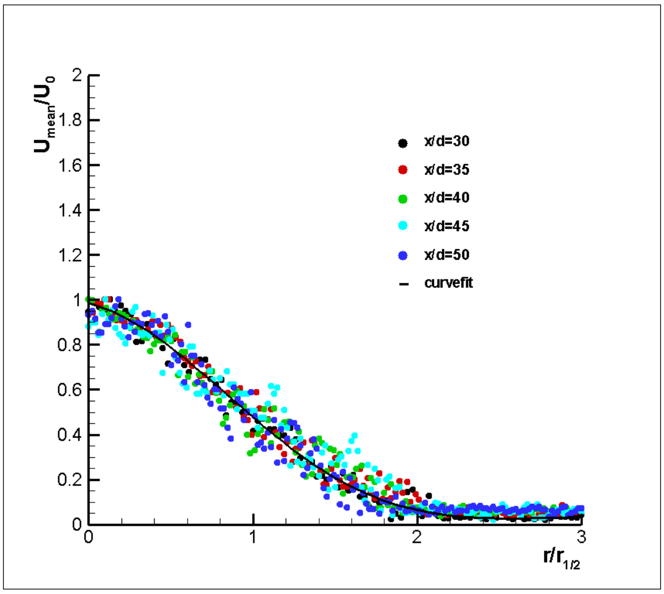

Figure 3.4: The self-similar profile of round jet at Re=5.5×10^4.

The obtained self-similar mean velocity profiles are presented in Figure 3.4 with a curve-fit. The result provides a good consistency with the ones obtained by Hussein et al. [5] and Wygnanski et al [2] as it can be seen in Figure 3.5.

In Figure 3.6 $U_e/U_0(x)$ is plotted versus x/d. In spite of the overlapping behaviour of the self similar mean velocity profiles, there is a difference between the curves.

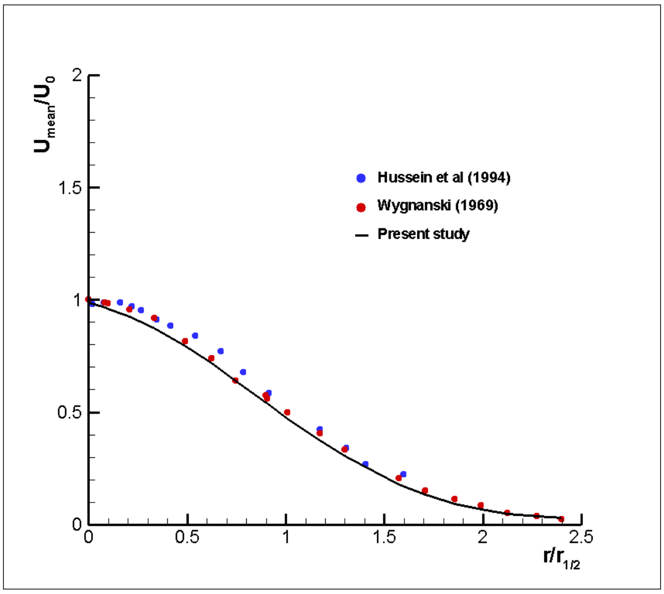

Figure 3.5: Comparison of self-similar mean velocity profile with the ones of Hussein et al [5] and Wygnanski et al [2].

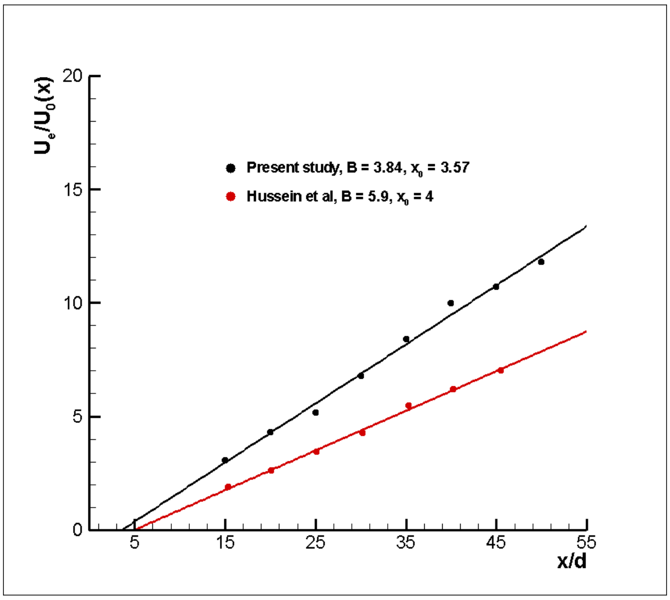

Figure 3.6: Variation of mean velocity along the axial distance in comparison with Hussein et al. [5].

Together with Figure 3.6 two new parameters are also introduced in order to comprehend the axial behaviour of the mean flow. The velocity decay constant B is derived directly from the linear curve and defined as

$$\frac{U_0(x)}{U_e} = \frac{B}{(x - x_0)/d}, (x > x_0), \tag{3.5}$$

where x_0 is the intercept of the line with x axis and is called as the virtual origin [19].

It is also observed that the jet spreads linearly and the spreading rate is

$$r_{1/2}(x) = S_r(x - x_0), (x > x_0), \tag{3.6}$$

Table 3.2: The spreading rate S_r and velocity decay B comparison [5].

	Hussein et al. (1994) hot wire data	Hussein et al. (1994) laser-Doppler data	Round Jet Results hot wire data
Re	95500	95500	55000
S_r	0.102	0.094	0.116
B	5.90	5.80	3.84

When referring to the Table 3.2 and Figure 3.5 it is observed that there is a significant difference between velocity decay B with those of Hussein et al [5]. This difference is very likely due to the different types of nozzles used in studies of Hussein et al [5] and Wygnanski et al [2]. Unlike those studies, long pipe nozzles are used in this study. Although the length of the pipe is not enough to introduce a fully developed turbulent flow, at the jet exit turbulence levels ejecting from the pipe is higher, resulting a faster velocity decay.

On the other hand it is stated by Hussein et al [5] that after a sufficient Re ($Re > 10000$) the spreading rate is almost independent of Re. So, this slight difference between the S_r should be due to different types of nozzles that are used.

3.2.2 Reynolds Stresses

The self similarity concept also exhibits a good characteristic behaviour between the Reynolds stresses across $x/d > 30$ of the far field region.

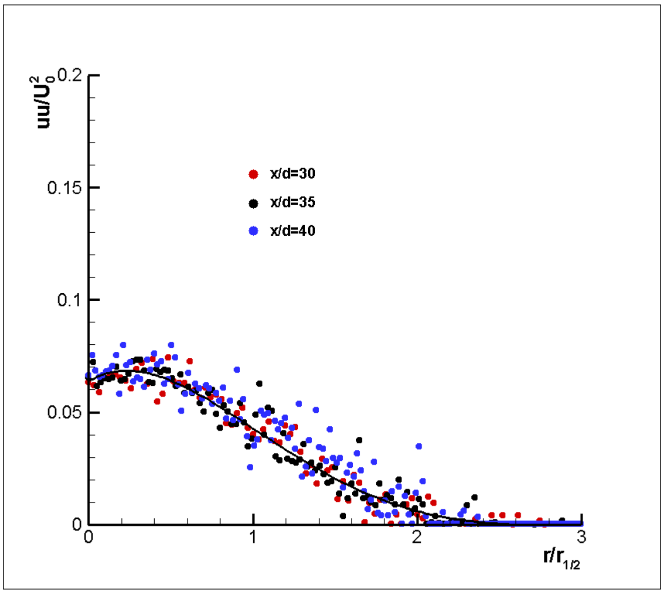

Figure 3.7: The curve-fit for $\overline{uu}$ of round jet.

In Figures 3.7, 3.8, 3.9 and 3.13 it can be clearly seen that Reynolds' normal stress and turbulent kinetic energy profiles are preserving their self-similar attitude to a good extent for 30, 35 and 40 diameters away from the nozzle exit, although there is some scatter.

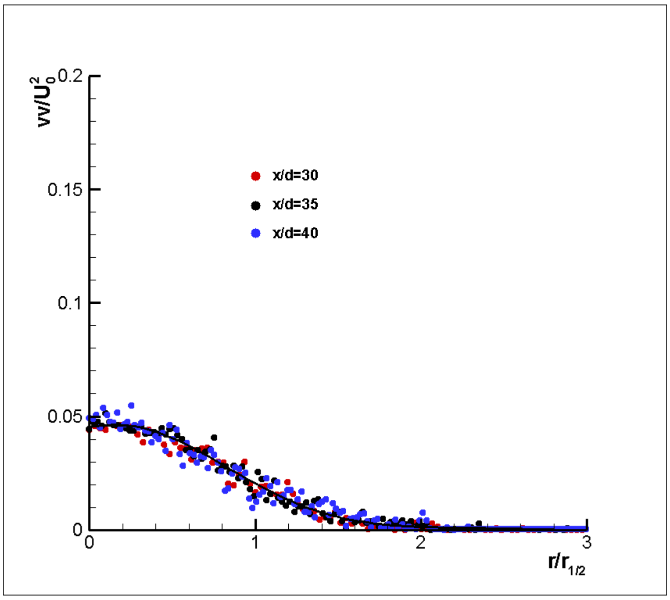

Figure 3.8: The curve-fit for $\overline{vv}$ of round jet.

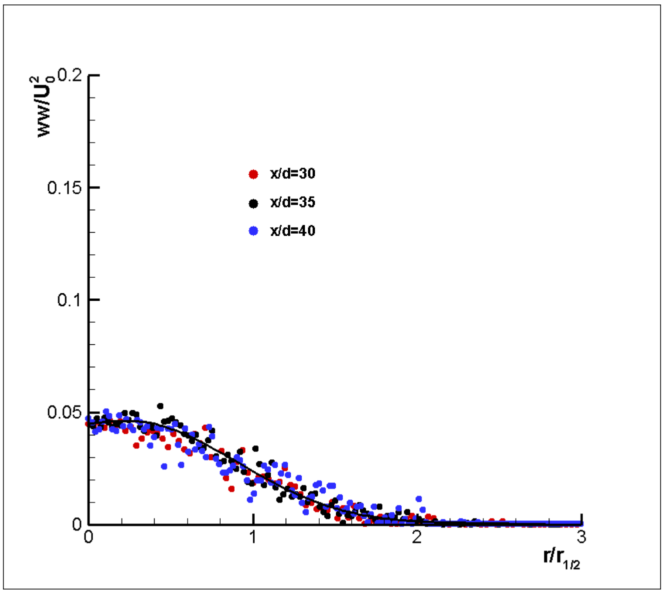

Figure 3.9: The curve-fit for $\overline{ww}$ of round jet.

On the other hand the comparison with the results of Hussein et al. [5] shows that difference between self-similar stress profiles, which are shown in the Figures 3.10, 3.11 and 3.12, are again caused by plane jet - pipe jet difference. Symmetrical behaviour of the curves about vertical axis in Figure 3.10 should not be perceived as overshooting.

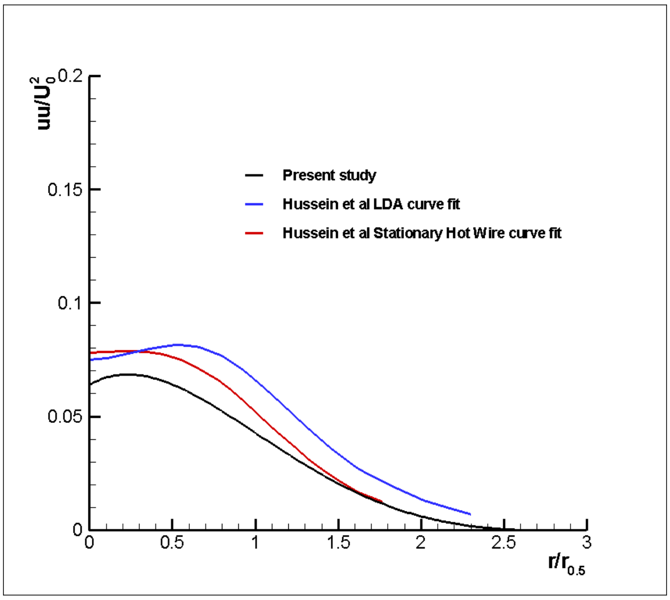

Figure 3.10: The comparison of $\overline{uu}$ of round jet results with those reported by Hussein et al. [5].

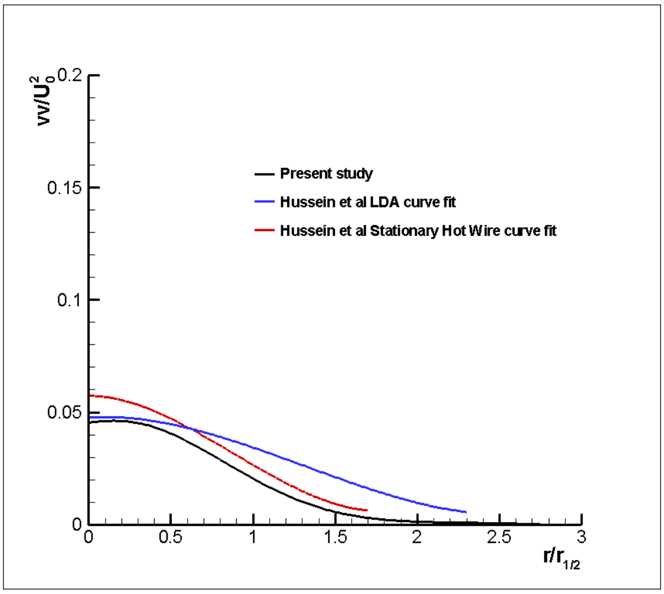

Figure 3.11: The comparison of $\overline{vv}$ of round jet results with those reported by Hussein et al. [5].

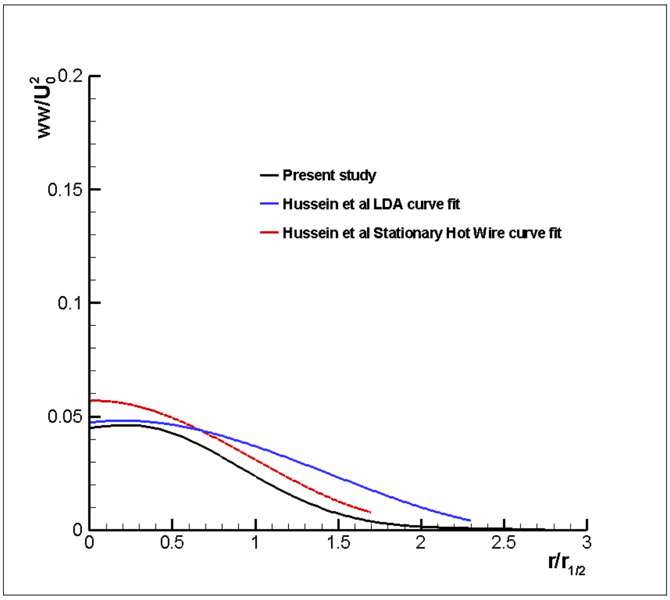

Figure 3.12: The comparison of $\overline{ww}$ of round jet results with those reported by Hussein et al. [5].

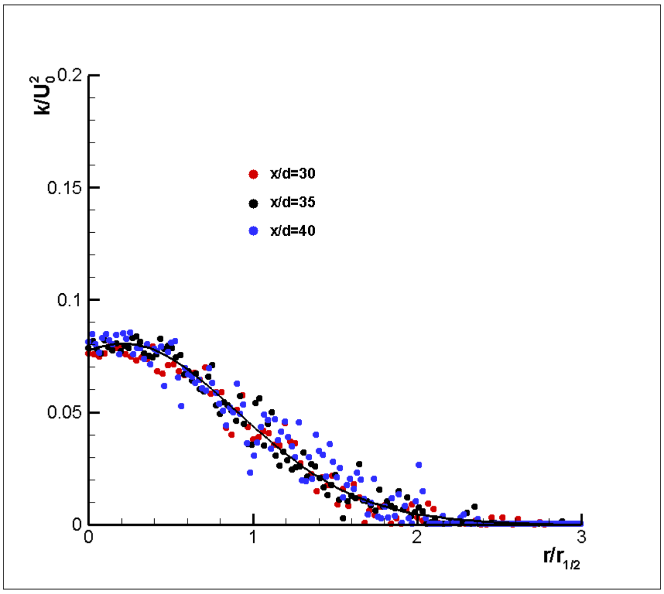

Figure 3.13: Curve fit for turbulent kinetic energy k of round jet.

In Figure 3.14 the derived Reynolds normal stress curve-fits, and the turbulent kinetic energy are represented together. The turbulent kinetic energy k is found directly from equation 2.29.

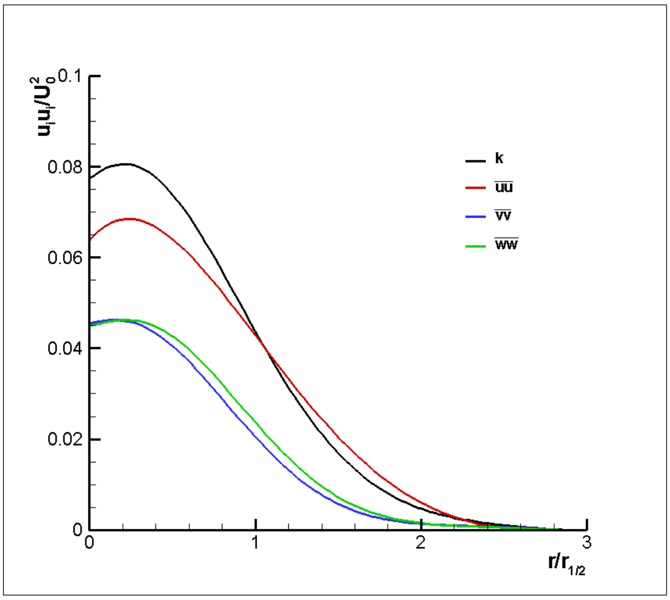

Figure 3.14: Reynolds normal stresses $\overline{u_i u_i}$ and turbulent kinetic energy k of round jet.

3.3 Geometry Effects

3.3.1 The Mean Velocity Profile

After the verification of the round jet results, the data acquisition, data conversion and data reduction processes can be accepted as reliable and geometry effects on self-similarity and turbulent characteristics can be compared.

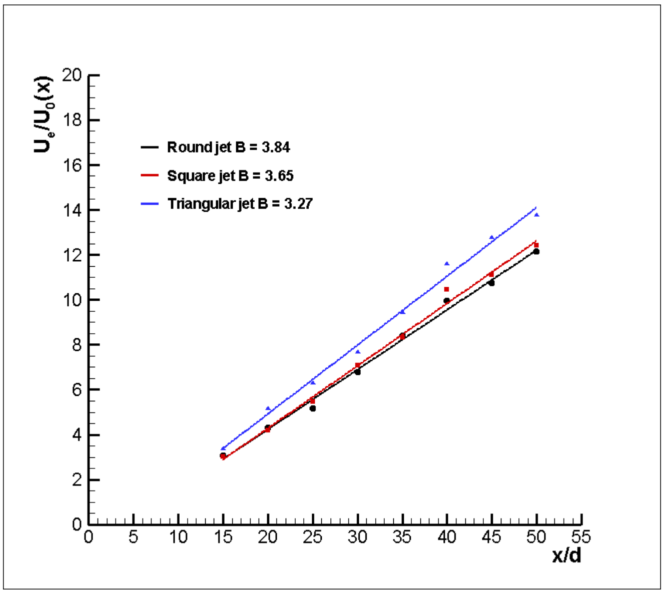

Figure 3.15: Variation of mean velocities of round, square and triangular jets along the axial distance.

The velocity decay rate B is compared in terms of different geometries in Figure 3.15 and in Table 3.3 the spread rate S is also presented together with B.

Table 3.3: Geometry effects on spreading rate S_r and velocity decay B [5].

	Hussein et al. (1994)	Round jet	Square jet	Triangular jet
Re	95500	55000	55000	55000
S_r	0.102	0.116	0.118	0.135
B	5.90	3.84	3.65	3.27

Relying on the results presented in the Figure 3.15 and Table 3.3 it can be stated that nozzle geometry directly effects the velocity decay rate with an utmost level for triangular jet. On the other hand, triangular jet unfolds a slight increase of spread rate S. That is, the triangular jet maintains the highest velocity decrease in axial direction and similarly it has the largest spread rate.

This outcome obtained from the far field analysis of the round, square, and triangular jets will result in the minimum core-length of the jet which is a indicator of enhanced mixing in the near fields of the jet flow [9]. The analysis of the near field will covered in chapter 4.

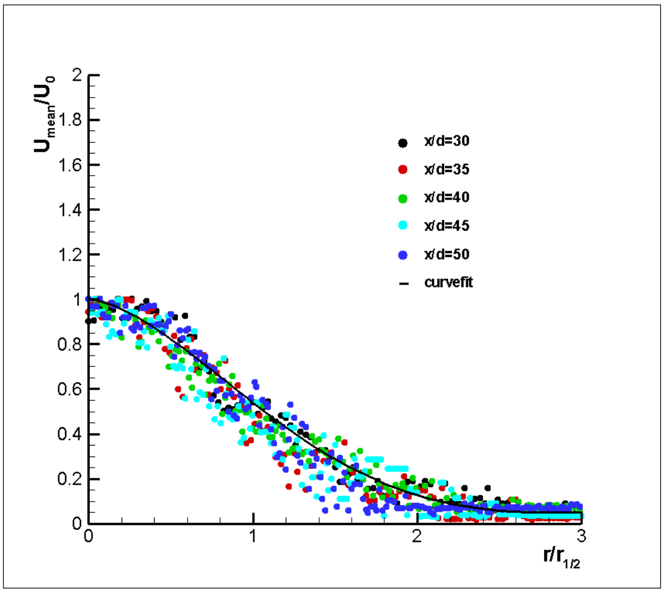

Figure 3.16: Self-similar velocity profile of square jet.

The self similarity phenomena also holds for different geometries and constitutes a universality for all round, square and triangular jets as can be seen in Figures 3.4, 3.16 and 3.17. The achieved curve-fit of the three jets show a good consistency with the self similarity on Figure 3.18.

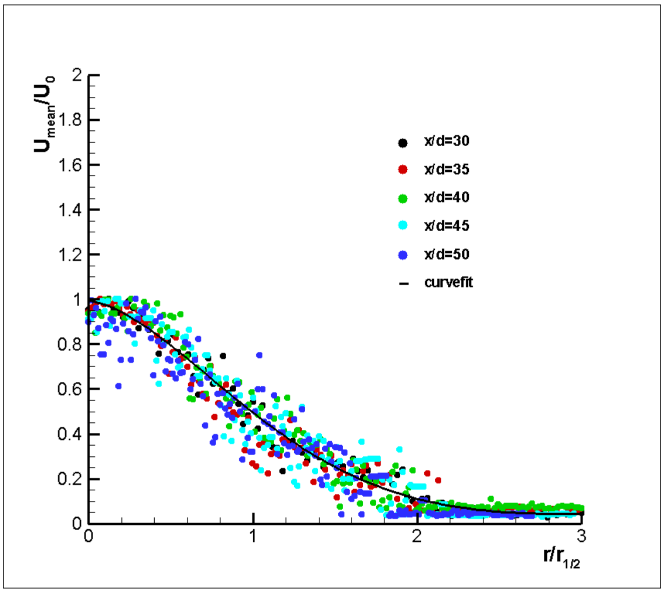

Figure 3.17: Self-similar velocity profile of triangular jet.

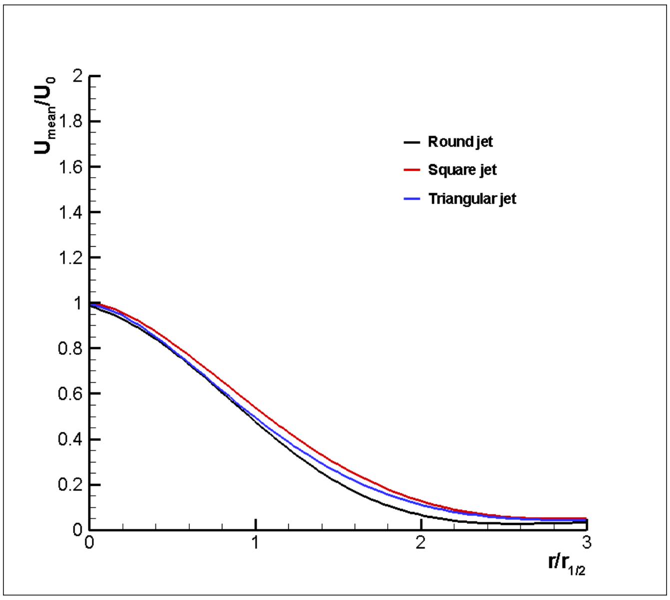

Figure 3.18: Geometry effects on self similarity.

3.3.2 Turbulent Kinetic Energies

Here, a curve-fit is performed on turbulent kinetic energy profiles of square and triangular jets, which are shown in Figures 3.19 and 3.20, and obtained curves for the k profiles of jets are compared in Figure 3.21.

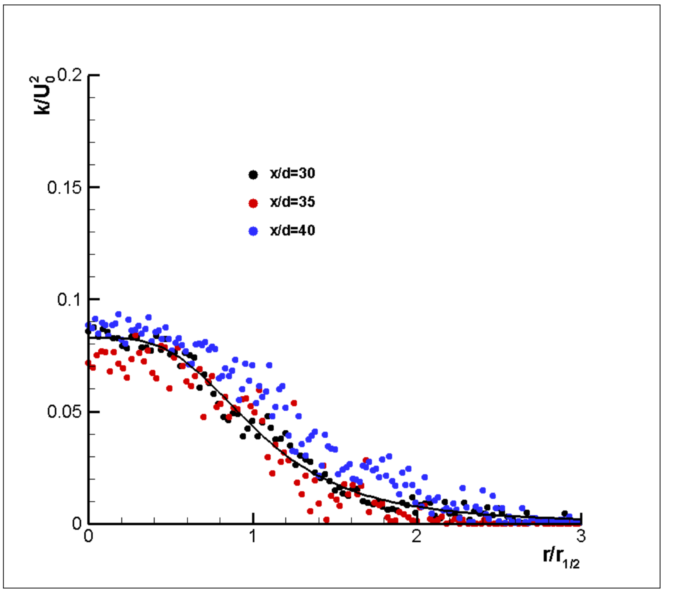

Figure 3.19: Turbulent kinetic energy *k* of square jet.

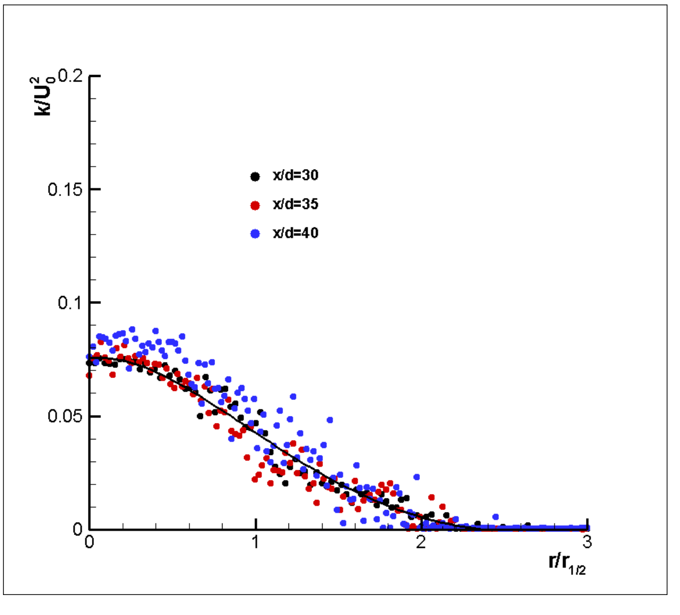

Figure 3.20: Turbulent kinetic energy *k* of triangular jet.

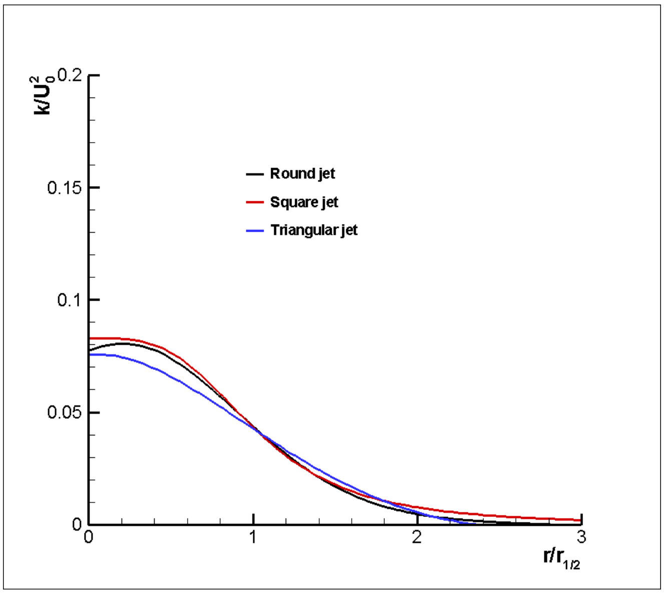

Figure 3.21: Geometry effects on turbulent kinetic energy *k*.

Although it is hard to say that the normalized k profiles for square and triangular jets exhibit good self similarity as round jet, they show that the self similarity concept forms a quite well universality for round, square and triangular jets. That is, the self similarity concept holds for different types of geometries when considering the jet flow.

As the normalized k profiles introduce a self similarity in the far field, it would be wise to consider the near field profiles in order to decide the mixing qualities of different types of jets.

CHAPTER 4

NEAR FIELD ANALYSIS OF JET FLOW

In this chapter, the near field analysis of the round, square and triangular jets are covered. Understanding the near field behaviour of the jet flow is crucial in order to perceive turbulence characteristics and the way that geometry effects liquid jet atomization [20].

In order attain widespread comprehension of turbulence and flow structure of the near field, the velocity field measurements are performed at 5 different stations (x/d =1, 2, 4, 6 and 10) away from the jet exit on cross-stream (lateral) planes. In addition to these lateral measurements, longitudinal measurements are conducted at the center-planes of all three types of jet flow. The mean velocity, Reynolds shear stress, vorticity and turbulent kinetic energy fields are obtained.

Longitudinal measurements provide better opportunity to understand the evolution of the jet core length which is an indicator of the near field mixing [9]. The mass entrainment rates of all three jets is also presented as an another indicator of turbulent mixing.

Finally the stress-strain relation is analysed at $x/d = 2$ for all three type of nozzles.

4.1 $x/d = 1$ Comparison

Before analysing the near field structures of the flow and turbulence characteristics, it would be wise to compare the centerline behaviour of the jets examined at $x/d = 1$ to point out the exit conditions if they are equally set or not. Because equally set exit conditions are the doorsteps to a reliable comparison of far and near field regions. It should also be considered that all three nozzles have designed based on a equivalent diameter which is picked due to equally set cross sectional area of the nozzles.

The three mean velocities, Reynolds shear stresses and turbulent kinetic energies are compared in order to see if the initial conditions are in agreement. In Figures 4.1, 4.2, 4.3, 4.4, 4.5, 4.6, and 4.7 it can be seen that the mismatch is within the acceptable limits and thus the experiments with those initial conditions offer comparable near-field and far-field data.

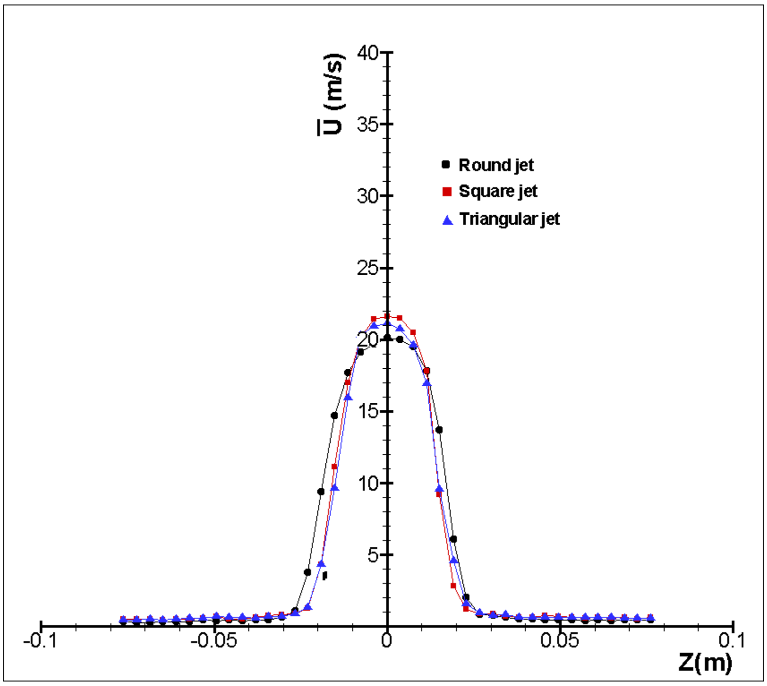

Figure 4.1: $x/d = 1$ comparison of $\overline{U}$.

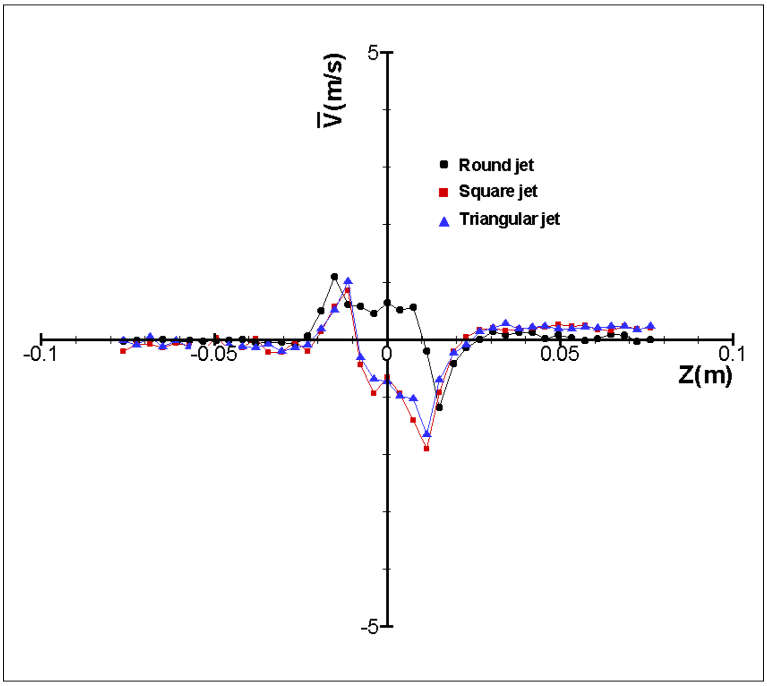

Figure 4.2: $x/d = 1$ comparison of $\overline{V}$.

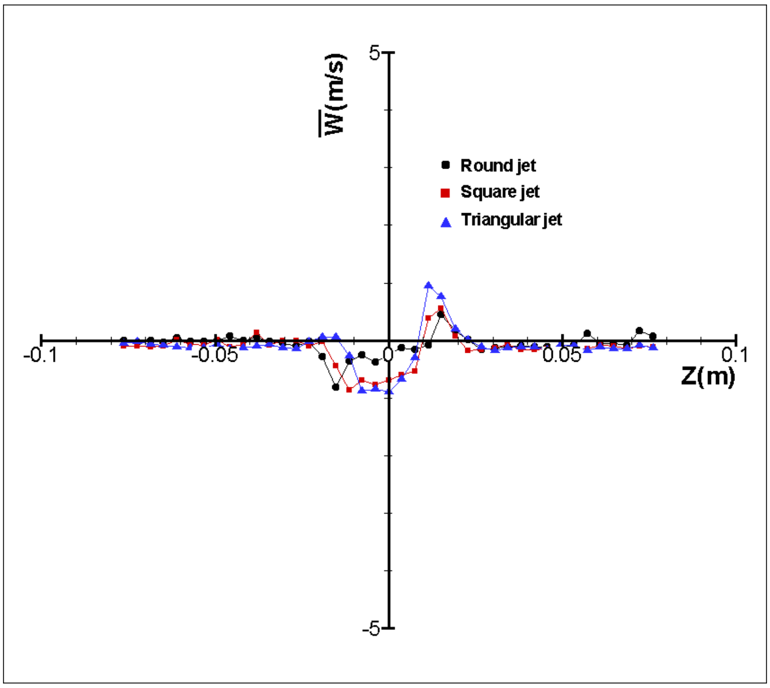

Figure 4.3: $x/d = 1$ comparison of $\overline{W}$.

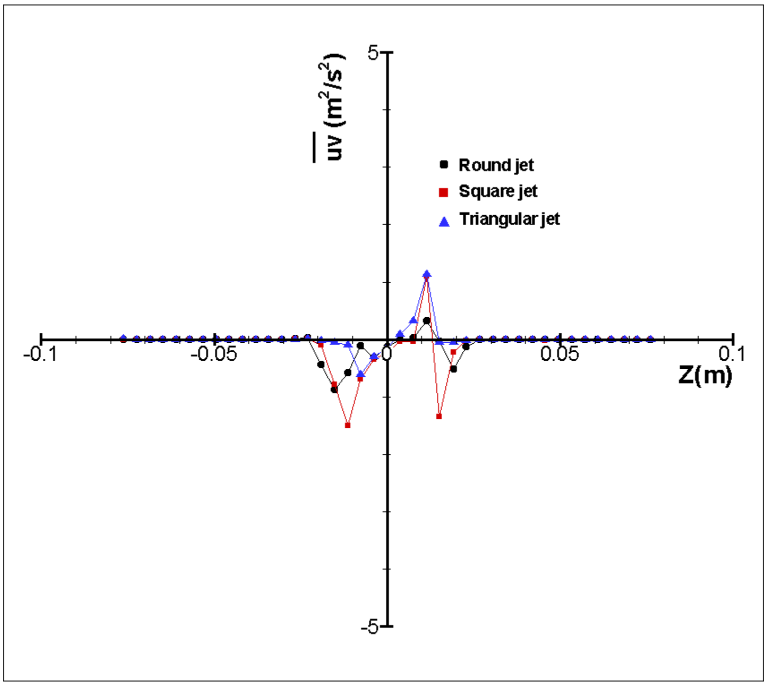

Figure 4.4: x/d = 1 comparison of $\overline{uv}$.

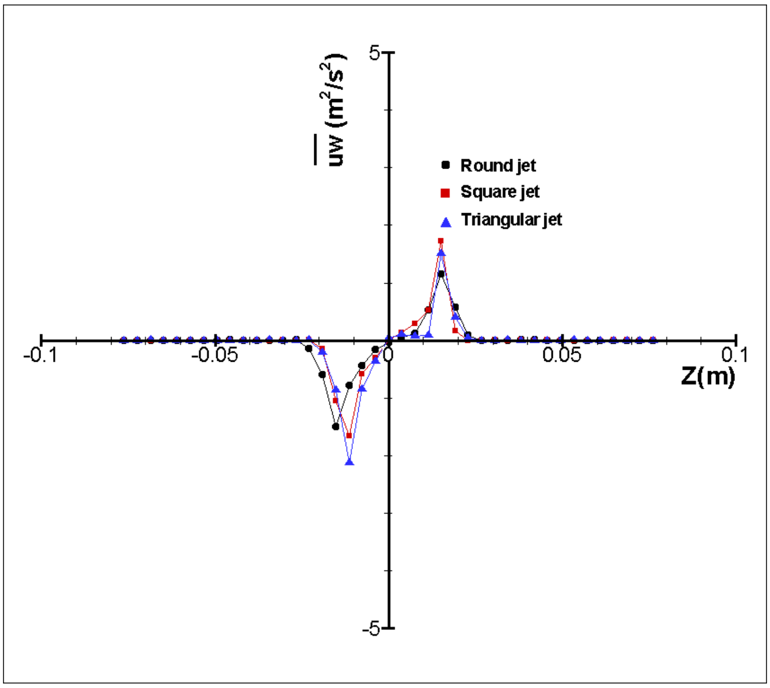

Figure 4.5: x/d = 1 comparison of $\overline{uw}$.

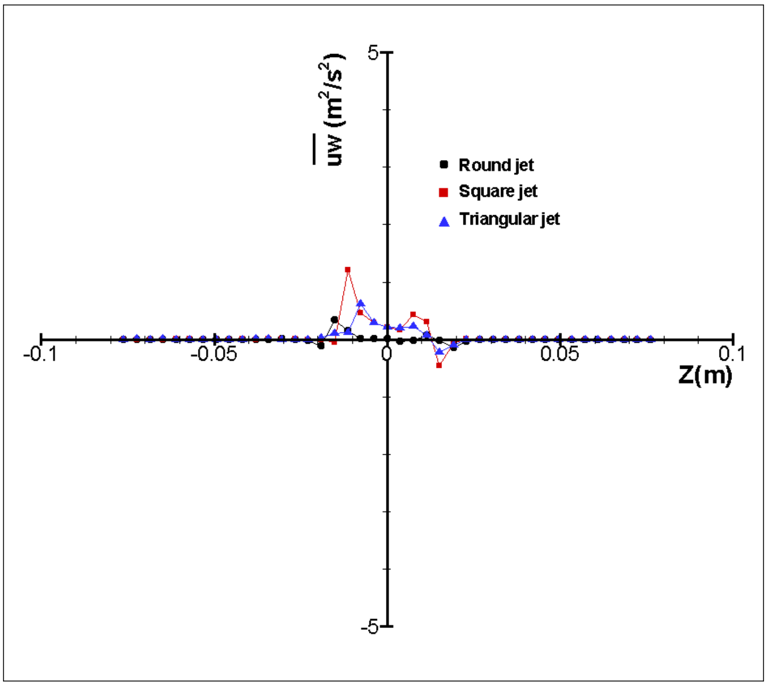

Figure 4.6: $x/d = 1$ comparison of $\overline{vw}$.

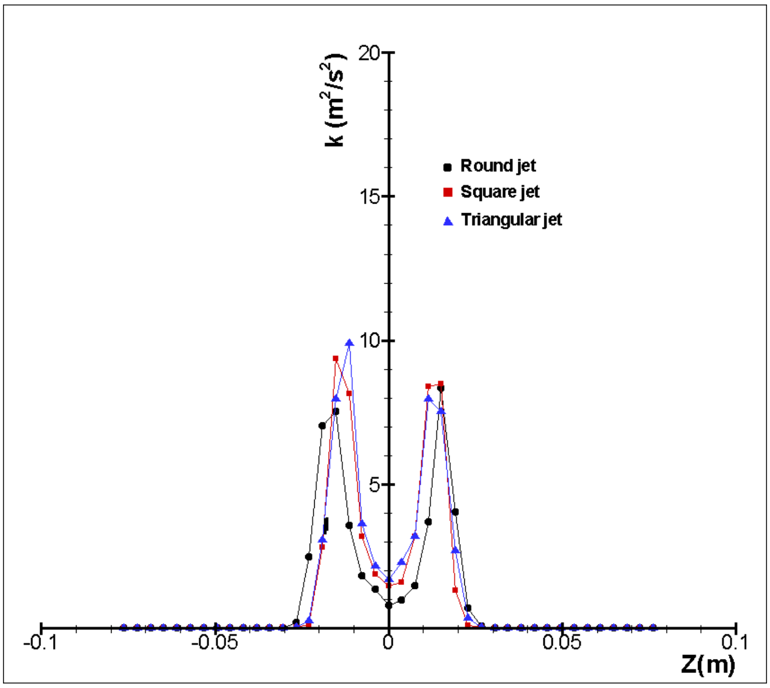

Figure 4.7: $x/d = 1$ comparison of turbulent kinetic energy.

4.2 Lateral Measurements

4.2.1 Mean Axial Velocity $\overline{U}$

Before examining the turbulent characteristics of the jet flow emanating from three different types of nozzles, it is mandatory to understand the behaviour of the mean axial velocity, namely $\overline{U}$.

It is revealed in chapter 3 that the triangular nozzle causes the highest velocity decay and the spreading rate of the jet flow at the far field. As the velocity decay behaviour is almost linear at near field [9], [19], the core length is a good parameter to understand the mixing characteristics of the jet flow.

The diffusion of all three types of jets are clearly evident from the figures 4.8, 4.9 and 4.10 as the jets move downstream. However the triangular jet seems to be diffused a little more when one compares the level of the centerline velocity levels of all three types of jets. Due to this diffusion, the core length of the triangular jet is exposed to a higher reduction. Smaller core length is stated as a result of enhanced mixing by Gutmark and Grinstein [7].

The rotation of the axes of the axial velocity field of non-circular jets, namely axis-switching phenomenon, which is stated as the fundamental reason of the improved entrainment for non-circular jets [7], is not observed at neither of the square and triangular jets. This result exposes a similarity with the study of Koshigoe et al [21] as the axis-switching is found to be related with orifice jets rather than pipe jets.

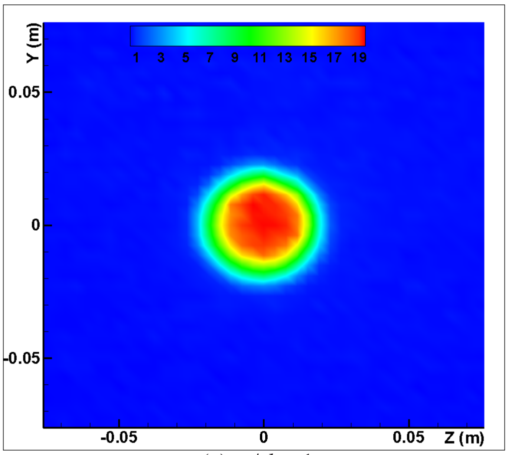

(a) $x/d = 1$

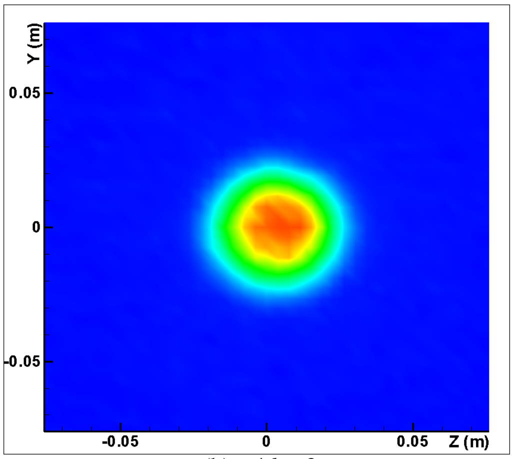

(b) $x/d = 2$

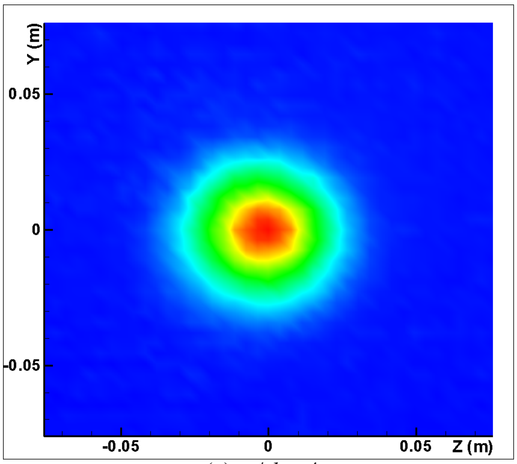

(c) $x/d = 4$

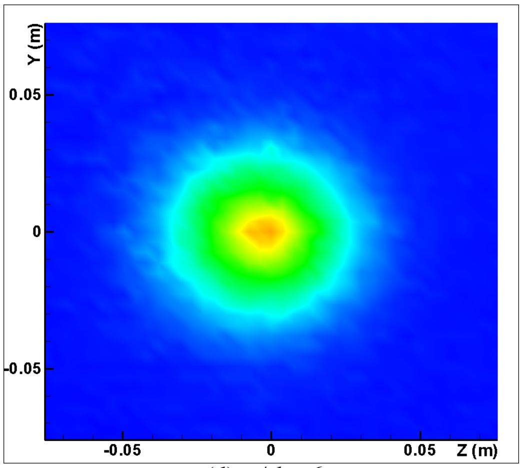

(d) $x/d = 6$

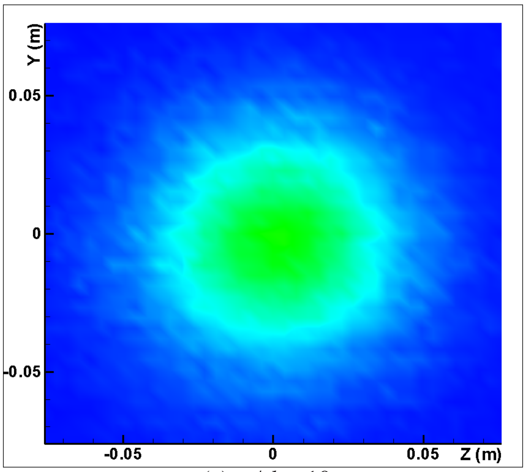

(e) $x/d = 10$

Figure 4.8: $\overline{U}$ field at various data acquisition stations (x/d = 1, 2, 4, 6 and 10) for round jet.

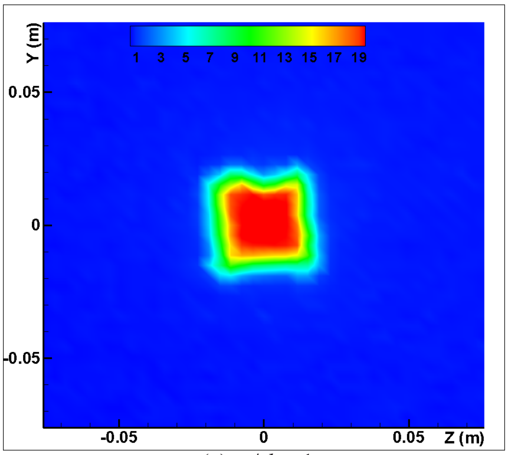

(a) $x/d = 1$

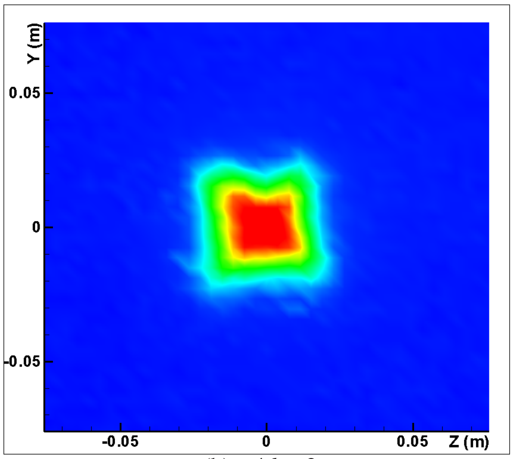

(b) $x/d = 2$

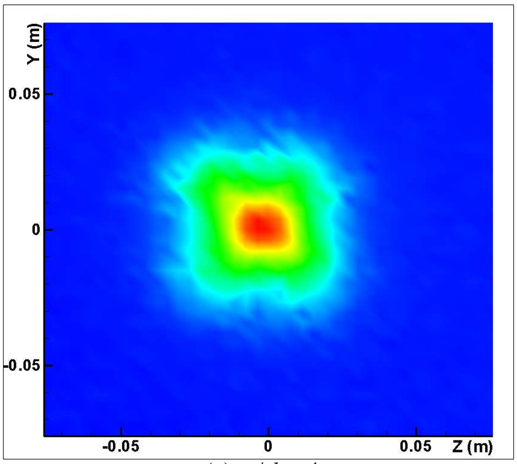

(c) $x/d = 4$

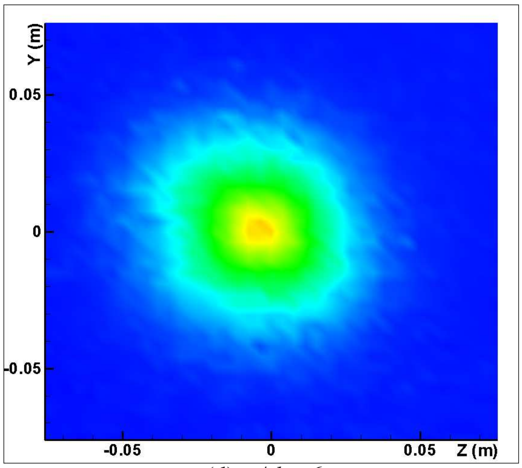

(d) $x/d = 6$

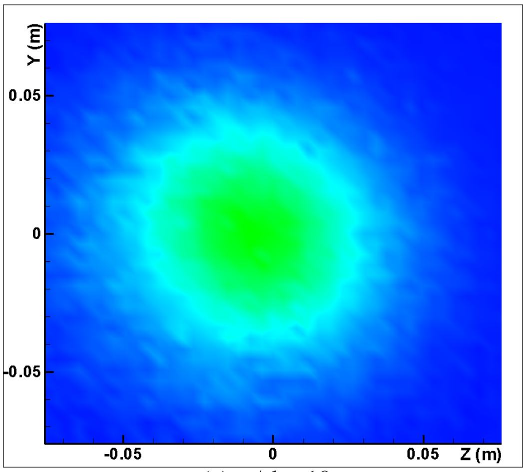

(e) $x/d = 10$

Figure 4.9: $\overline{U}$ field at various data acquisition stations (x/d = 1, 2, 4, 6 and 10) for square jet.

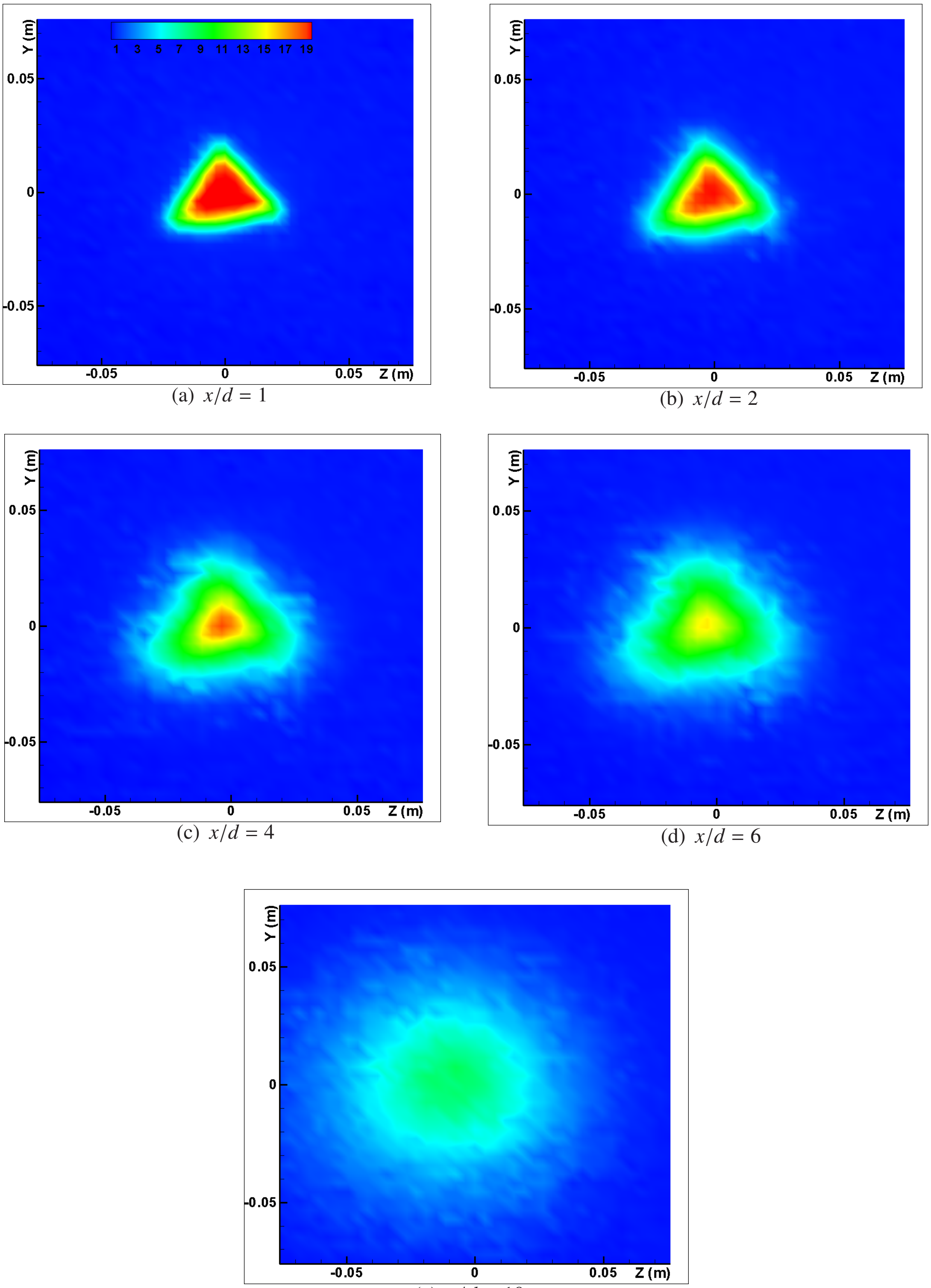

(a) $x/d = 1$

(b) $x/d = 2$

(c) $x/d = 4$

(d) $x/d = 6$

(e) $x/d = 10$

Figure 4.10: $\overline{U}$ field at various data acquisition stations (x/d = 1, 2, 4, 6 and 10) for triangular jet.

4.2.2 Mean Vertical $\overline{V}$ and Horizontal Velocities $\overline{W}$

The vertical and horizontal velocities of the jets are also obtained. Although the spreading rate S_r is a function of half velocity width and consequently axial velocity decay, the vertical and horizontal velocities may also have some influence on S_r considering the following contour plots. These effects are probably realized by means of axial vorticity which is the main reason of the reduction of core length and represented with equation 2.7.

On the other hand referring to Figures 4.11,4.12, 4.13, 4.14, 4.15, and 4.16, it can be said that decay of $\overline{V}$ and $\overline{W}$ velocities exhibit similar behaviour as $\overline{U}$. That is, decay of the lateral and horizontal velocities of triangular jet reduces more then the others. Also notice that, the magnitude of these velocities are considerably lower than the axial velocity, meaning that the relative error is larger.

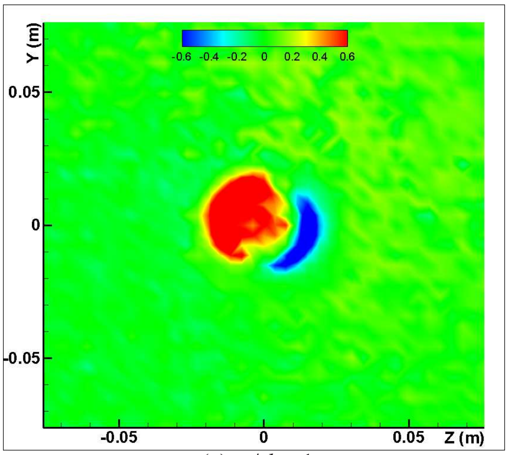

(a) $x/d = 1$

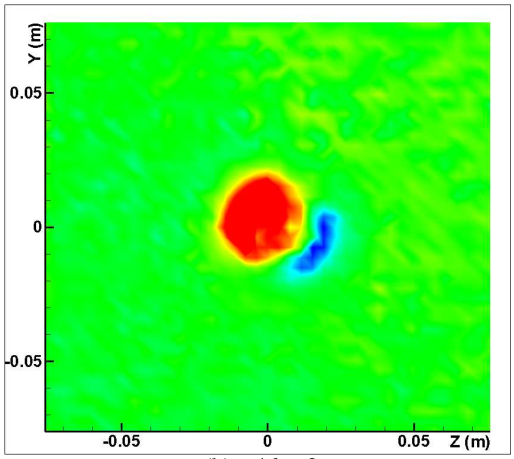

(b) $x/d = 2$

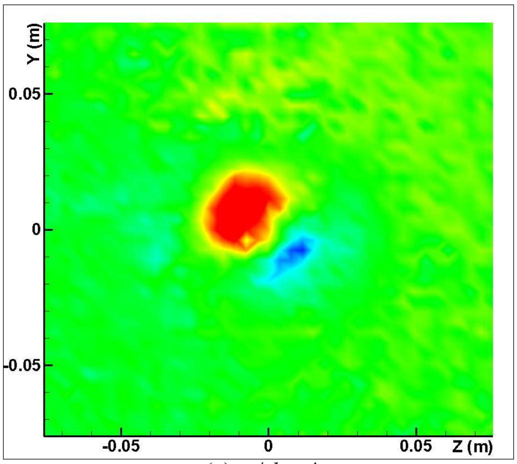

(c) $x/d = 4$

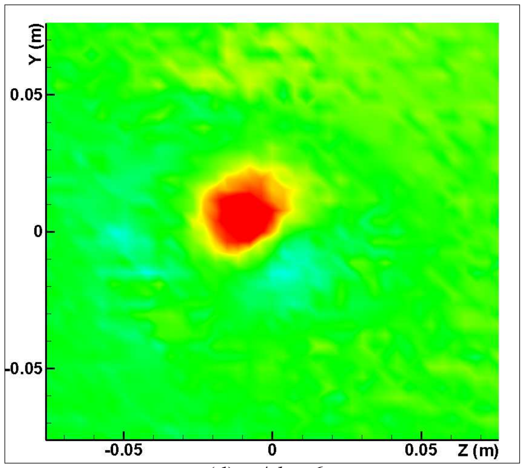

(d) $x/d = 6$

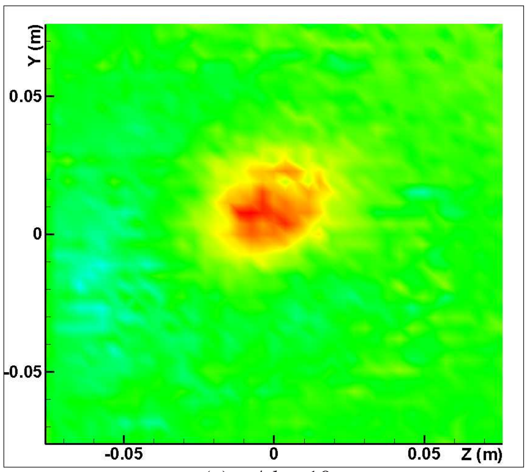

(e) $x/d = 10$

Figure 4.11: $\overline{V}$ field at various data acquisition stations (x/d = 1, 2, 4, 6 and 10) for round jet.

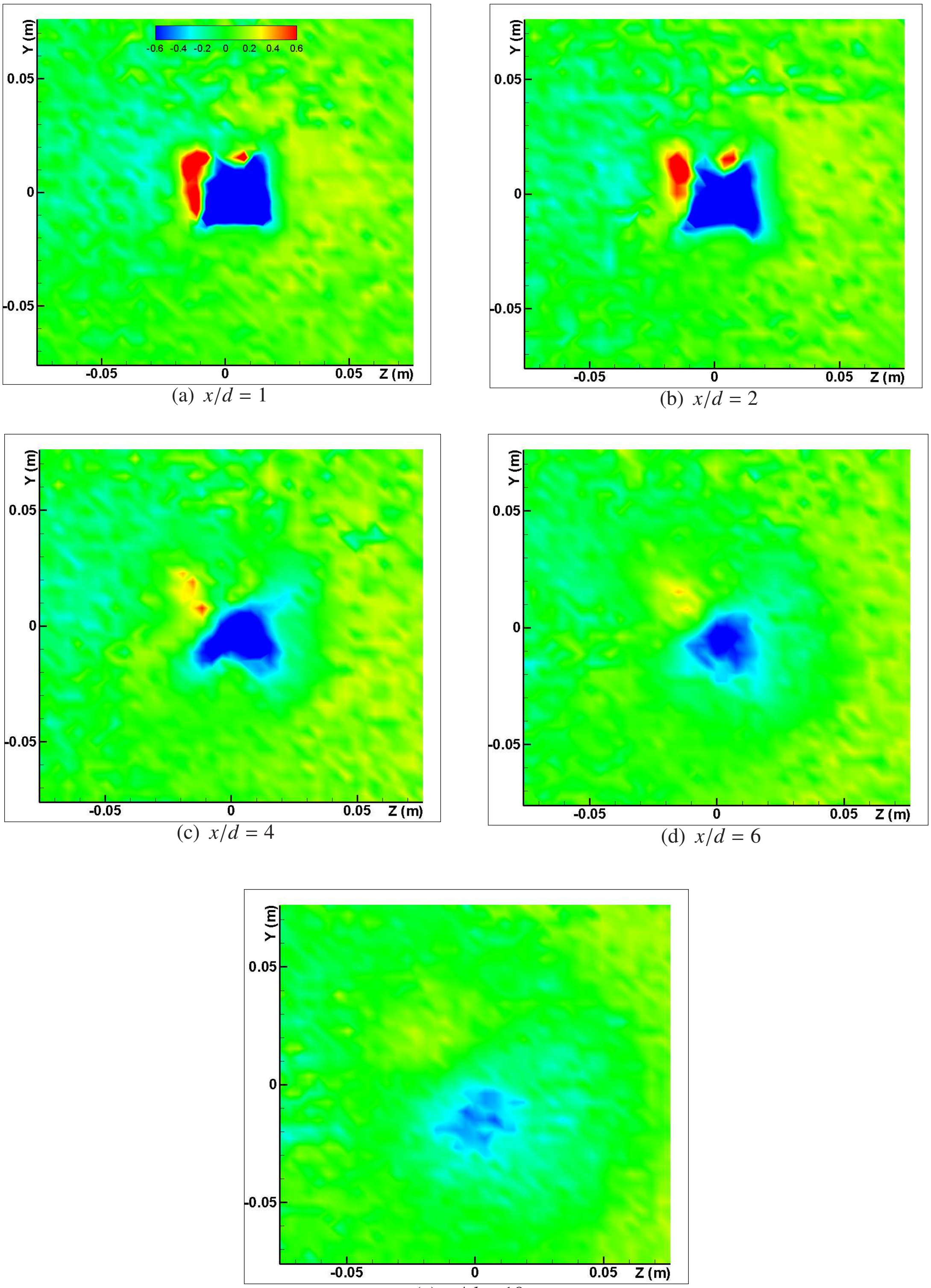

(a) $x/d = 1$

(b) $x/d = 2$

(c) $x/d = 4$

(d) $x/d = 6$

(e) $x/d = 10$

Figure 4.12: $\overline{V}$ field at various data acquisition stations (x/d = 1, 2, 4, 6 and 10) for square jet.

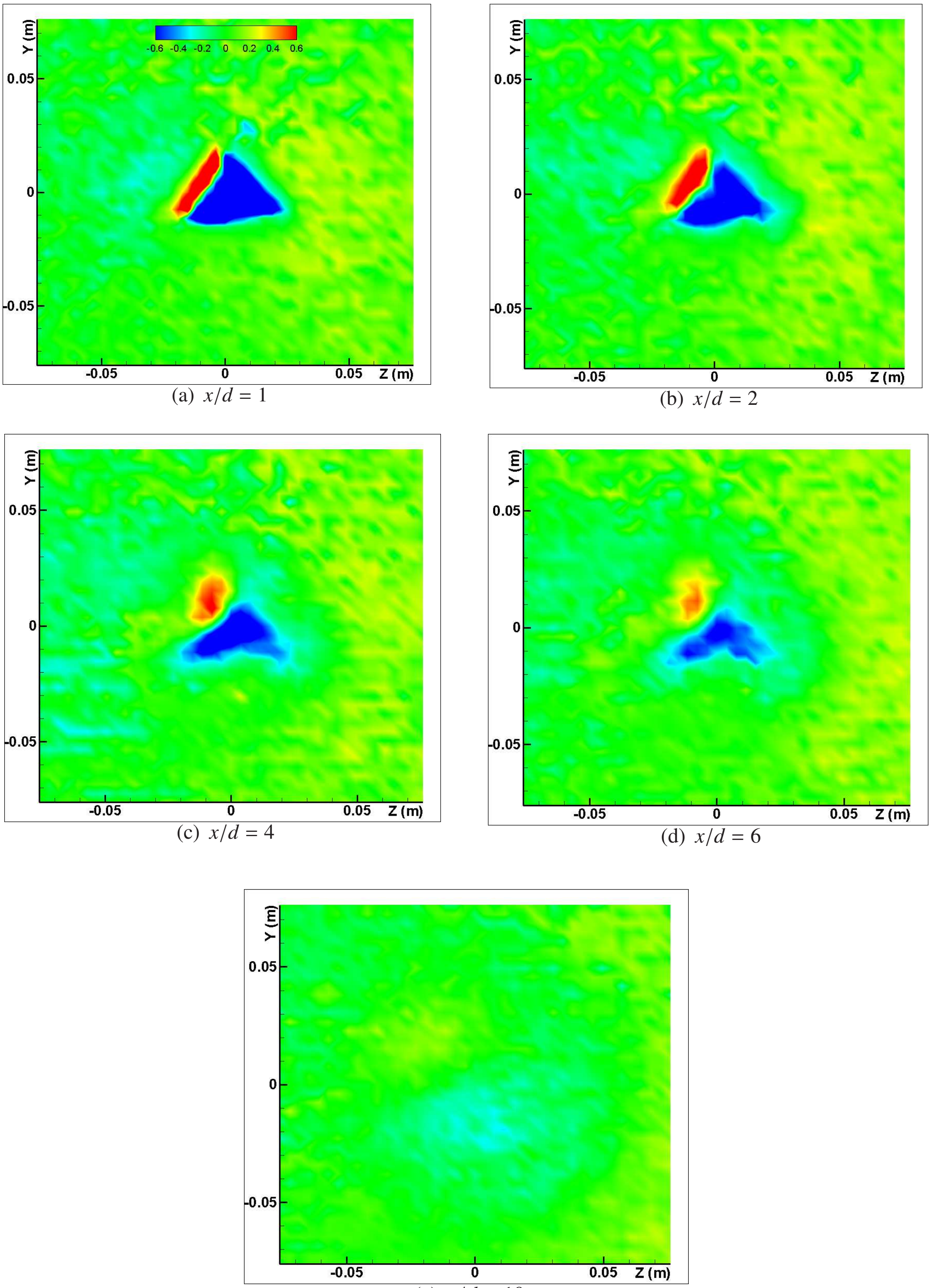

(a) $x/d = 1$

(b) $x/d = 2$

(c) $x/d = 4$

(d) $x/d = 6$

(e) $x/d = 10$

Figure 4.13: $\overline{V}$ field at various data acquisition stations (x/d = 1, 2, 4, 6 and 10) for triangular jet.

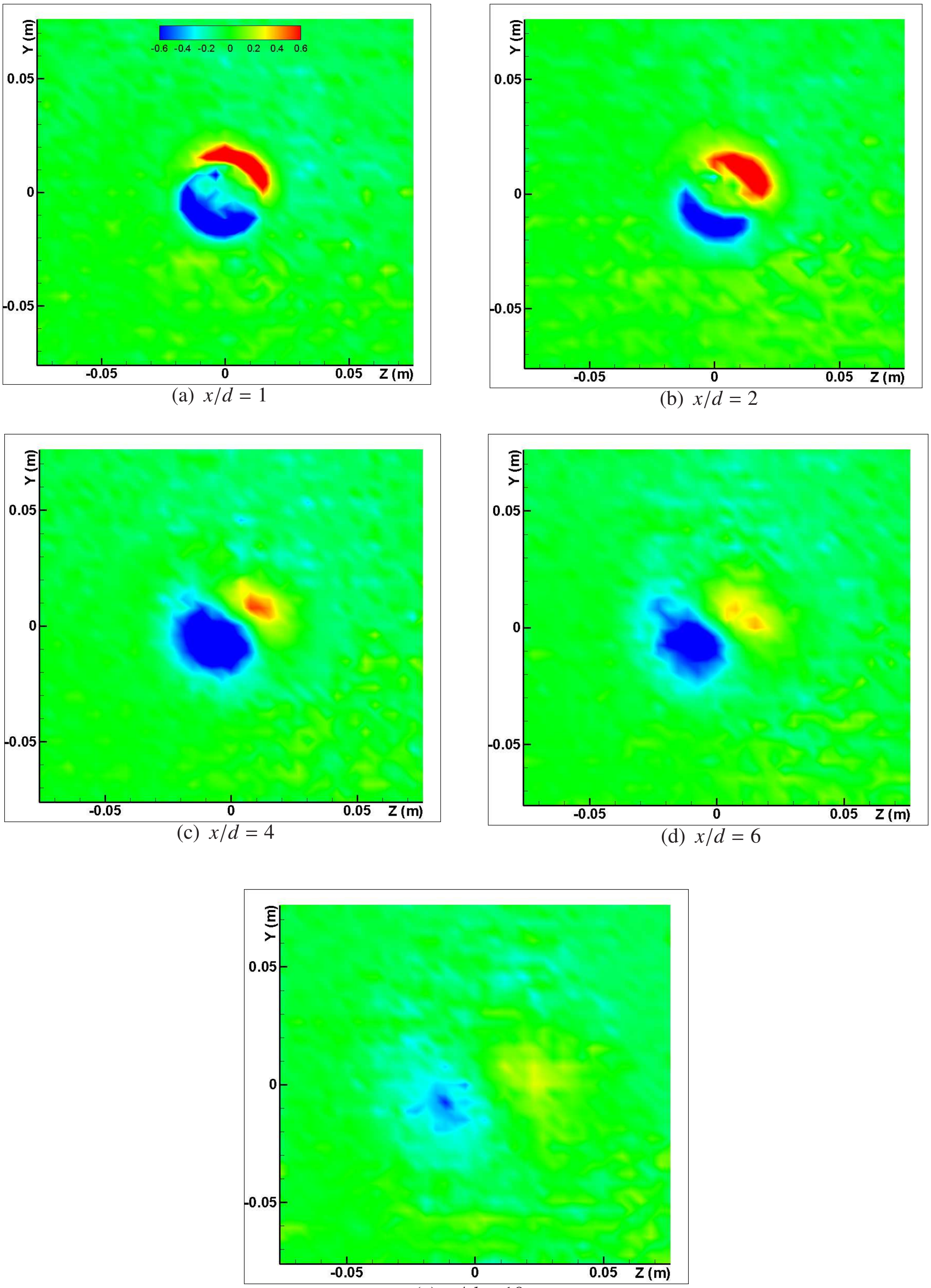

(a) $x/d = 1$

(b) $x/d = 2$

(c) $x/d = 4$

(d) $x/d = 6$

(e) $x/d = 10$

Figure 4.14: $\overline{W}$ field at various data acquisition stations (x/d = 1, 2, 4, 6 and 10) for round jet.

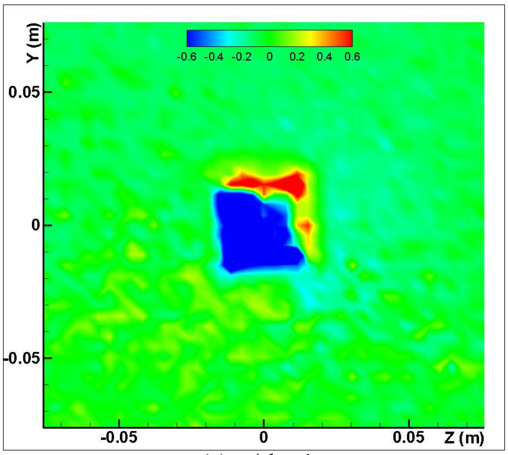

(a) x/d = 1

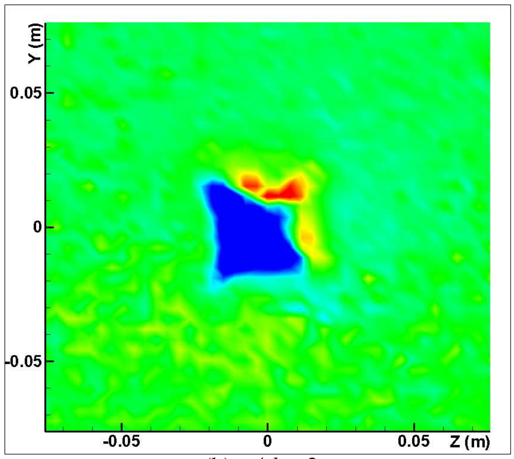

(b) x/d = 2

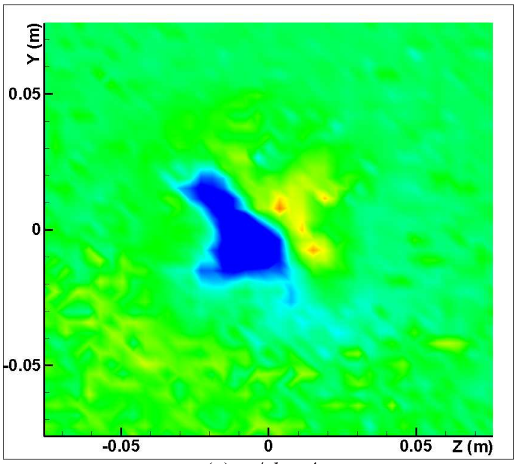

(c) x/d = 4

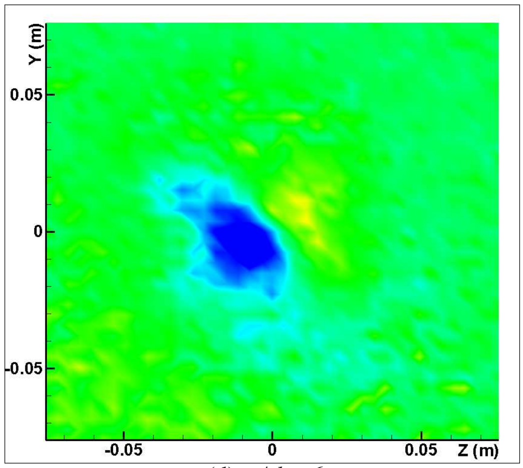

(d) x/d = 6

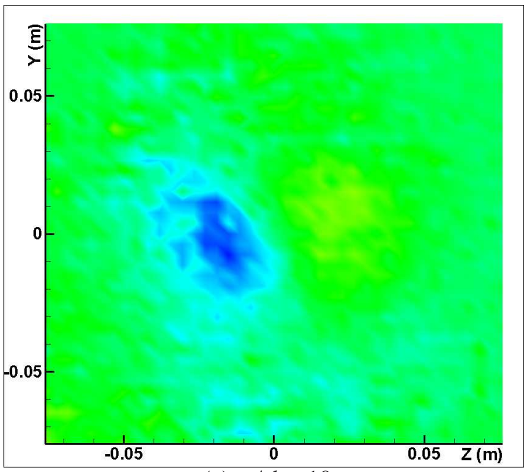

(e) x/d = 10

Figure 4.15: $\overline{W}$ field at various data acquisition stations (x/d = 1, 2, 4, 6 and 10) for square jet.

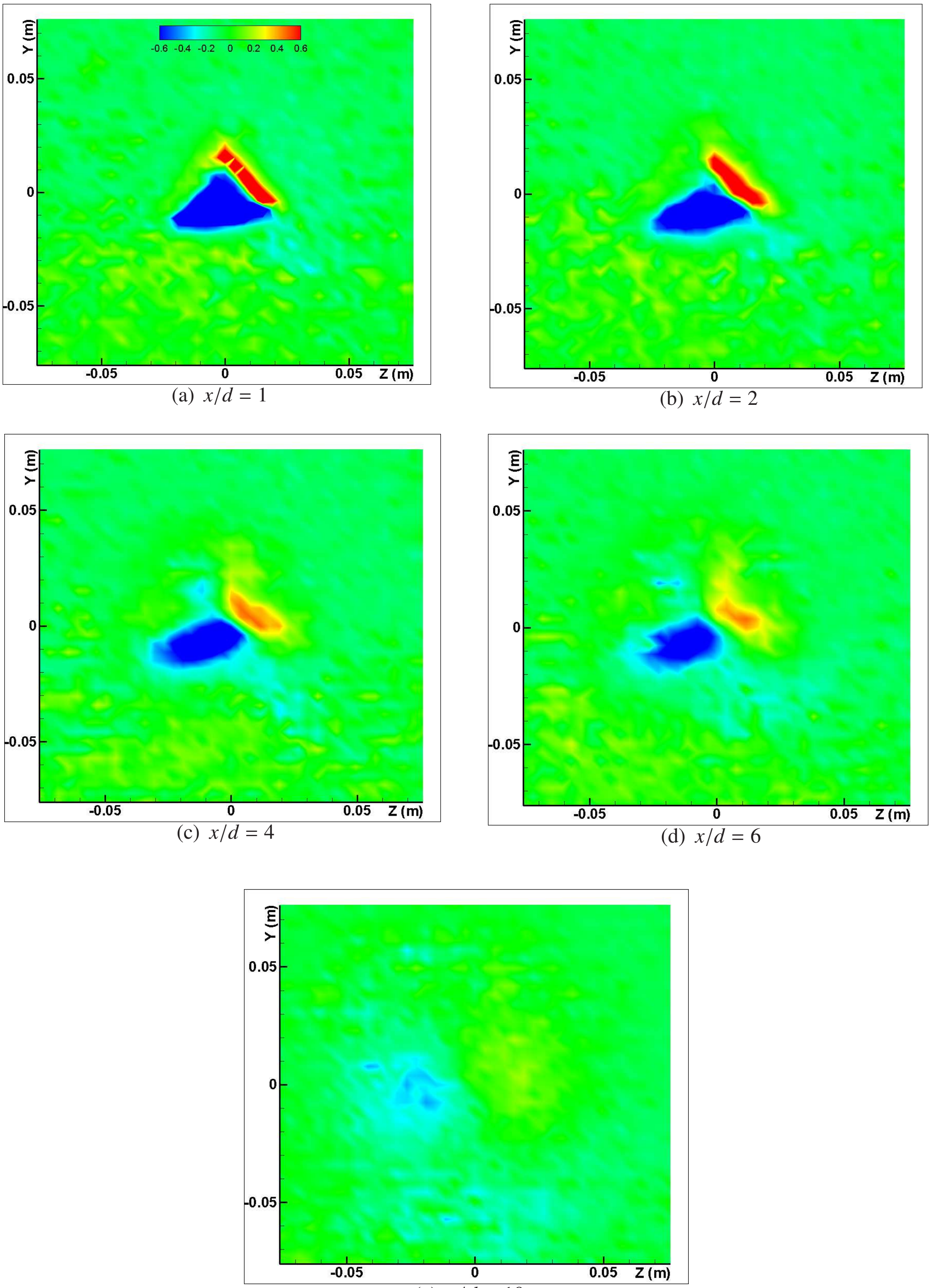

(a) $x/d = 1$

(b) $x/d = 2$

(c) $x/d = 4$

(d) $x/d = 6$

(e) $x/d = 10$

Figure 4.16: $\overline{W}$ field at various data acquisition stations (x/d = 1, 2, 4, 6 and 10) for triangular jet.

4.2.3 Reynolds Shear Stresses

The off-diagonal terms of the Reynolds stress tensor shown in Equation 4.1 are called Reynolds shear stresses whereas the diagonal terms called the Reynolds normal stresses.

$$[\overline{u_i u_j}] = \begin{bmatrix} \overline{u}^2 & \overline{uv} & \overline{uw} \\ \overline{uv} & \overline{v}^2 & \overline{vw} \\ \overline{uw} & \overline{vw} & \overline{w}^2 \end{bmatrix} \tag{4.1}$$

Recalling the mean kinetic energy balance equation 2.24 and the loss to turbulent term $\overline{u_i u_j}\frac{\partial \overline{U_i}}{\partial x_j}$ it can be seen that the Reynolds stresses are responsible for production of turbulence. When considering the transport term in equation 2.24, the shear stresses represent the mean rate of transfer of linear momentum [8]. The $\overline{uv}$ and $\overline{uw}$ are defined as the primary shear stresses.

The main result obtained from the investigation of the Reynolds shear stresses is related with the axis-switching phenomenon. The axis-switching phenomenon which is observed at orifice jets, and influenced by the axial vorticity, is not observed in the current study as stated in Gutmark and Grinstein [7]. This non-occurrence of the phenomenon is mostly due to high shear layer thickness to the jet diameter ratio. In figures 4.17, 4.18, 4.19, 4.20, 4.21, 4.22, 4.23, 4.24, and 4.25 it is demonstrated that, round jet has the thickest shear layer when compared with square and round jets. It can also be seen that the triangular jet has the smallest ratio of shear layer thickness to the jet diameter.

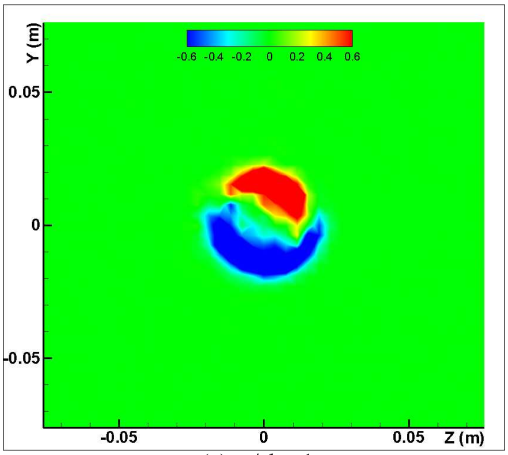

(a) $x/d = 1$

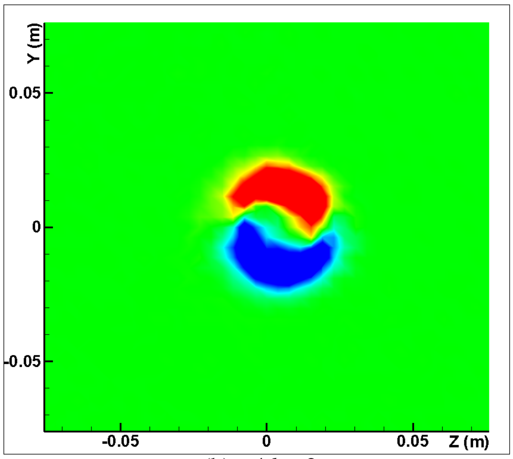

(b) $x/d = 2$

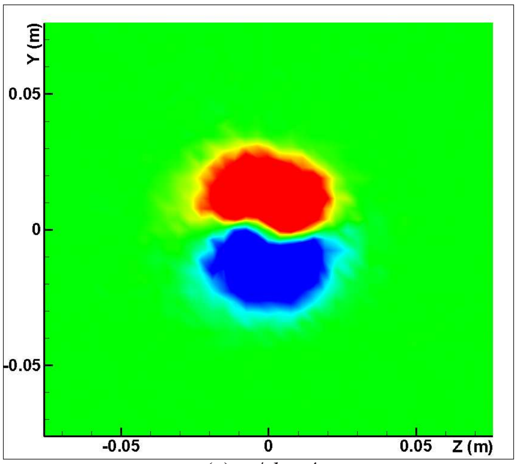

(c) $x/d = 4$

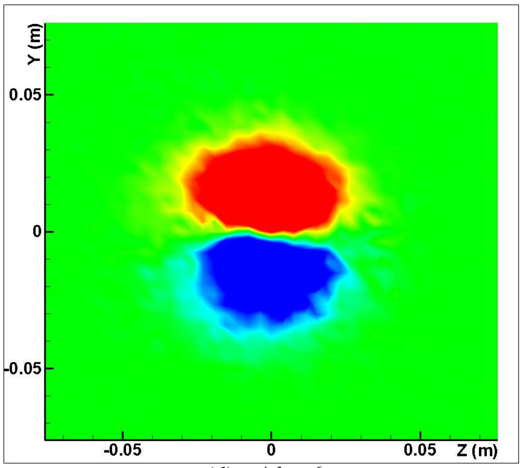

(d) $x/d = 6$

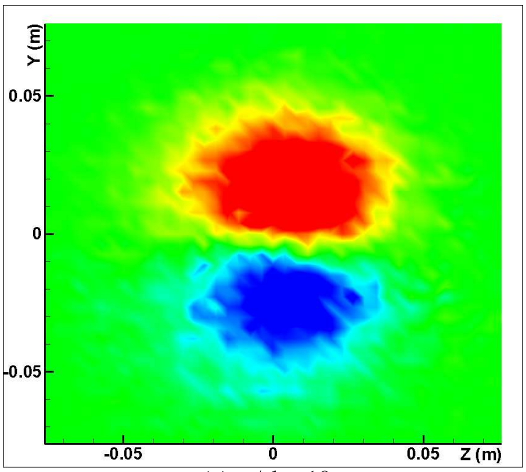

(e) $x/d = 10$

Figure 4.17: $\overline{uv}$ field at various data acquisition stations (x/d = 1, 2, 4, 6 and 10) for round jet.

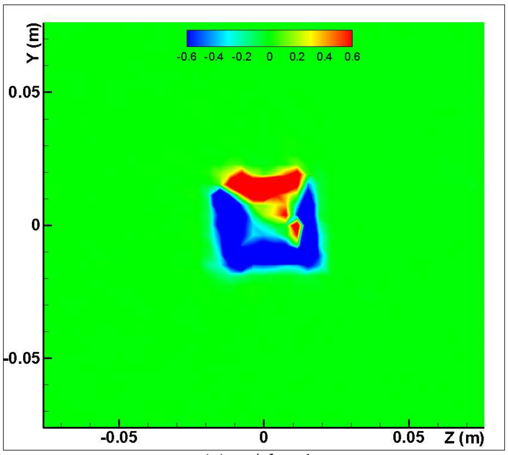

(a) $x/d = 1$

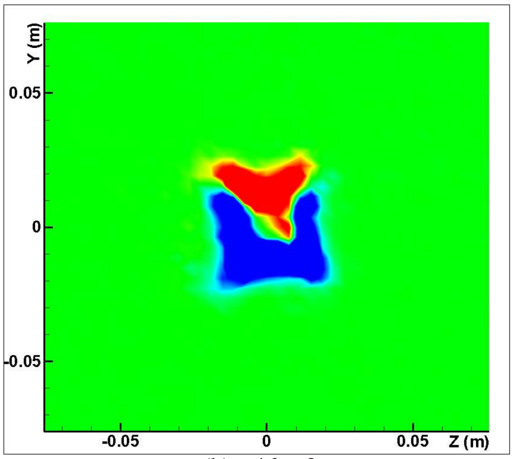

(b) $x/d = 2$

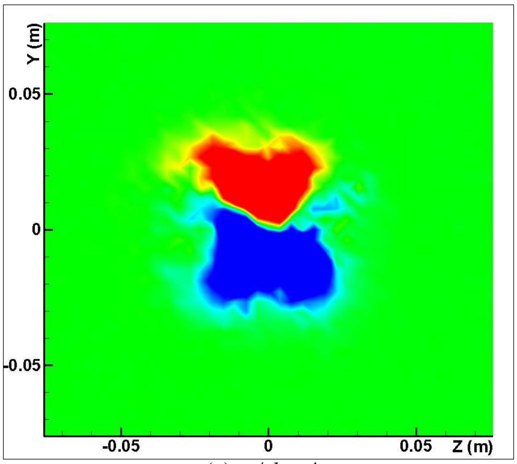

(c) $x/d = 4$

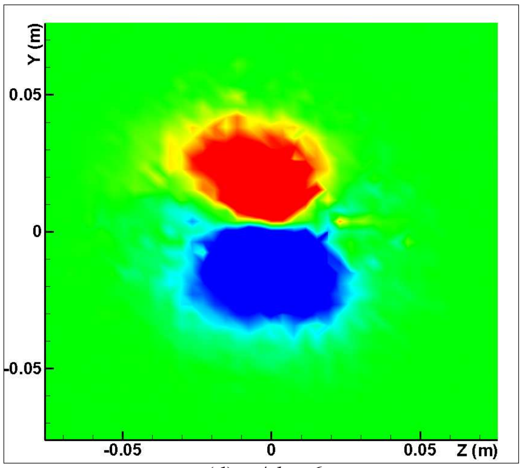

(d) $x/d = 6$

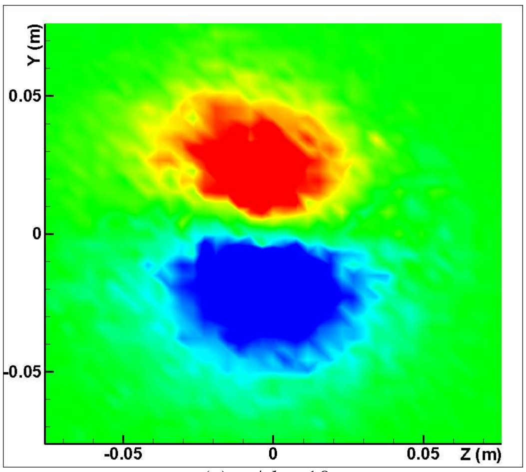

(e) $x/d = 10$

Figure 4.18: $\overline{uv}$ field at various data acquisition stations (x/d = 1, 2, 4, 6 and 10) for square jet.

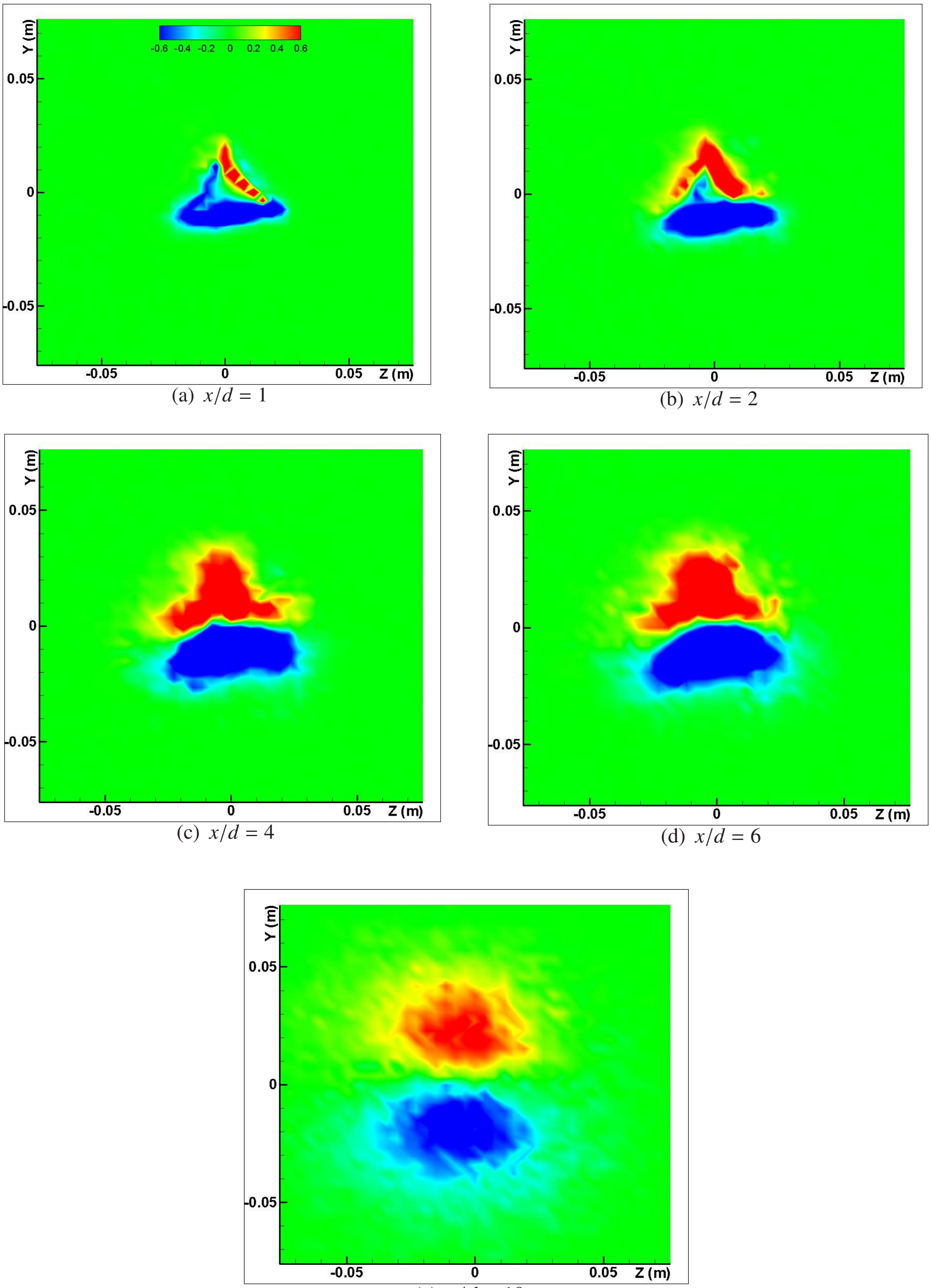

(a) $x/d = 1$

(b) $x/d = 2$

(c) $x/d = 4$

(d) $x/d = 6$

(e) $x/d = 10$

Figure 4.19: $\overline{uv}$ field at various data acquisition stations (x/d = 1, 2, 4, 6 and 10) for triangular jet.

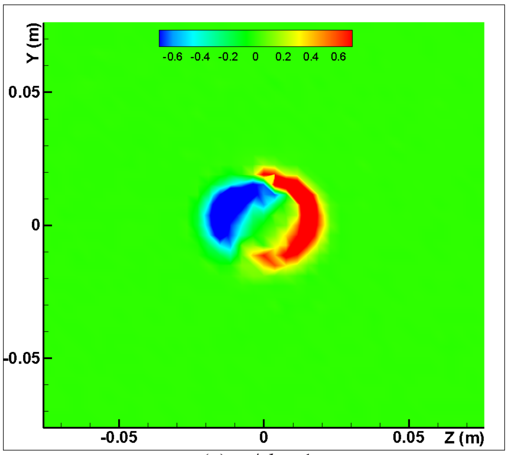

(a) $x/d = 1$

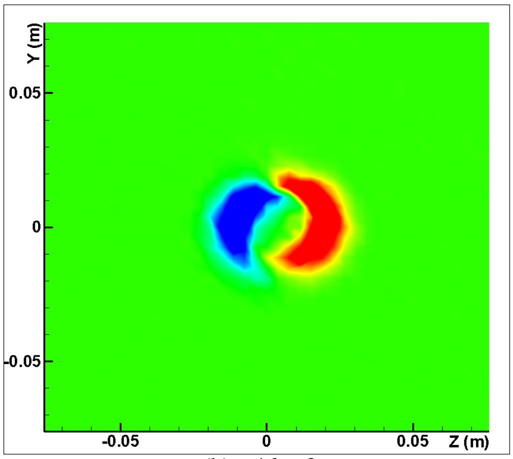

(b) $x/d = 2$

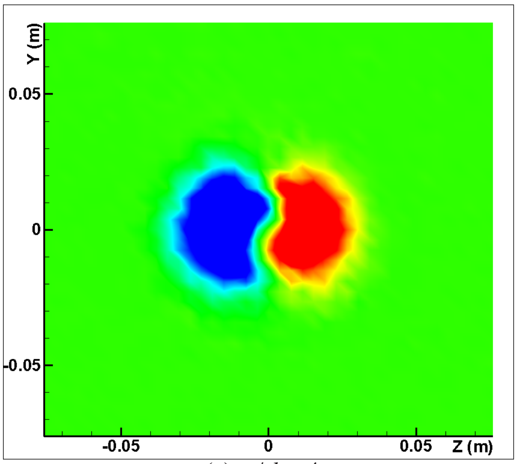

(c) $x/d = 4$

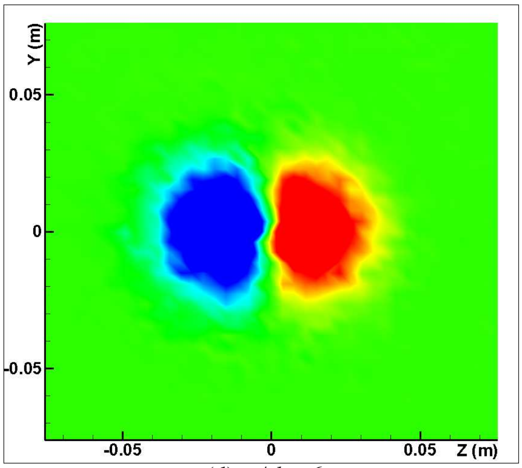

(d) $x/d = 6$

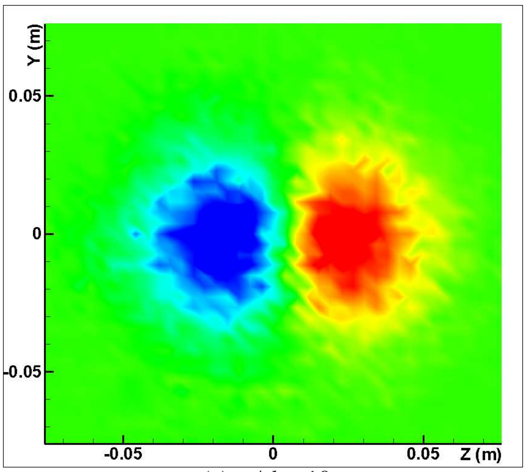

(e) $x/d = 10$

Figure 4.20: $\overline{uw}$ field at various data acquisition stations (x/d = 1, 2, 4, 6 and 10) for round jet.

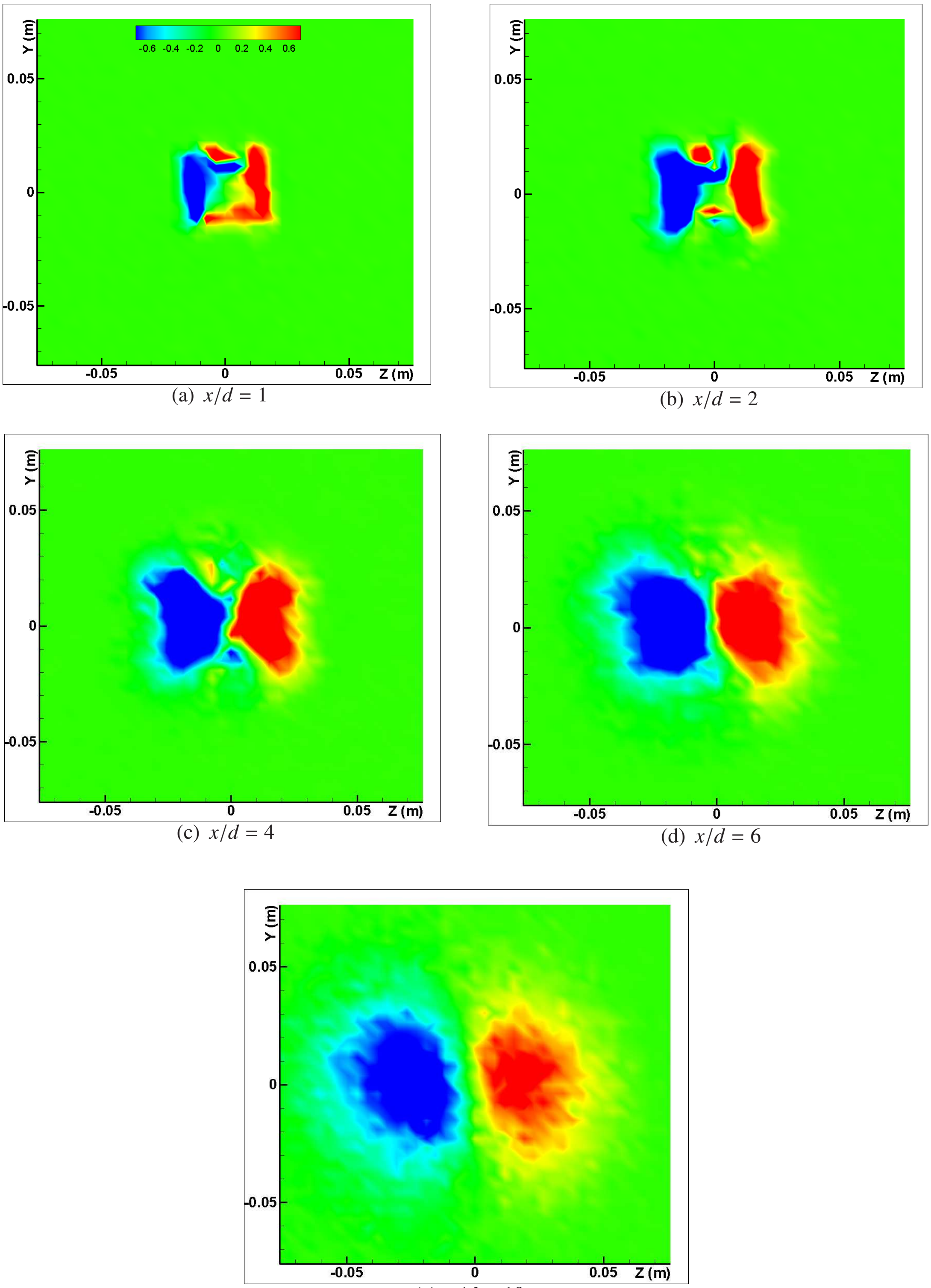

(a) $x/d = 1$

(b) $x/d = 2$

(c) $x/d = 4$

(d) $x/d = 6$

(e) $x/d = 10$

Figure 4.21: $\overline{uw}$ field at various data acquisition stations (x/d = 1, 2, 4, 6 and 10) for square jet.

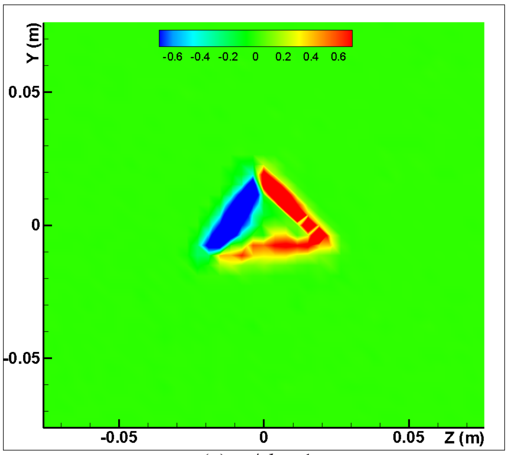

(a) $x/d = 1$

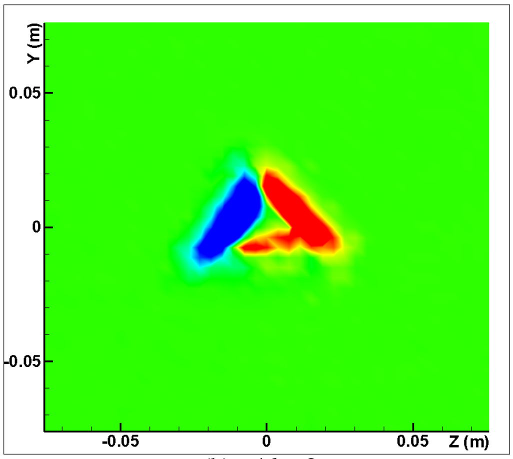

(b) $x/d = 2$

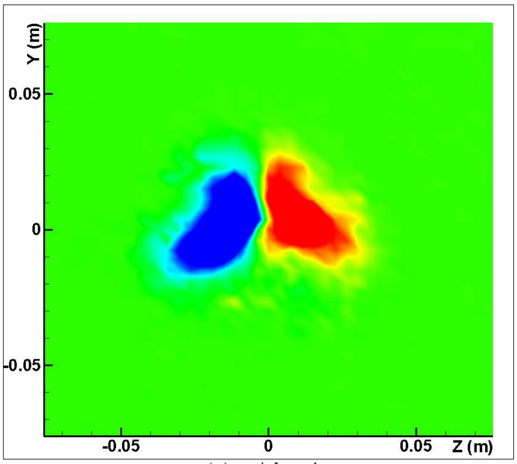

(c) $x/d = 4$

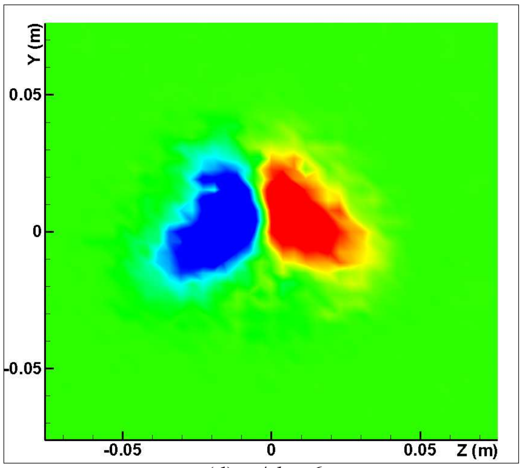

(d) $x/d = 6$

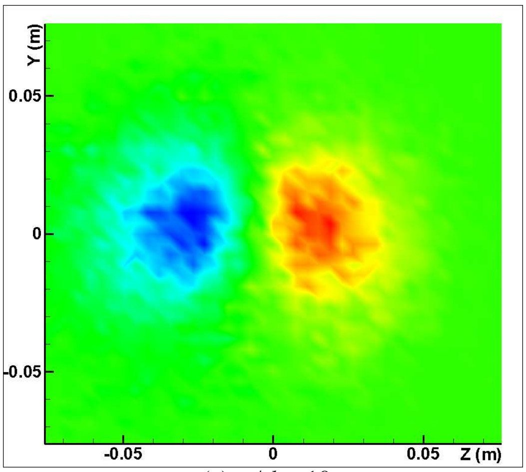

(e) $x/d = 10$

Figure 4.22: $\overline{uw}$ field at various data acquisition stations (x/d = 1, 2, 4, 6 and 10) for triangular jet.

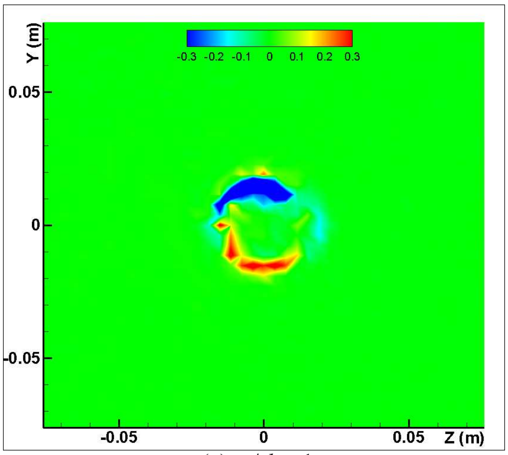

(a) x/d = 1

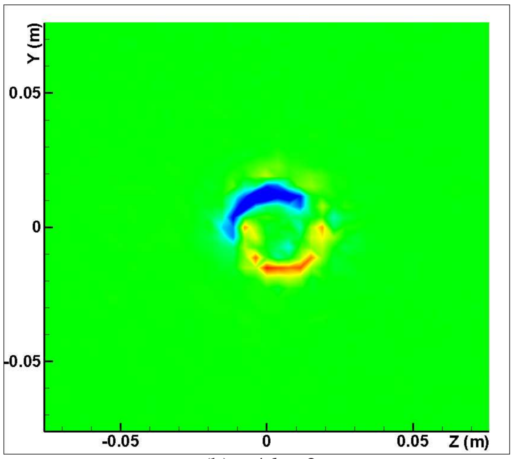

(b) x/d = 2

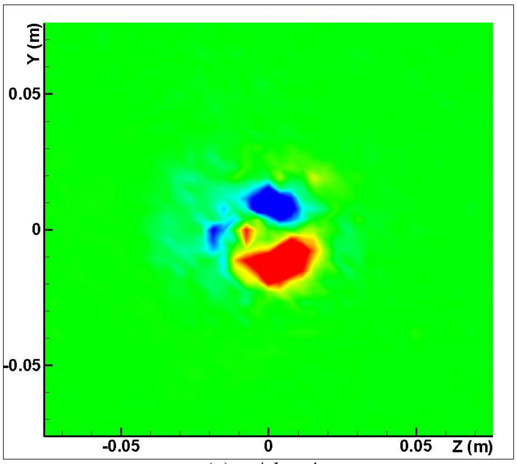

(c) x/d = 4

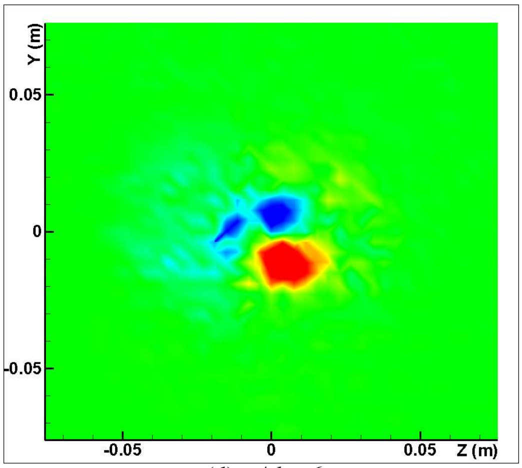

(d) x/d = 6

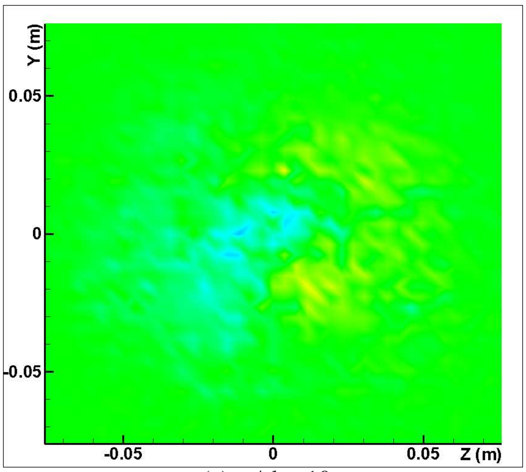

(e) x/d = 10

Figure 4.23: $\overline{vw}$ field at various data acquisition stations (x/d = 1, 2, 4, 6 and 10) for round jet.

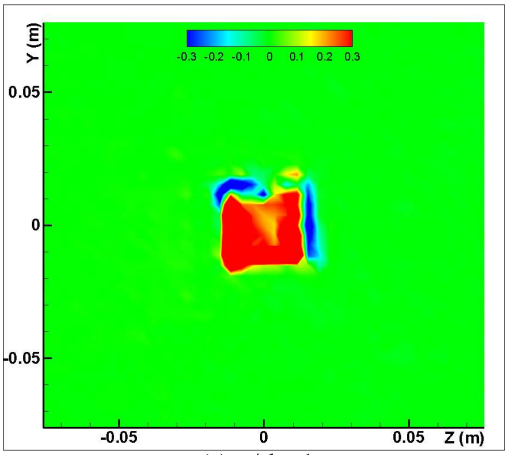

(a) $x/d = 1$

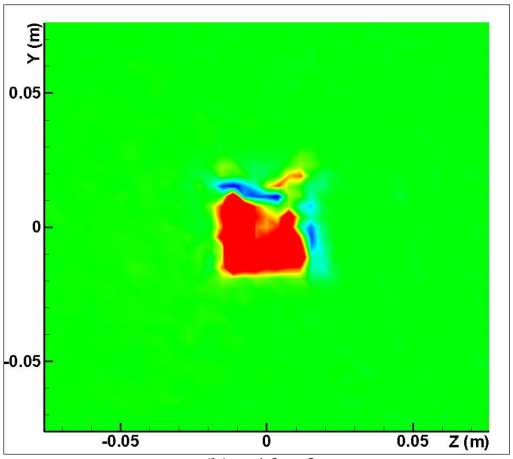

(b) $x/d = 2$

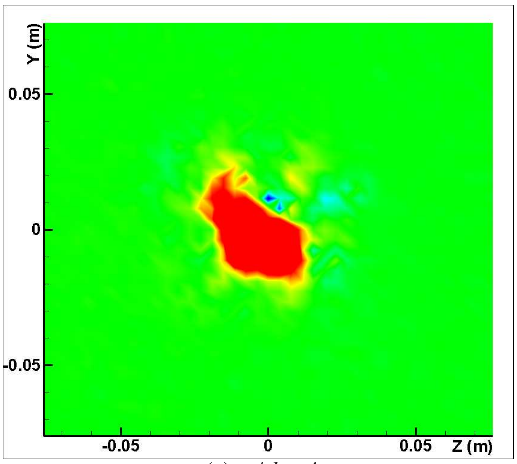

(c) $x/d = 4$

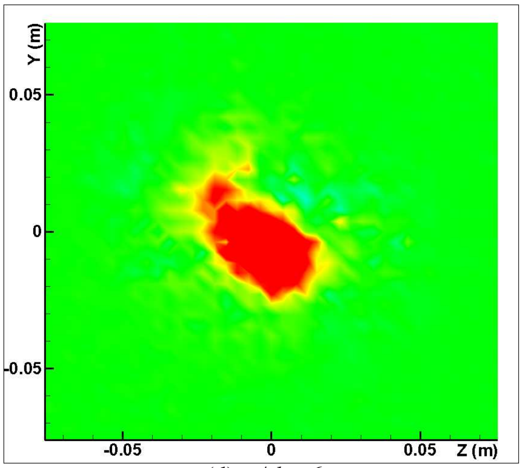

(d) $x/d = 6$

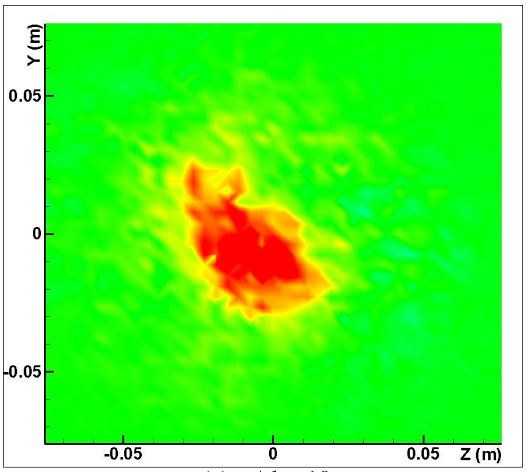

(e) $x/d = 10$

Figure 4.24: $\overline{vw}$ field at various data acquisition stations (x/d = 1, 2, 4, 6 and 10) for square jet.

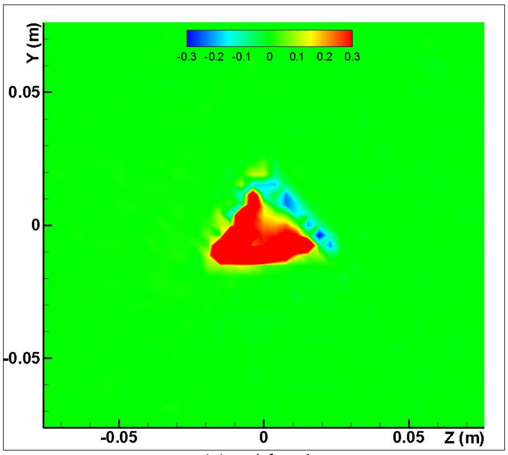

(a) $x/d = 1$

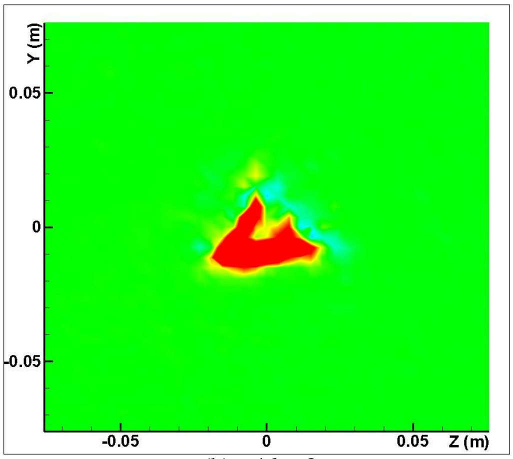

(b) $x/d = 2$

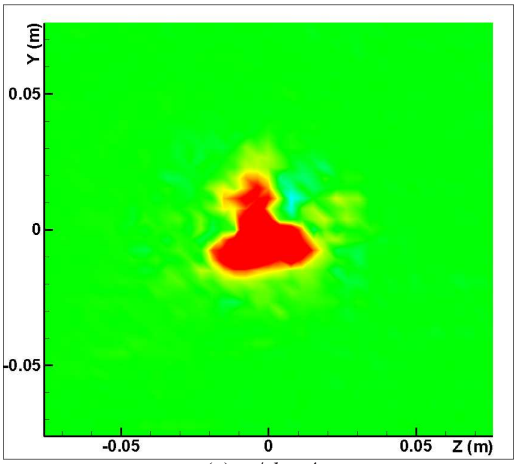

(c) $x/d = 4$

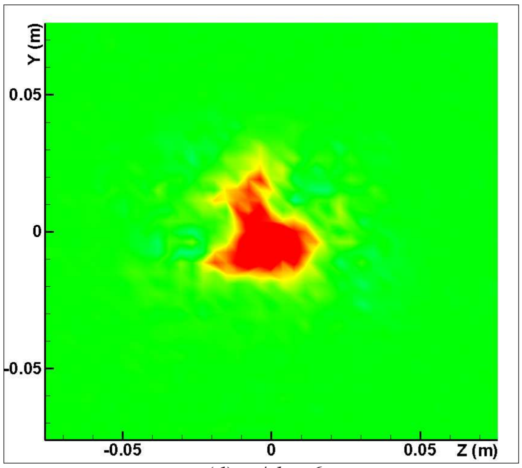

(d) $x/d = 6$

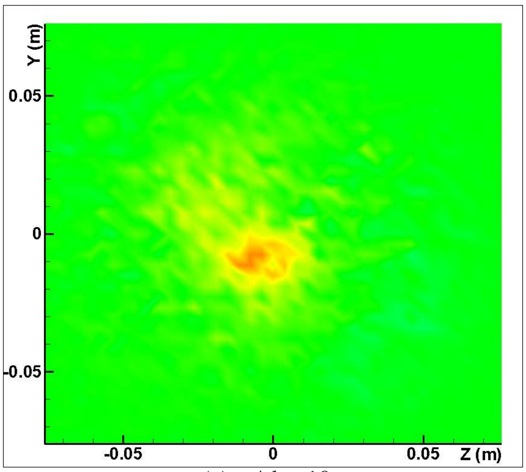

(e) $x/d = 10$

Figure 4.25: $\overline{vw}$ field at various data acquisition stations (x/d = 1, 2, 4, 6 and 10) for triangular jet.

4.2.4 Streamwise Vorticity

It is suggested by Crow and Champagne [22] that streamwise vorticity dominates the shear layer growth and entrainment at moderately high Re. It is also suggested by Liepmann and Gharib [23] that it has the most effect on mass entrainment rate after a short distance from the jet exit. The mean streamwise vorticity is described in chapter 2 as

$$\omega_x = \frac{\partial \overline{W}}{\partial y} - \frac{\partial \overline{V}}{\partial z} \tag{4.2}$$

The vorticity map is obtained by applying differencing methods to the equation 4.2. The positive and negative values of ω_x indicates the clockwise and counter-clockwise rotation of vortices consistent with the right hand rule considering in-plane $\overline{U}$.

The vorticity distribution is also known as the reason for the large-scale mixing [7]. It can be clearly inferred from the figures 4.26, 4.27, and 4.28 that, the higher values of the axial vorticity fields of square and triangular jet conducts better large-scale mixing than the round jet. Although it is very hard to guess which provides a better mixing, the enduring behaviour of the triangular jet's vorticity field up to $x/d = 6$ wipes out all the doubts that the triangular jet is a better large-scale mixer than square jet.

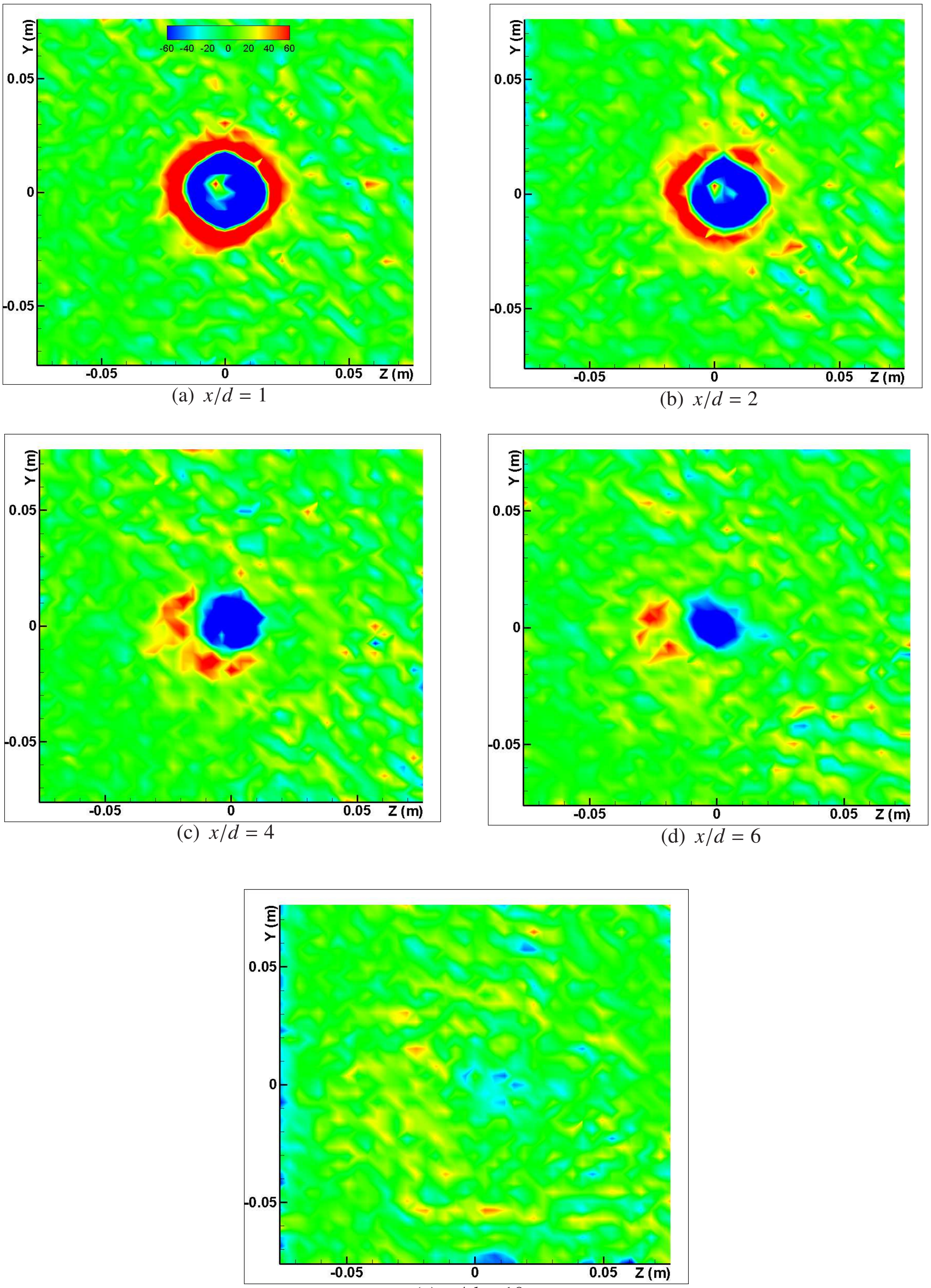

(a) $x/d = 1$

(b) $x/d = 2$

(c) $x/d = 4$

(d) $x/d = 6$

(e) $x/d = 10$

Figure 4.26: ω_x field at various data acquisition stations ((x/d = 1, 2, 4, 6 and 10) for round jet.

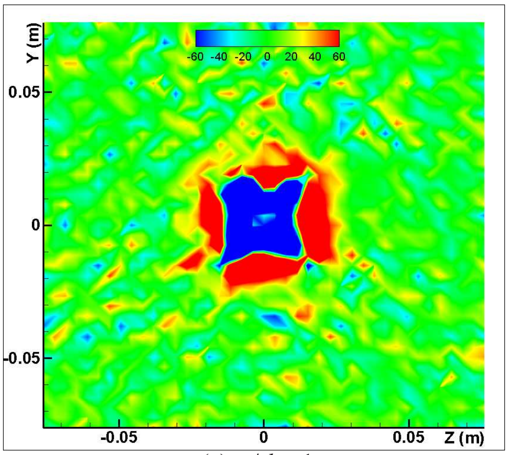

(a) $x/d = 1$

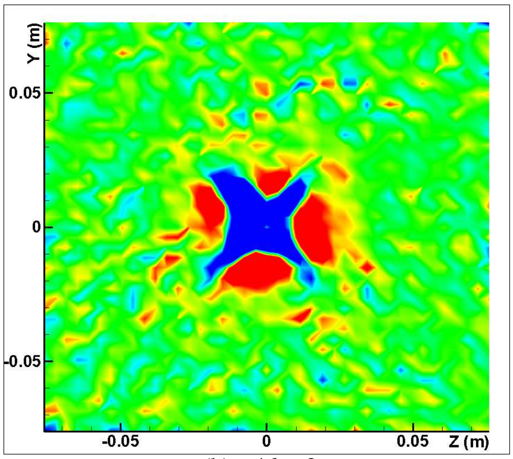

(b) $x/d = 2$

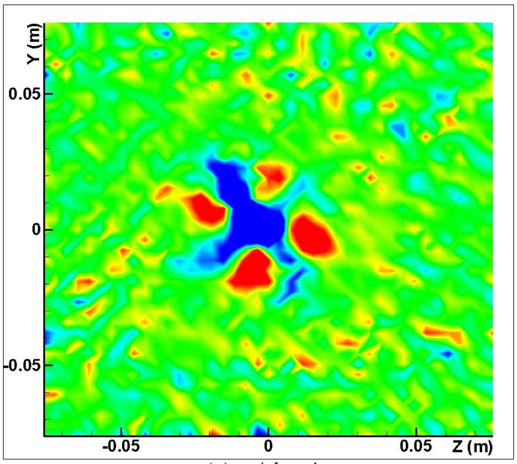

(c) $x/d = 4$

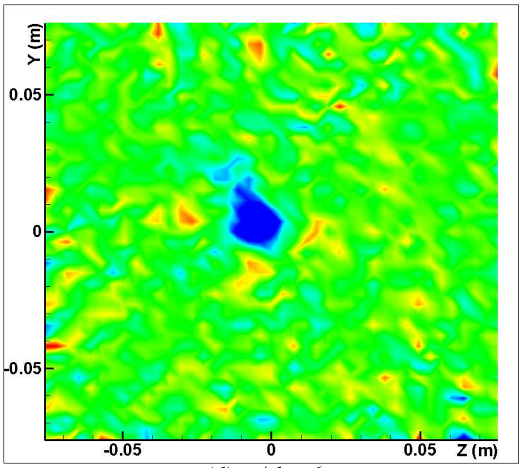

(d) $x/d = 6$

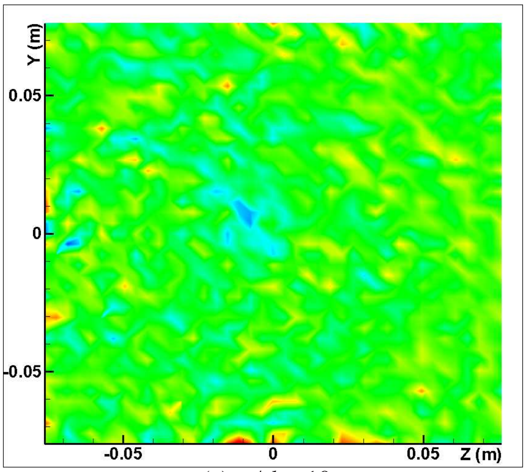

(e) $x/d = 10$

Figure 4.27: ω_x field at various data acquisition stations (x/d = 1, 2, 4, 6 and 10) for square jet.

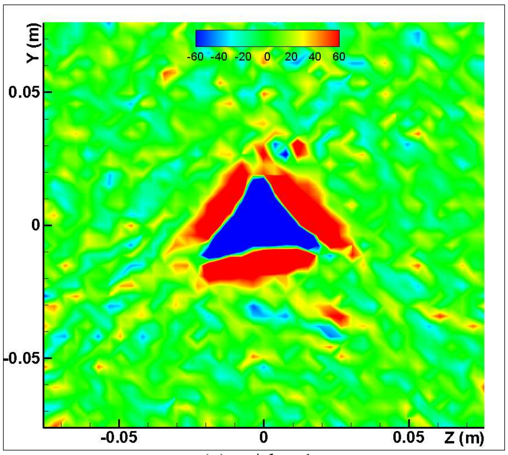

(a) x/d = 1

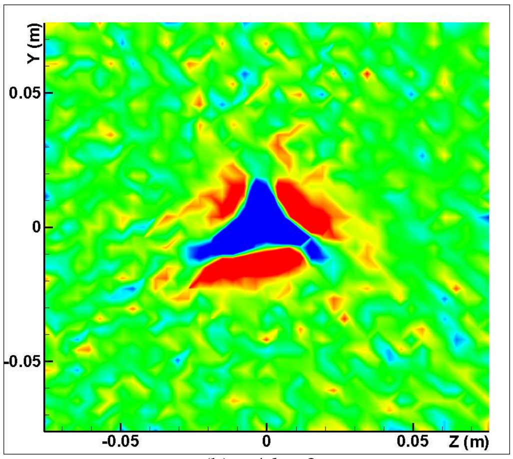

(b) x/d = 2

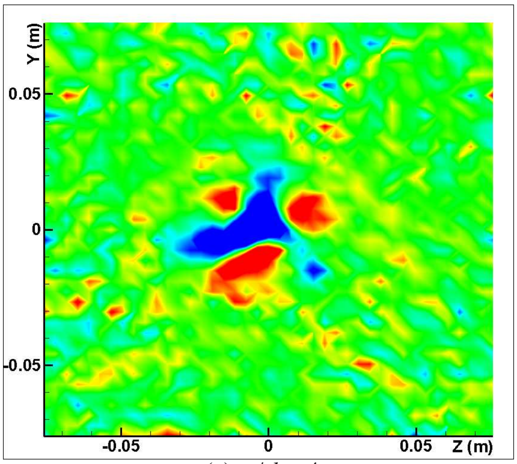

(c) x/d = 4

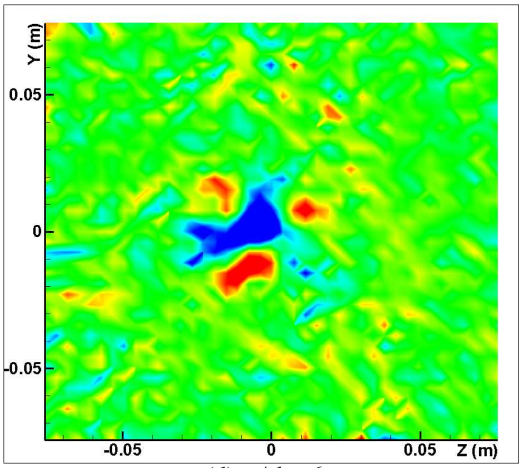

(d) x/d = 6

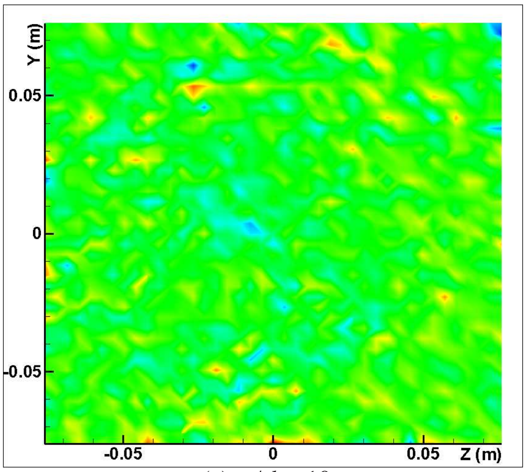

(e) x/d = 10

Figure 4.28: ω_x field at various data acquisition stations (x/d = 1, 2, 4, 6 and 10) for triangular jet.

4.2.5 Turbulent Kinetic Energy

The turbulent kinetic energy is defined as the half of the trace of the Reynolds stress tensor and defined in chapter 2 with the Equation 2.29

The turbulent kinetic energy specified in Equation 2.29 is the mean kinetic energy per unit mass in the fluctuating velocity field [19]. The turbulent kinetic energy distributions shown in figures 4.29, 4.30, and 4.31, indicate that the turbulent kinetic energy levels within the jet flow structure rise much quicker for triangular and square jets compared to the round jet. On the other hand the decay of k has the highest value for triangular jet lowest value for the round jet. The fact that the turbulent kinetic energy levels are increasing with downstream distance is consistent with the results provided by Quinn [9]. The turbulent kinetic energy distributions are also demonstrated in Section 4.3.

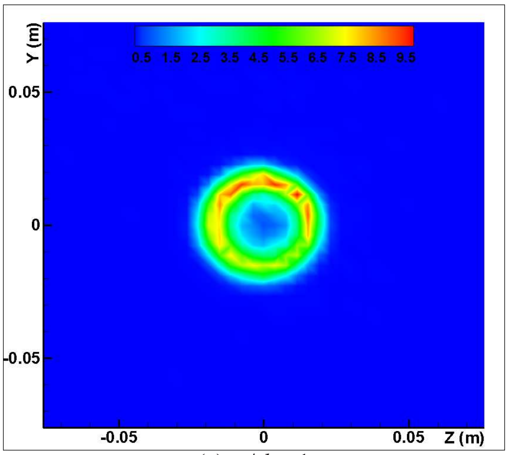

(a) $x/d = 1$

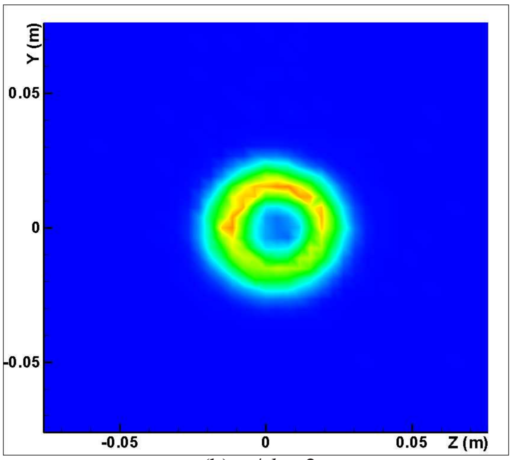

(b) $x/d = 2$

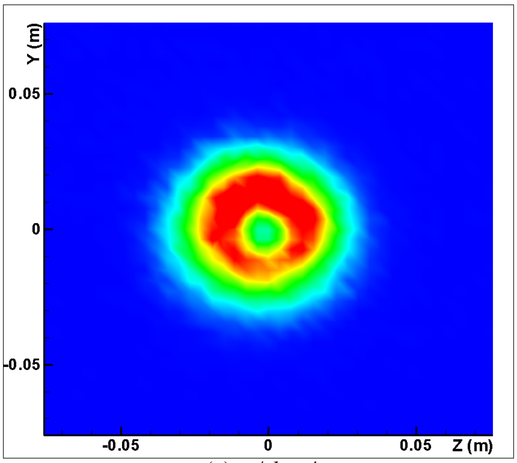

(c) $x/d = 4$

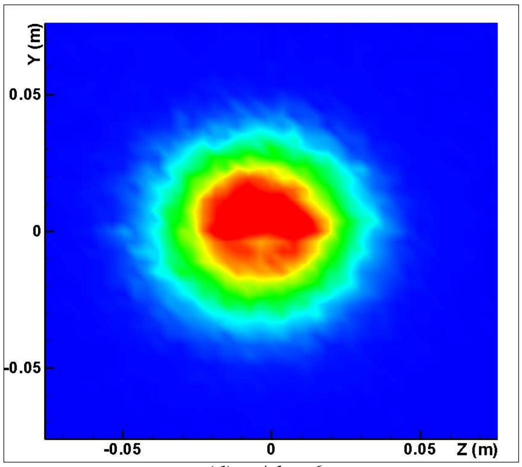

(d) $x/d = 6$

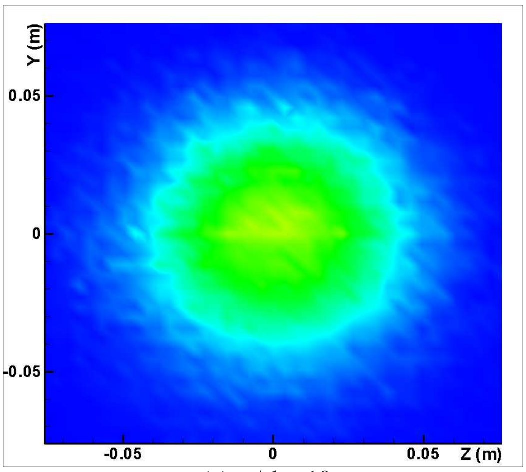

(e) $x/d = 10$

Figure 4.29: k field at various data acquisition stations ($x/d = 1, 2, 4, 6$ and 10) for round jet.

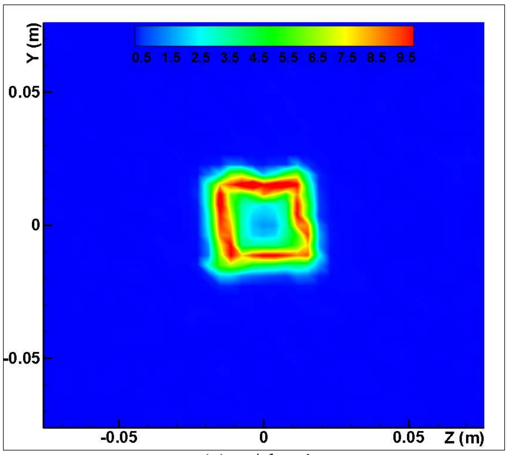

(a) $x/d = 1$

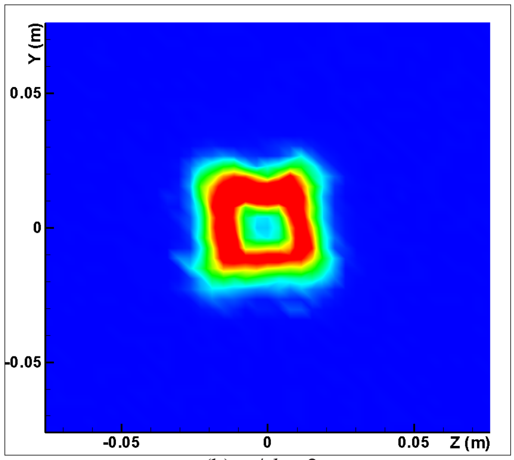

(b) $x/d = 2$

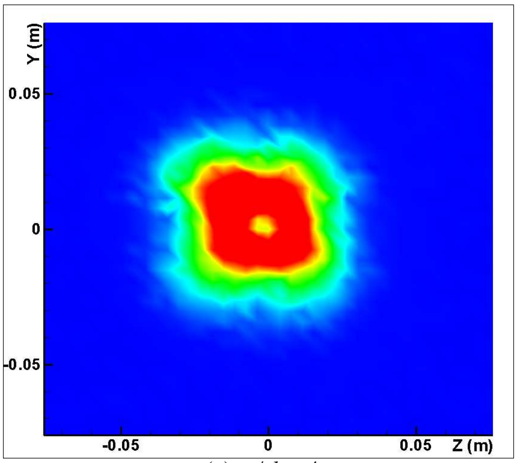

(c) $x/d = 4$

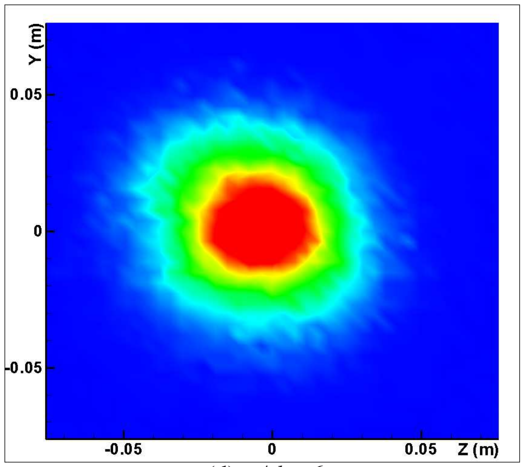

(d) $x/d = 6$

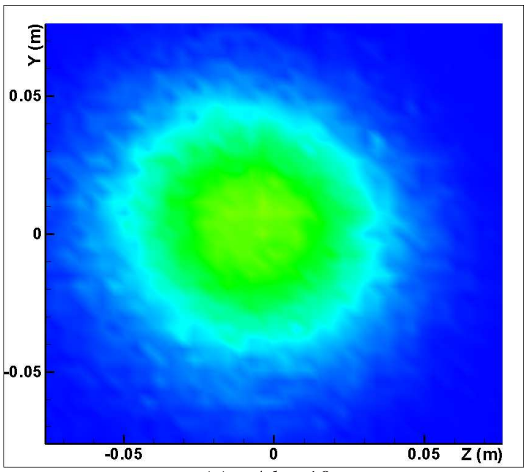

(e) $x/d = 10$

Figure 4.30: k field at various data acquisition stations (x/d = 1, 2, 4, 6 and 10) for square jet.

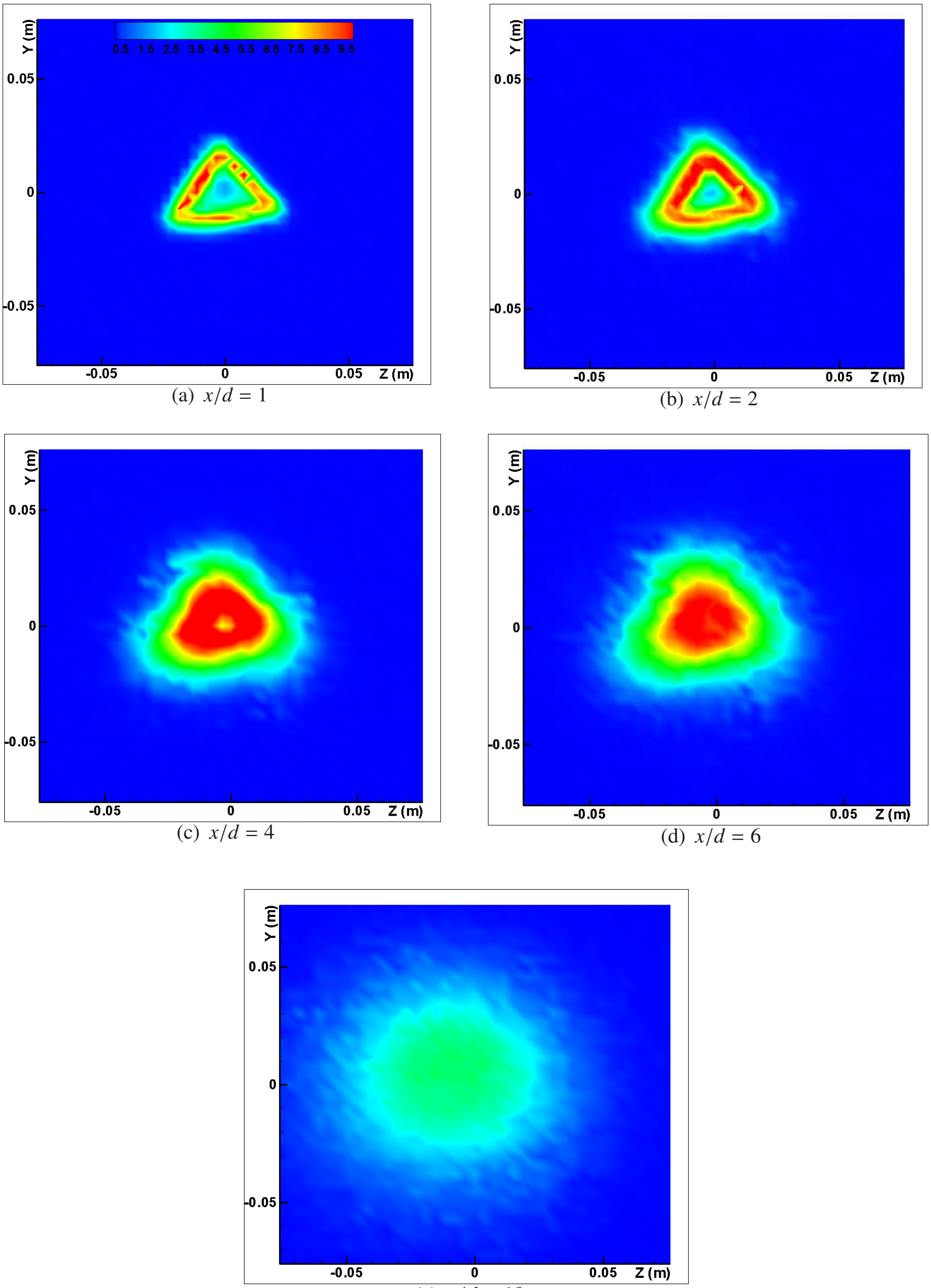

(a) $x/d = 1$

(b) $x/d = 2$

(c) $x/d = 4$

(d) $x/d = 6$

(e) $x/d = 10$

Figure 4.31: k field at various data acquisition stations ($x/d = 1, 2, 4, 6$ and 10) for triangular jet.

4.3 Longitudinal Measurements

4.3.1 Mean Axial Velocity $\overline{U}$

In order to better comprehend and visualize the velocity decay and contraction of potential core, longitudinal measurements are conducted at the center plane of each type of jet flow. Gutmark and Grinstein [7] stated that the higher mixing rate results in the smaller potential core. Together with this information and referring to the Figure 4.32 in which the triangular jet has the smallest potential core, it can be said that triangular jet has the higher mixing rate.

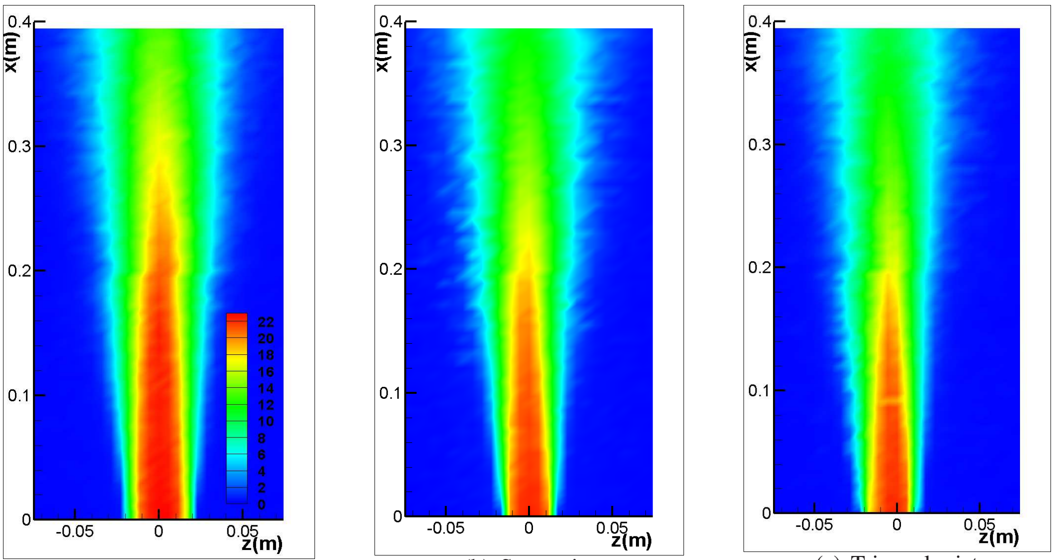

(a) Round jet (b) Square jet (c) Triangular jet

Figure 4.32: Longitudinal $\overline{U}$ field.

Figure 4.33 which shows the velocity decay up to $x/d = 10$ is also in good agreement with the results presented in Figure 3.15. Non-dimensional velocity decay profiles are also compared with Quinn's [8] results which are presented in the Figure 4.33 too. Both results are in good agreement although Quinn uses a orifice type nozzle.

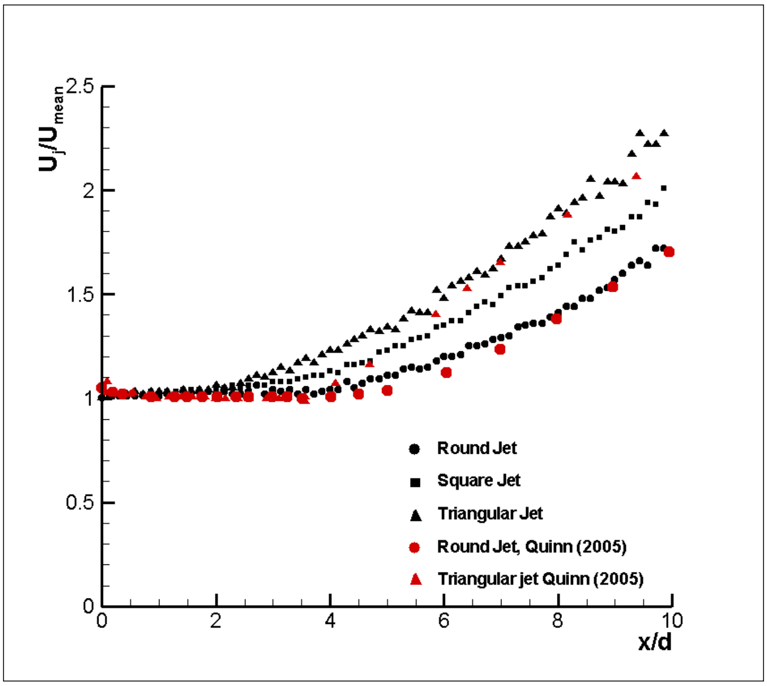

Figure 4.33: The comparison of centerline velocity variation with those reported by Quinn. [8].

4.3.2 Mean Vertical $\overline{V}$ and Horizontal Velocities $\overline{W}$

The longitudinal illustration of vertical and horizontal velocities $\overline{V}$ and $\overline{V}$ are shown in Figure 4.34 and Figure 4.35. They have similar velocity decay behaviour like axial velocity $\overline{U}$. The highest reduction in $\overline{V}$ and $\overline{W}$, is observed in triangular jet whereas the round jet velocity decay is the lowest.

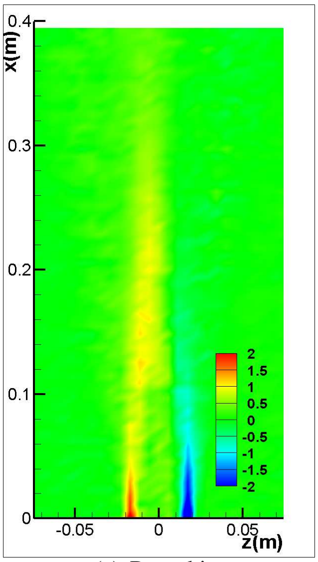

(a) Round jet

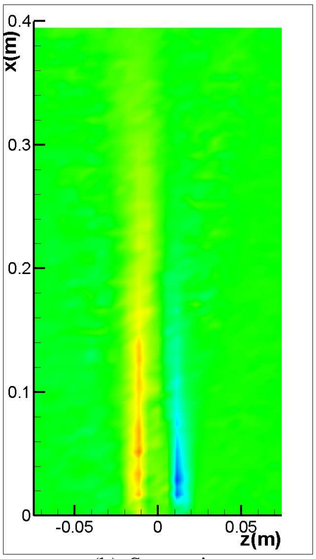

(b) Square jet

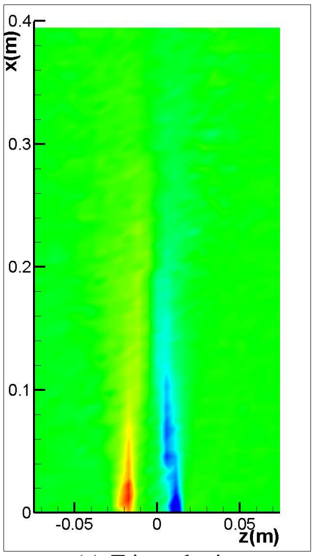

(c) Triangular jet

Figure 4.34: Longitudinal $\overline{V}$ field.

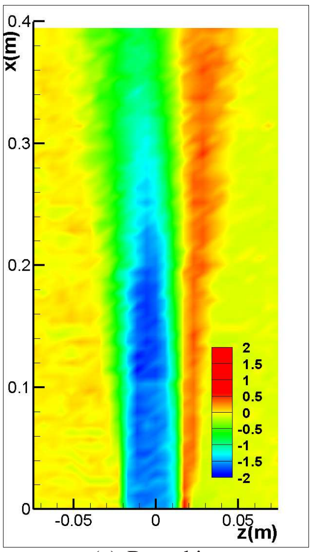

(a) Round jet

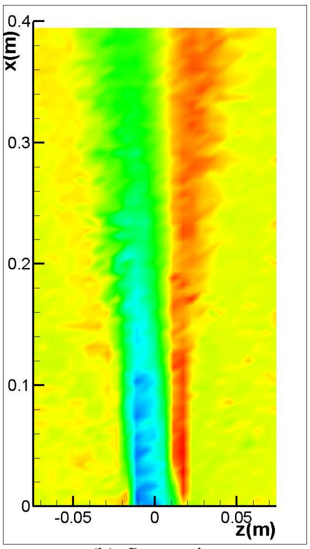

(b) Square jet

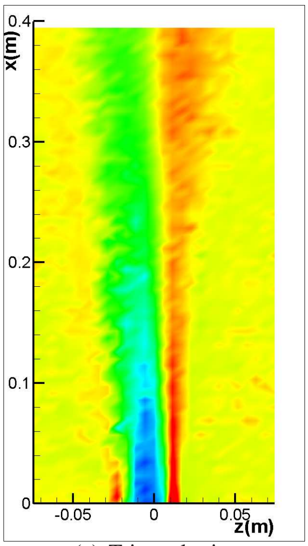

(c) Triangular jet

Figure 4.35: Longitudinal $\overline{W}$ field.

4.3.3 Reynolds Shear Stresses

Longitudinal visualization of Reynolds shear stress field gives an opportunity of better observation of shear layer thickness to the jet diameter ratio. In figures 4.36, 4.37 and 4.38 it is cleary seen that triangular jet has the smallest shear layer thickness to the jet diameter ratio as stated in Subsection 4.2.3,

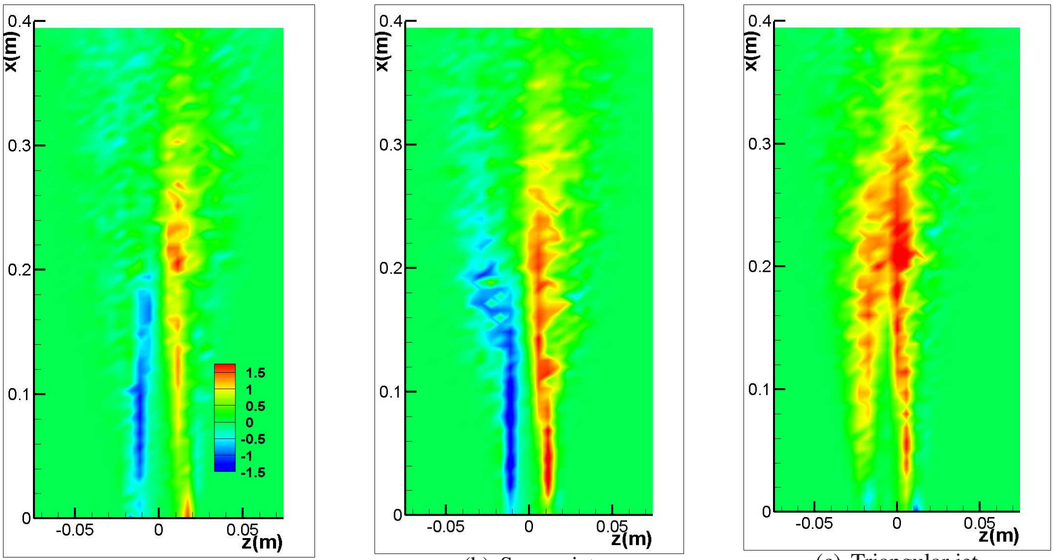

(a) Round jet (b) Square jet (c) Triangular jet

Figure 4.36: Longitudinal $\overline{uv}$ field.

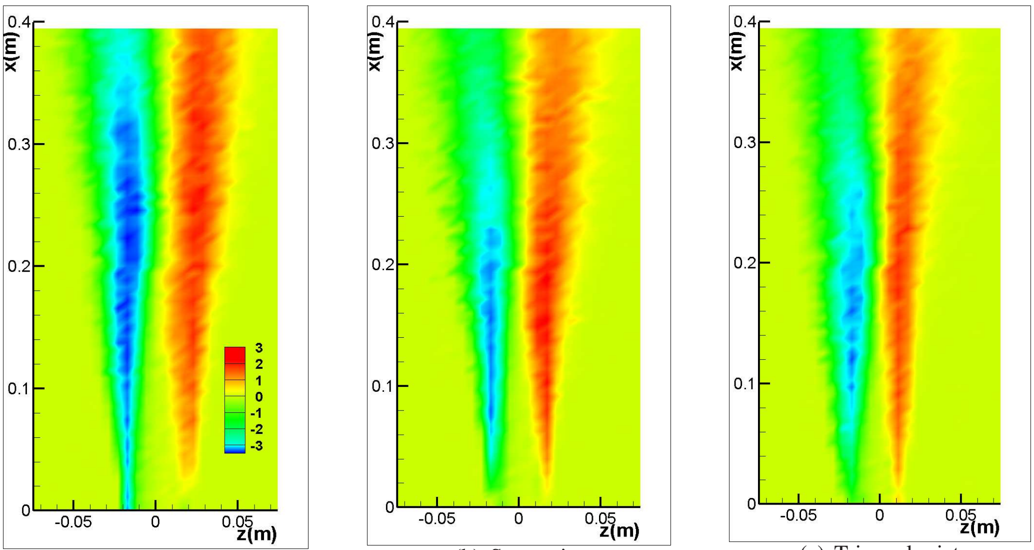

(a) Round jet (b) Square jet (c) Triangular jet

Figure 4.37: Longitudinal $\overline{uw}$ field.

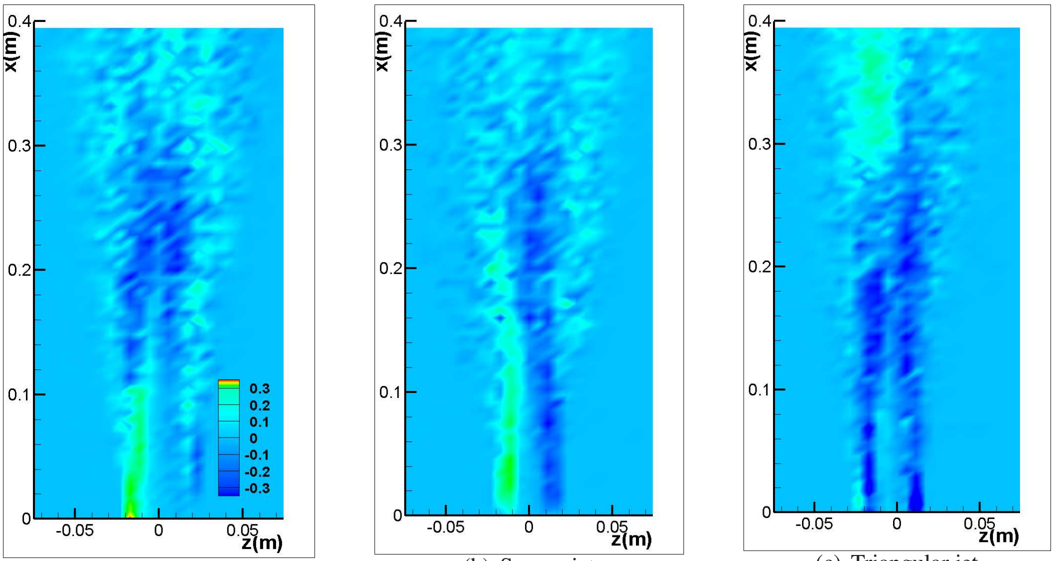

(a) Round jet (b) Square jet (c) Triangular jet

Figure 4.38: Longitudinal $\overline{vw}$ field.

4.3.4 Vertical Vorticity

In the longitudinal analysis of the flow vertical vorticity is determined by

$$\omega_y = \frac{\partial \overline{U}}{\partial z} - \frac{\partial \overline{W}}{\partial x} \tag{4.3}$$

It can be seen from the Figure 4.39 that, ω_y fields have similar distribution for round, square and triangular jets. Considering this similarity it can be said that vertical vorticity has no significant influence on mixing and mass entrainment.

4.3.5 Turbulent Kinetic Energy

The turbulent kinetic energy increases suddenly in the streamwise direction and after reaching a maximum value, it is transported to the jet centerline [8]. This phenomenon can be observed from the normalized profile of k along the centerline which is shown in Figure 4.41. In order to compare the convection and diffusion of the k Figure 4.40 should be checked.

Referring to the Figure 4.40 and Figure 4.41 it can be said that triangular jet has the maximum convection and dissipation of k. Similarly, triangular jet has the maximum normalised value

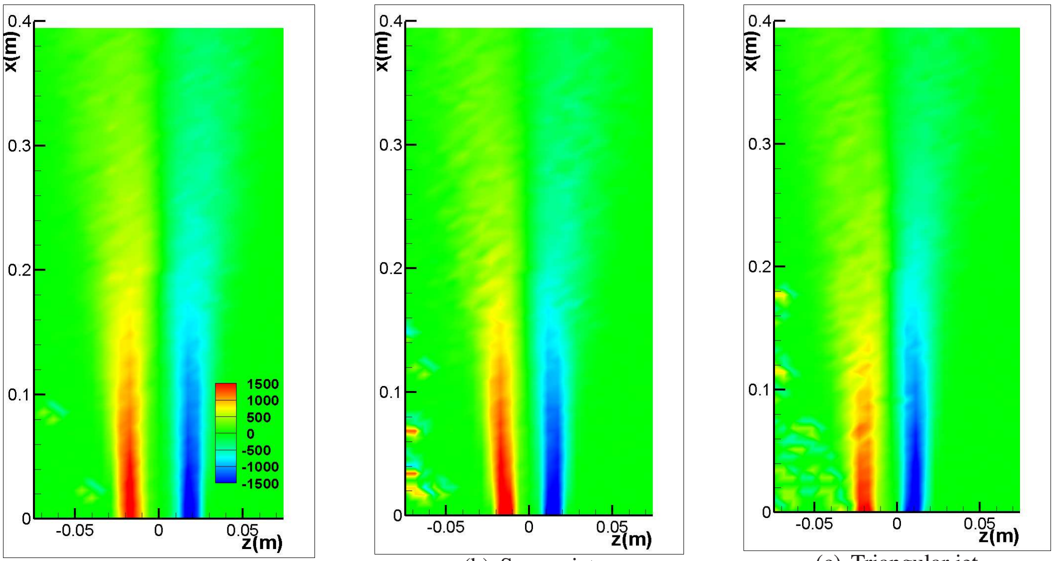

(a) Round jet (b) Square jet (c) Triangular jet

Figure 4.39: Longitudinal ω_y field.

of k across the centerline.

Moreover, overlapping regions of maximum k and shear layer, is a good illustration for turbulence production behaviour of shear layer.

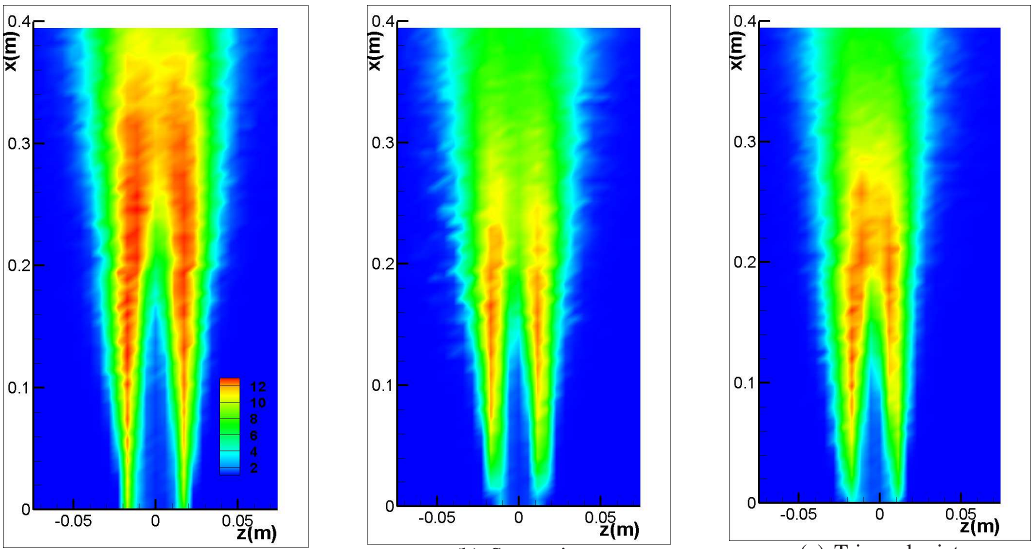

(a) Round jet (b) Square jet (c) Triangular jet

Figure 4.40: Longitudinal k field.

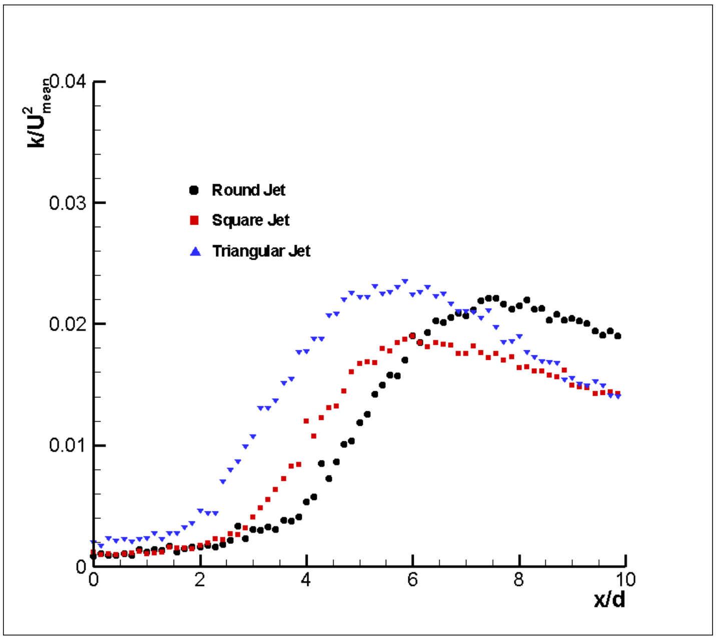

Figure 4.41: The comparison of normalized profile k in longitudinal direction.

4.4 Mass Entrainment Rate

One of the most important outcomes of this study in order to decide the most efficient geometry for highest possible level of atomization, is the comparison of mass entrainment rates.

Quinn [9] defined mass entrainment rate as

$$MassEnrainmentRate = \frac{Q - Q_0}{Q_0}, \tag{4.4}$$

where

$$Q = \int_A \rho U dA, \tag{4.5}$$

and Q_0 represent the mass flux at the jet exit. The Q and Q_0 are calculated by using numerical integration of $\overline{U}$ at each x/d station.

Regardless of the nonexistence of axis-switching, the results shown in figure 4.42 are consistent with those of Quinn [9] as the triangular jet introduces the highest mass entrainment rate when compared with round and square jet.

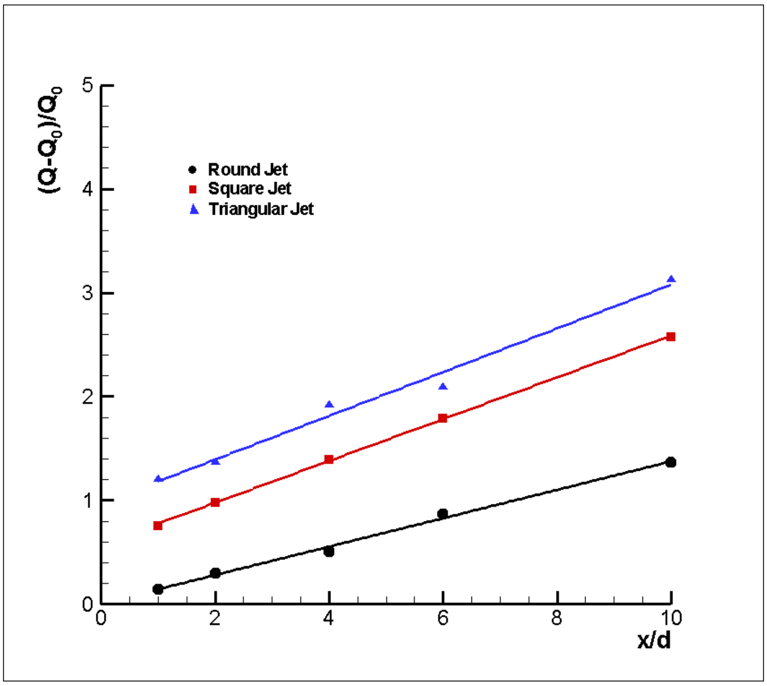

Figure 4.42: Mass entrainment rates of round, square and triangular jets.

4.5 Stress-Strain Relation

The stress-strain relation of the jet flow is also covered in this study. The eigenvalue structures and eigenvector alignment of stress and strain is investigated which deserves special attention in order to provide a basis for turbulent models and point out the geometry effects on stress-strain alignment.

In previous chapters the mean strain rate is defined as

$$\overline{S}_{ij} = \frac{1}{2}\left(\frac{\partial \overline{U_i}}{\partial x_j} + \frac{\partial \overline{U_j}}{\partial x_i}\right) \tag{4.6}$$

The first, second and the third eigenvalues of the mean strain rate tensor yields the most contracting, intermediate and most extensive modes respectively. As there is no rotation in the principal axes, the off diagonal terms of the principal strain tensor are zero.

Similarly as Pope [19] states, in the principal axes the Reynolds shear stresses are found to be zero whereas the normal stresses, that is the eigenvalues are non-negative.

The deviatoric anisotropic part of the stress tensor is defined in Pope [19] as

$$a_{ij} = \overline{u_i u_j} - \frac{2}{3}k\delta_{ij} \tag{4.7}$$

where k represents the turbulent kinetic energy and δ_{ij} represents the Kronecker's delta.

Comparing the Figures 4.43, 4.44, and 4.45 with 4.46, 4.47, and 4.48, it can be seen that contracting eigen values of S_ij matches with the first eigen value of the $\overline{u_i u_j}$ as it refers compressive stress. Similarly extensive eigen values of S_ij can be related with the third eigen value of the $\overline{u_i u_j}$ as it refers tensile stress.

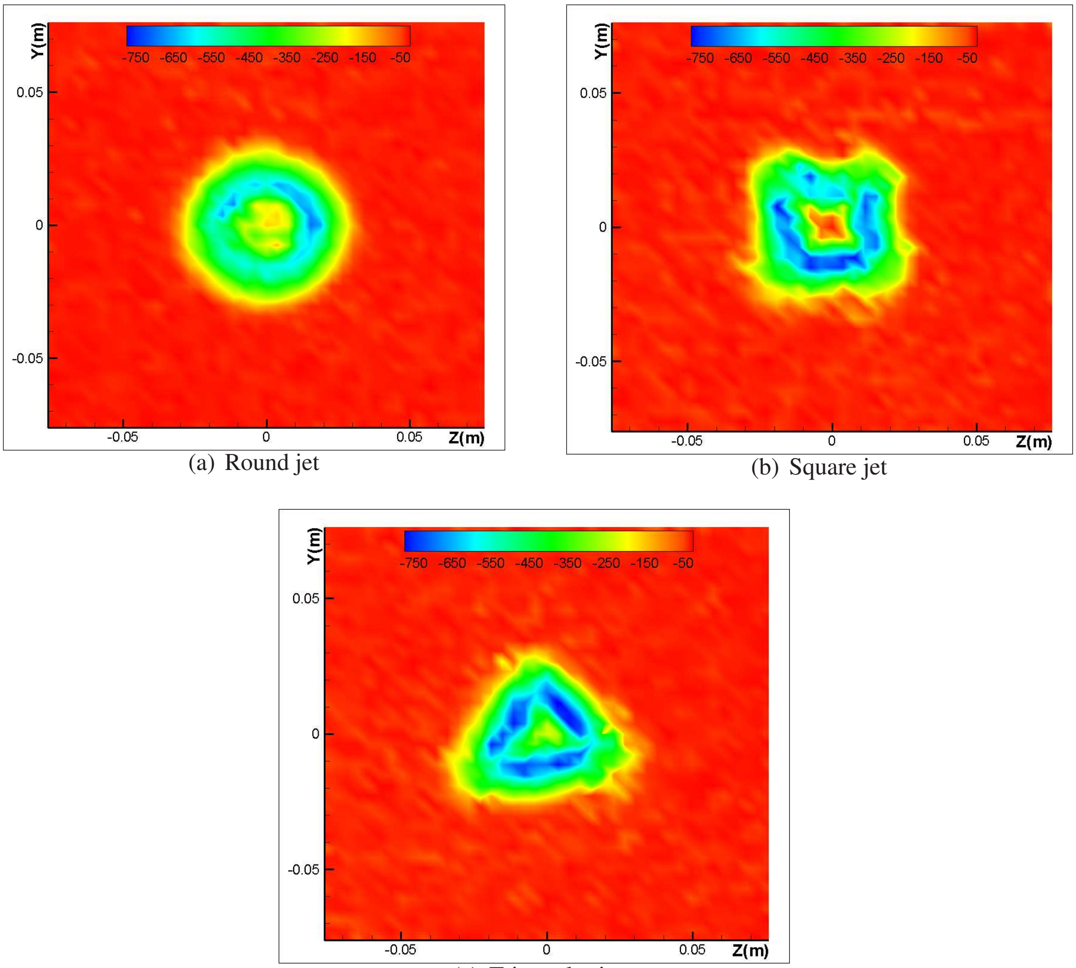

(a) Round jet

(b) Square jet

(c) Triangular jet

Figure 4.43: The contracting eigenvalues of $\overline{S_{ij}}$ at $x/d = 2$.

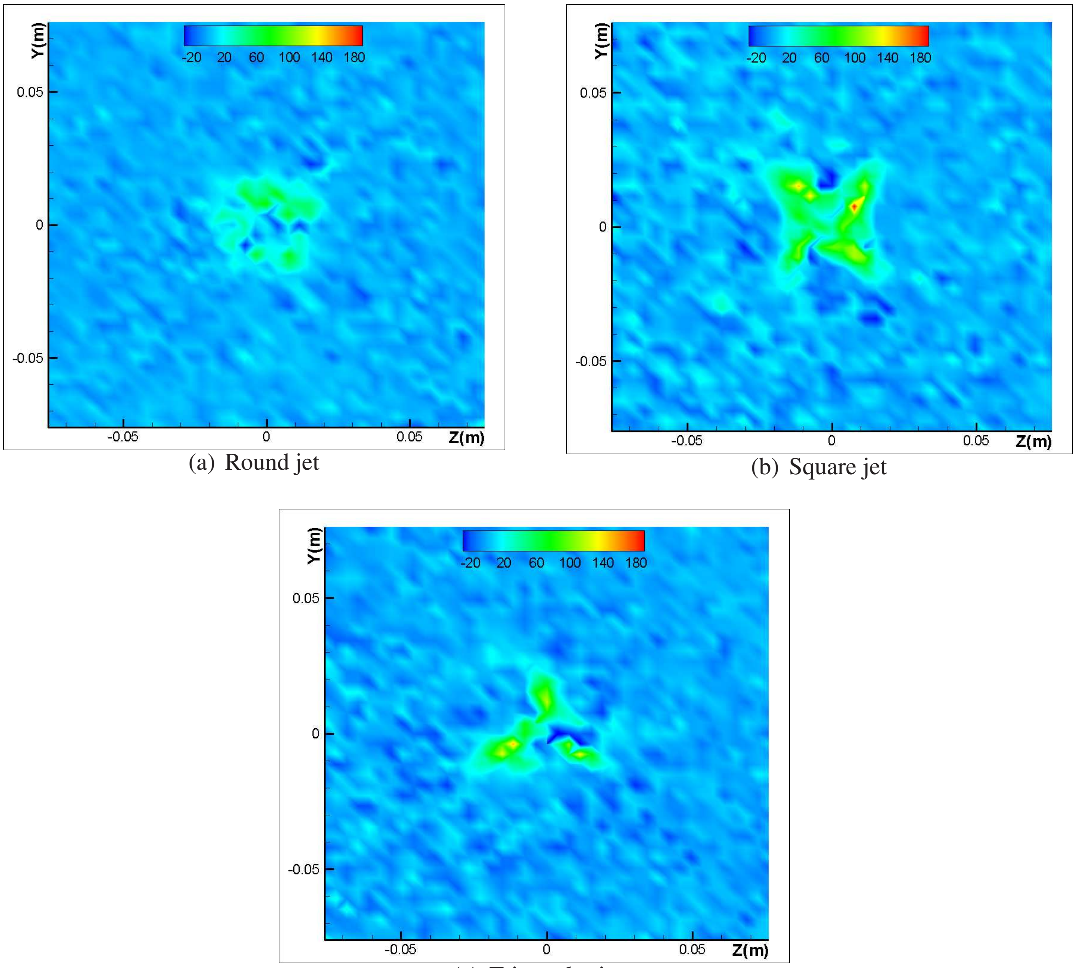

(a) Round jet

(b) Square jet

(c) Triangular jet

Figure 4.44: The intermediate eigenvalues of $\overline{S_{ij}}$ at $x/d = 2$.

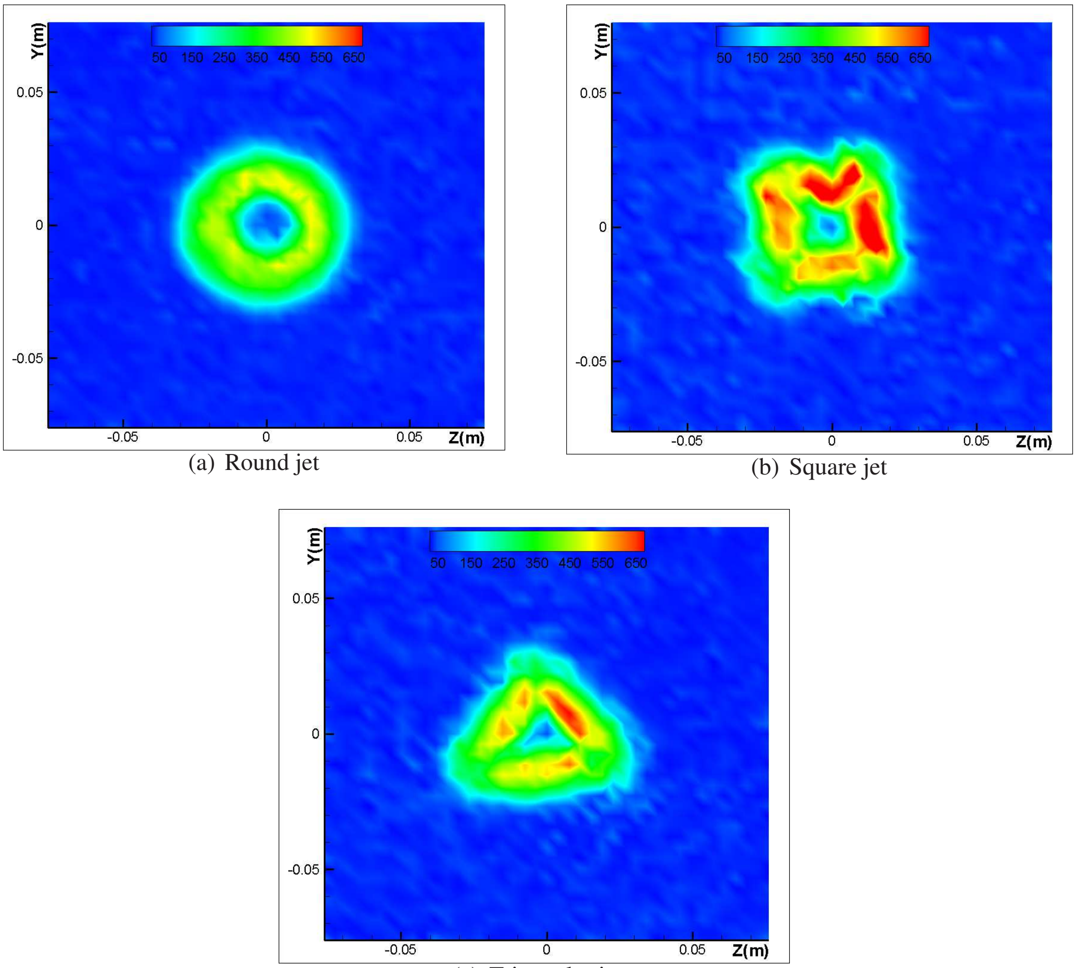

(a) Round jet

(b) Square jet

(c) Triangular jet

Figure 4.45: The extensive eigenvalues of $\overline{S_{ij}}$ at $x/d = 2$.

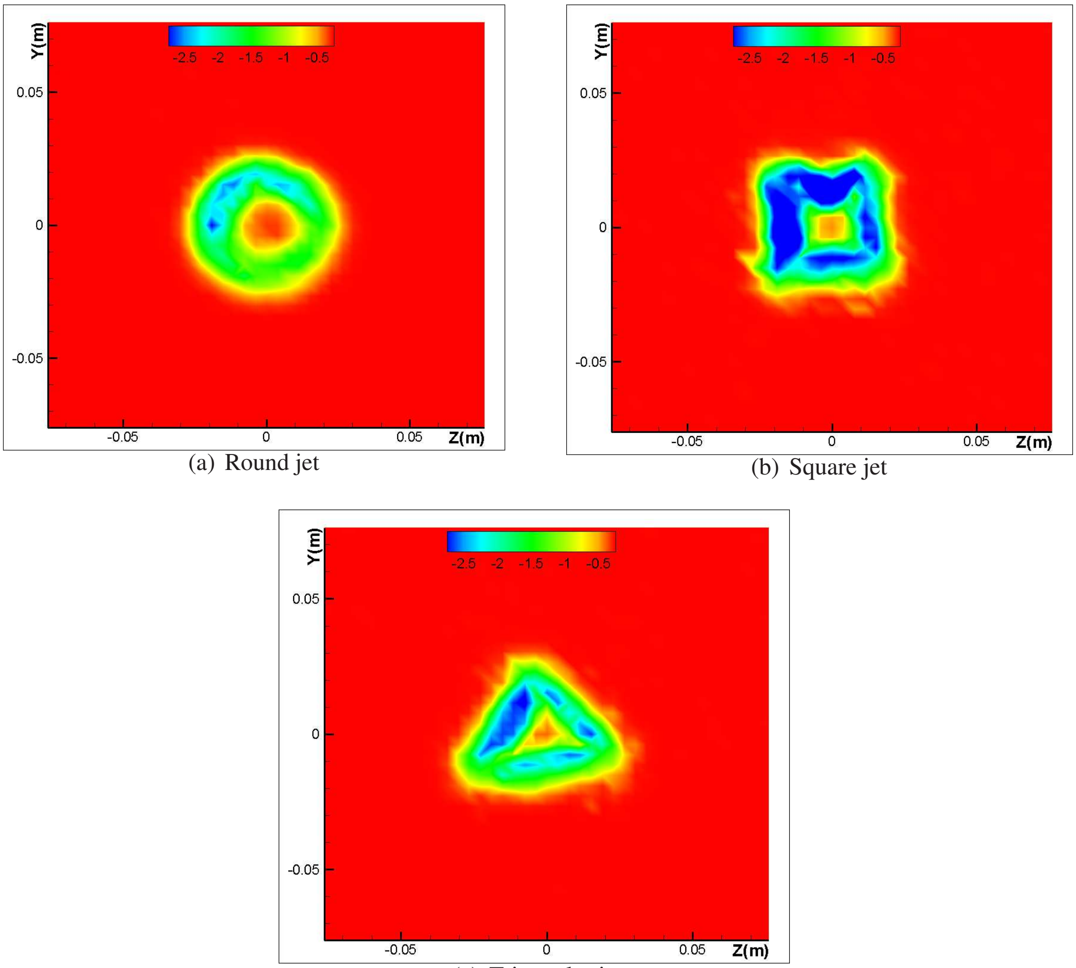

(a) Round jet

(b) Square jet

(c) Triangular jet

Figure 4.46: The first eigenvalues of $\overline{u_i u_j}$ at $x/d = 2$.

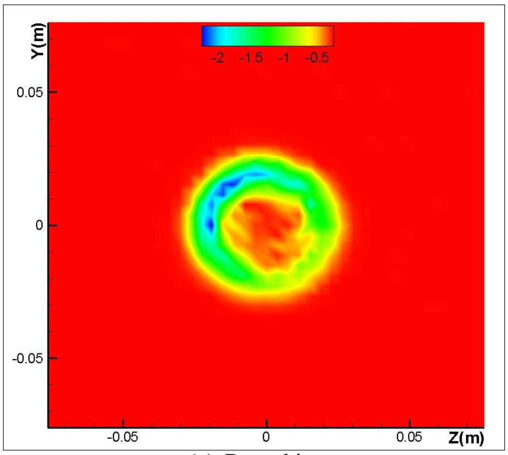

(a) Round jet

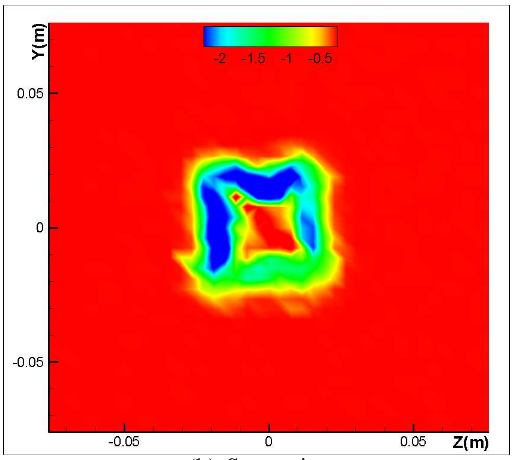

(b) Square jet

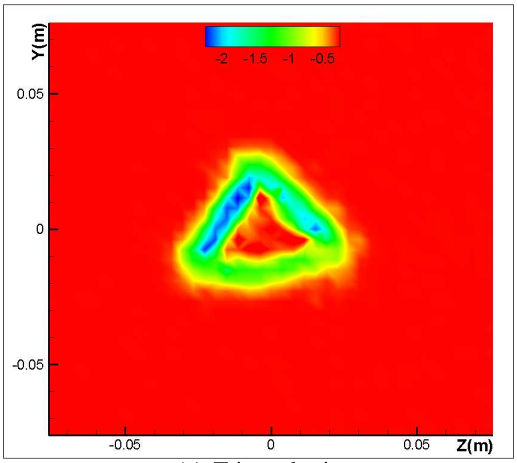

(c) Triangular jet

Figure 4.47: The second eigenvalues of $\overline{u_i u_j}$ at $x/d = 2$.

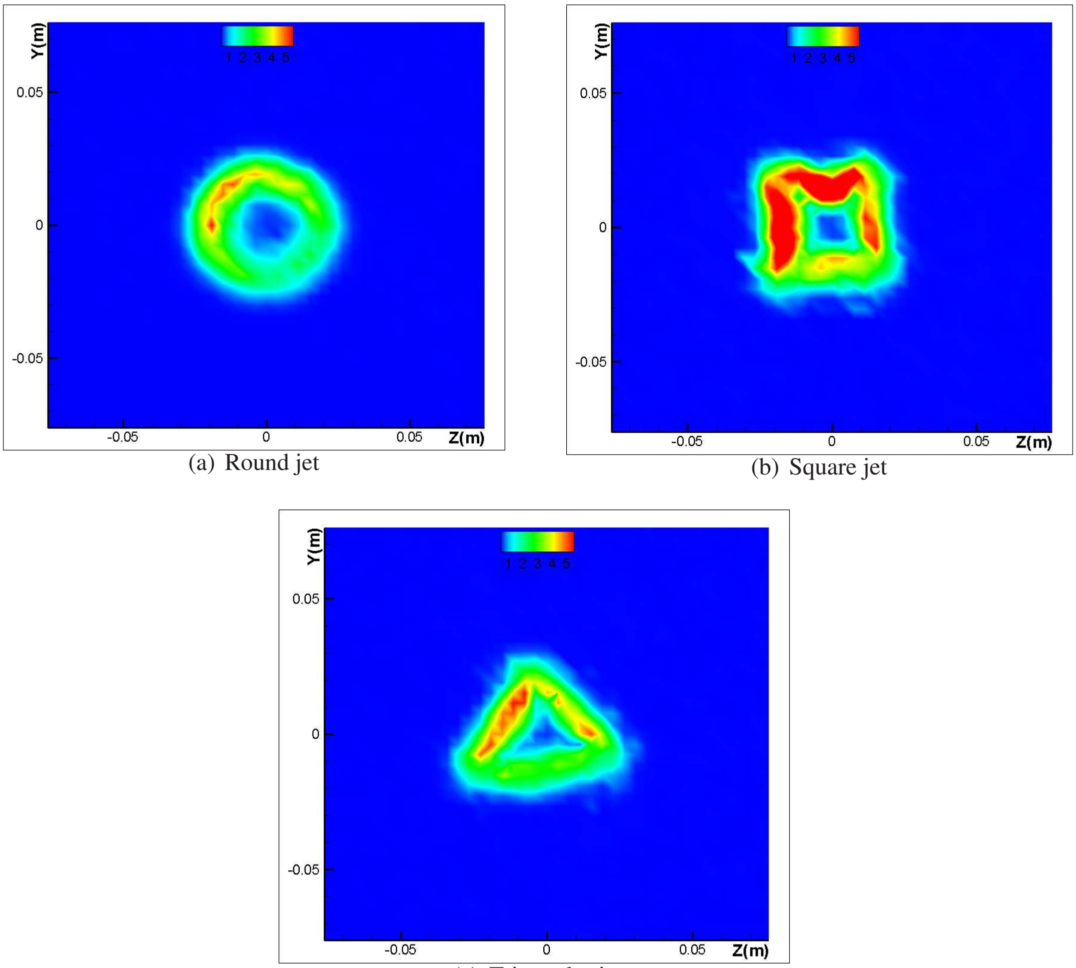

(a) Round jet

(b) Square jet

(c) Triangular jet

Figure 4.48: The third eigenvalues of $\overline{u_i u_j}$ at $x/d = 2$.

CHAPTER 5

CONCLUSIONS AND FUTURE WORK

In this study, an in-depth analysis is conducted in order to comprehend the geometry effects on flow structure and turbulence at near and far fields of air jets by using constant temperature hot wire anemometry.

The experiments are performed for round, square and triangular nozzle geometries at near and far fields of the flow field. Near field data acquisition is carried out in each streamwise station which are located at x/d = 1, 2, 4, 6 and 10. Horizontal center-plane measurements are also conducted at the near field region. The farfield streamwise stations are located at x/d =15, 20, 25, 30, 35, 40, 45 and 50. The near field data acquisition is organized to obtain the velocity fields whereas the far field data acquisition is performed in order to get one side of the centerline velocity profile.

The main aim of the far field analysis is to verify the data acquisition, data conversion and data reduction processes based on the self similarity concept. The obtained results for round jet are compared with the previous work existing in the literature in terms of the mean axial velocities,velocity decay rates, spreading rates, Reynolds' stresses and turbulent kinetic energies. Regardless of the difference between the Re's of various studies, the mean axial velocities and spreading rates are likely to introduce a universal consistency in terms of self similarity. The self similar profiles of turbulent kinetic energies and Reynolds' normal stresses can also be considered within the range of the universality. On the other hand, there is no universal self similarity established between the velocity decay rates. This result about velocity decay rate points out a solid relationship between decay rate and nozzle geometry.

The geometry effects on self similarity are also examined. It is found that the all quantities but the velocity decay rate, establish a universal self similarity in terms of different geometries, and the triangular jet has the highest velocity decay rate. The most important outcome of the far field analysis is the geometry dependence of the velocity decay rate.

In the near field analysis, mean axial, horizontal, and vertical velocities, the Reynolds' stresses, mean streamwise vortices, mass entrainment rates, turbulent kinetic energies and stress-strain relation of three types of jets are observed by means of lateral and longitudinal measurements of jet flow. The investigation of the mean axial velocities shows that the triangular jet has the lowest core length and highest diffusion which are the indicators of high mixing rates. Although the spreading rate is not calculated at near field, observing the mean vertical and horizontal velocities may give some idea about the spreading rate.

Investigation of the mean streamwise vorticity distribution which is known as the reason for the large-scale mixing indicates the better large scale behaviour of the triangular jet.

The turbulent kinetic energy distributions of all three types of jets indicate that the turbulent kinetic energy levels within the jet flow structure rise and decay much quicker for triangular jet, comparing with round and square ones. This fact is also consistent with the literature.

Another and the most important quantity for near field is mass entrainment rate and the triangular jet introduces the highest mass entrainment rate when compared with round and square jet.

The stress-strain relation is also investigated in the principal axes in order the predict a basis for turbulent modelling of air jets and consistent results with the literature are obtained.

To sum up, considering all the results, it can be said that, the triangular jet, would be the best choice in order to obtain the most efficient atomization as it possesses the highest mixing rate, mass entrainment rate and turbulence level.

Suggested future works which are mainly related with the atomization of liquid jets can be listed as

- Geometry effects on droplet size by using PIV.
- Effects of electric charges on liquid stability and droplet size.
- Effects of surfactants on liquid stability and droplet size.

- Effects of viscosity on liquid stability and droplet size.

REFERENCES

[1] E. J. Gutmark, K. C. Schadow, T. P. Parr, D. M. Hanson-Parr, K. JM. Wilson "*Non-Circular Jets in Combustion Systems*", Exp. Fluids 7:248, 1989

[2] I. Wygnanski, H. Fiedler "*Some Measurements in the Self-Preserving Jet*", J. Fluid Mech., vol. 38, pp. 572-612, 1969

[3] C. B. Baker "*An Analysis of the Turbulent Buoyant Jet*", PhD Dissertation, Pennsylvania State University, University Park PA, 1980

[4] A. A. Seif "*Higher Order Closure Model for Turbulent Jet*", PhD Dissertation, University at Buffalo, SUNNY, 1981

[5] H. J. Hussein, S. P. Capp, W. K. George "*Velocity Measurements in a High-Reynolds-Number Momentum Conserving Axis-symmetric, Turbulent Jet*", J. Fluid Mech., vol. 258, pp. 31-75, 1994

[6] R. S. Miller, C. K. Madnia, P. Givi "*Numerical Simulation of Non-Circular Jets*", Computers and Fluids Vol. 24, No. 1, pp. 1-25, 1995

[7] E. J. Gutmark, F. F. Grinstein "*Flow Control with Non-Circular Jets*", Annual Review of Fluid Mechanics, Volume 31:239-272, 1999

[8] W. R. Quinn "*Near-Field Measurements in an Equilateral Triangular Turbulent Free Jet*", AIAA Journal Vol. 43, No. 12, December, 2005

[9] W. R. Quinn "*Measurements in the Near Flow Field of an Isosceles Triangular Turbulent Free Jet*", Experiments in Fluids 39:111-126, 2005

[10] K. C. Schadow, E. J. Gutmark, D. M. Parr, K. J. Wilson "*Selective Control of Flow Coherence in Triangular Jets*", Exp. Fluids 6:129-35, 1988

[11] K. Toyada, A. K. M. F. Hussain "*Vortical Structures of Non-Circular Jets*", Proc of the Asian Congr. Fluid Mech., 4th, Hong Kong, pp. A117-27, 1989

[12] S. Gaskin, I.R. Wood "*The Axisymmetric and Plane Jet in a co-Flow*", J. Hydraulic Research, vol. 39 (5), pp. 451-458, 2001

[13] L.J.S. Bradbury, J. Riley "*The Spread of a Turbulent Plane Jet Issuing Into a Parallel Moving Air Stream*", J. Fluid Mech., vol. 27, pp. 381-394, 1967

[14] P.C.K. Chu, H.J. Lee "*Spreading of Turbulent Round Jet in a co-Flow*", J. HYdraulic Eng., vol. 20, pp. 195-204, 1999

[15] J.F.J. Maczynski "*A Round Jet in an Ambient Coaxial Stream*", J. Fluid Mech., vol. 13, pp. 597-608, 1961

[16] B. Tao, J. Katz, C. Meneveau "*Alignment of the Strain-Rate, SGS Stress, and SGS Force Relative to Parameters Based on the Filtered Velocity Gradients*", ASME Fluids Engineering Division Summer Meeting, May 29-June 1, 2001, New Orleans, Louisiana, USA

[17] H. S. Kang, C. Meneveau "*Effect of Large-Scale Coherent Structures on Subgrid-Scale Stress and Strain-Rate Eigen Vector Alignments in Turbulent Shear Flow*", Physics of Fluids 17, 055103, 2005

[18] P: K. Kundu, I. M. Cohen "*Fluid Mechanics*", Academic Press, 2002

[19] S. B. Pope "*Turbulent Flows*", Cambridge University Press, 2002

[20] J. C. Lasheras, E. J. Hopfinger "*Liquid Jet Instability and Atomization in a Co-axial Gas Stream*", Annual Review of Fluid Mechanics, Volume 32:275-308, 2000

[21] S. Koshigoe, E. J. Gutmark, K. C. Schadow "*Initial Development of Non-Circular Jets Leading to Axis-Switching*", AIAA Journal 27:411, 1989

[22] S. C. Crow, F. H. Champagne "*Orderly Structure in Jet Turbulence*", J. Fluid Mech., vol. 48, pp. 547, 1971

[23] D. Liepmann, M. Gharib "*The Role of Streamwise Vorticity in the Near-Field Entrainment of Round Jets*", J. Fluid Mech., vol. 245, pp. 643-668, 1992

[24] U. Vandsburger, C. Ding "*The Spatial Modulation of a Forced Triangular Jet*", Exp. Fluids 18:239-48, 1995

[25] A. Dewan, A. Lakshmikanth, S. Maurya "*Prediction of Turbulent Round Jet in a Co-flowing Ambient Using Different Turbulence Models*",

[26] S. P. Lin, R. D. Reitz "*Drop and Spray Formation From a Liquid Jet*", Annual Review of Fluid Mechanics, Volume 30:85-105, 1998

[27] E.A. Ibrahim , S.O. Marshall "*Instability of a Liquid Jet of Parabolic Velocity Profile*", Chemical Engineering Journal, Volume 76 17-21, 2000

[28] Y. C. Chow, O. Uzol, J. Katz "*On the Flow and Turbulence Within the Wake and Boundary Layer of a Rotor Blade Located Downstream of an IGV*", ASME Turbo Expo Power for Land Sea and Air,June 16-19, 2003, Atlanta, Georgia, USA

[29] B. Tao, J. Katz, C. Meneveau "*Effects of Strain-Rate and Subgrid Dissipation Rate on Alignment Trends Between Large and Small Scales in Turbulent Duct Flow*", ASME Fluids Engineering Division Summer Meeting, June 11-15, 2000, Boston, Massachusetts, USA